Ph.D. thesis

DECIPHERING GLOBAL AND LOCAL CONTROLS ON THE PALEOZOIC CARBON AND SULFUR CYCLES

고생대의 탄소 및 황 순환에 대한 전 지구적 및 지역적인 해석

2023년 8월

서울대학교 대학원

지구환경과학부

권효상

Deciphering global and local controls on the Paleozoic carbon and sulfur cycles

지도 교수 심 민 섭

이 논문을 이학박사 학위논문으로 제출함
2023 년 5 월

서울대학교 대학원
지구환경과학부
권 효 상

권효상의 이학박사 학위논문을 인준함
2023 년 7월

위 원 장   허 영 숙   (인)

부위원장   심 민 섭   (인)

위   원   우 주 선   (인)

위   원   주 영 지   (인)

위   원   김 문 기   (인)

ABSTRACT

DECIPHERING GLOBAL AND LOCAL CONTROLS ON THE PALEOZOIC

CARBON AND SULFUR CYCLES

Hyosang Kwon

School of Earth and Environmental Sciences

The Graduate School

Seoul National University

Stable carbon and sulfur isotope records from sedimentary rocks have been extensively employed in reconstructing the biogeochemical cycle of the ancient Earth. The objective of this thesis is to interpret the Paleozoic biogeochemical carbon and sulfur cycle, both globally and regionally, using carbon and sulfur isotope data obtained from Middle Ordovician, Late Carboniferous, and Early Permian carbonate strata.

Chapter 1 offers a comprehensive overview of the fundamental concepts related to the sulfur cycle. It covers topics such as the fractionation of sulfur isotopes sulfate reducers, the influence of depositional environment on sulfur isotope values, and the key parameters that drive changes in the global sulfur cycle. This chapter aims to provide a basis information about biogeochemical sulfur cycle for readers to enhance their understanding of the thesis.

Chapter 2 focuses on the carbon isotope chemostratigraphy and interpretation of the regional biogeochemical cycle during the Middle Ordovician, accomplished through an analysis of the isotopic compositions of carbonate carbon, organic carbon, and pyrite sulfur in the upper Joseon Supergroup

located in the Taebaek and Yeongwol areas of South Korea. Although deposited in the same basin, the Taebaek and Yeongwol groups exhibit distinct trends in $\delta^{13}C_{Carb}$. In the Taebaek Group, a -4‰ negative excursion in paired carbon isotope values is observed in the middle Jigunsan Formation, which is not observed in other regions, including the Yeongwol Group. Therefore, this negative carbon isotope excursion is likely to reflect local environmental changes and explained by enhanced organic matter degradation and benthic flux input into water column due to slow sedimentation rate. The pyrite sulfur isotope trends observed in the Taebaek Group reflect availability of organic matter for sulfate reducers, influenced by fluctuations of water depth and sedimentation rate during the deposition. However, heavy $\delta^{34}S_{Py}$ values in the middle Jigunsan Formation indicate an increase in availability due to changes in redox conditions rather than water depth. In contrast, the sulfur isotope compositions in the Yeongwol Group exhibit relatively heavier values without a clear stratigraphic trend, which is interpreted as the influence of relatively shallow and invariant water depths.

Chapter 3 is a published study about the interactions between the biogeochemical sulfur cycle, tectonic events, and climate change in the late Paleozoic. The late Paleozoic was characterized by a series of continental collisions and ice ages. Despite the drastic environmental changes, sparse sulfur isotope data hinder our understanding of the late Paleozoic biogeochemical sulfur cycle, especially during the Early Permian. To overcome this potential bias, Chapter e presents a high-resolution sulfur isotope record of carbonate-associated sulfate (CAS) and pyrite from the Carboniferous-Permian successions of the Svalbard archipelago (Gipsdalen Group). Throughout the Carboniferous, $\delta^{34}S_{CAS}$ results are largely consistent with the global trend, although the development of a restricted environment resulted in a locally observed $\delta^{34}S_{CAS}$ peak of +20‰ during the Gzhelian. The Early Permian $\delta^{34}S_{CAS}$ data in Svalbard bridge the gap in the existing record, showing a steady increase contemporaneous with the closure of the Ural Seaway and Gondwana glaciation, albeit superimposed by short-term oscillations. The enhanced incorporation of diagenetic sulfate into authigenic carbonates may have caused small-scale oscillations during the regional regression in the Artinskian. The long-term increasing trend of $\delta^{34}S_{CAS}$ and its relation to geological events can be explained by the enhanced pyrite burial flux driven

by a major shift in the locus of organic carbon burial from the continent to the ocean, with a lesser contribution from the dissolution of epicontinental Seaway evaporites. Since the onset of the Middle Carboniferous Bashkirian $\delta^{34}S_{CAS}$ excursion also corresponds in timing to the major glaciation event and the closure of the Rheic Seaway, the sulfur isotope record during the consolidation of Pangea is punctuated by the episodes of increased pyrite burial and evaporite sulfate weathering, delineating the links between paleogeography, paleoclimate, and biogeochemical cycles.

Chapter 4 introduces a mesoscale experimental method for bulk-rock CAS extraction designed for MC-ICP-MS analysis. This chapter presents the experimental results aimed at evaluating the precision and reproducibility of this method. Through experimentation with Carboniferous carbonate samples, it was confirmed that the precision and reproducibility of the new CAS extraction method were within a range of less than 1‰. However, the analysis of pyrite-added samples show alteration in sulfate isotope value, indicating experimental pyrite oxidation. For Ordovician samples, which have relatively low CAS and high pyrite content, the mesoscale method revealed a notable discrepancy from the isotope values obtained through traditional methods, suggesting that pyrite oxidation was not effectively prevented. In addition, microscale experiment to exclude pyrite oxidation also show light isotope compositions, representing possible influence of early diagenesis. However, the effect of the authigenic carbonate is diluted in bulk rock experiment due to the mixing of textures, thus it seems possible to obtain the seawater sulfate signal by using the mesoscale extraction method in the bulk rock if pyrite contents is low.

Student number: 2018-35370

TABLE OF CONTENTS

3.   RESPONSES OF THE BIOGEOCHEMICAL SULFUR CYCLE TO EARLY PERMIAN TECTONIC AND CLIMATIC EVENTS (PUBLISHED)

LIST OF TABLES

LIST OF FIGURES

Chapter 1. Introduction of the sulfur cycle

1.1 Overview of the sulfur cycle

Sulfur is the 9th most abundant element on Earth and has a wide range of redox states from +6 (SO_4^{2-}) to -2 (H_2S). Because sulfur can interact with a variety of materials, the biogeochemical sulfur cycle plays an important role in regulating Earth's redox state and carbon cycle (Garrels & Lerman, 1981; Berner & Raiswell, 1983; Berner, 1984; Torres et al., 2014; Fike et al., 2015). For example, the metabolic process of sulfate-reducing bacteria in the reduced zone of sediments can reduce the redox state of sulfur, resulting in the formation of sulfide minerals. Such a process results in the removal of reduced sulfur from the Earth's surface, further oxidizing the surface environment (Berner, 1982; 1984). 25% of the oxygen production in the present environment is due to the burial of sulfide minerals (Garrels & Lerman, 1981; Berner & Raiswell, 1983). In addition, the weathering of sulfide minerals can affect the Earth's carbon cycle and climate change. Oxidation of sulfide minerals produces hydrogen ions along with sulfate, which lowers the pH and alkalinity of seawater. As a result, seawater releases carbon dioxide into the atmosphere, contributing to global warming (Torres et al., 2014). The release of carbon dioxide from seawater through the weathering of sulfide minerals highlights the importance of understanding the sulfur cycle on a global scale.

There are three primary reservoirs in the global sulfur cycle: marine sulfate, deposits of evaporite, and pyrite in marine sediments (Bottrell & Newton, 2006). The fluxes of sulfur between these reservoirs are crucial processes in the sulfur cycle. Other reservoirs such as organic sulfur, the terrestrial hydrosphere, and atmospheric sulfur have relatively small reservoir sizes and therefore do not play significant roles in controlling the sulfur cycle (Brimblecombe et al., 1989). In the present-day environment, the concentration of marine sulfate is approximately 28 mM, and the total ocean reservoir size is estimated to be 4.2×10^{19} mol (Lowenstein et al., 2003). Given that marine sulfate accounts for

the third largest component of dissolved salts in seawater (Hayes & Waldbauer, 2006; Turchyn & DePaolo, 2019), the behavior of sulfate has a substantial impact on the overall chemical composition of the oceans.

There are numerous input fluxes of marine sulfate, such as SO_2 gas from volcanic activity or deep-sea hydrothermal vents, but riverine sulfate is known to be the largest contributor (Bottrell & Newton, 2006). The source of riverine input sulfate is the weathering of evaporite and sulfide minerals in the terrestrial environment. The magnitude of riverine input sulfate in the present environment is estimated to be approximately 1.5×10^{12} mol/yr (Kah et al., 2004). By dividing the sulfate reservoir size by the riverine input flux, it can be estimated that the residence time of marine sulfate is about 28 Ma, which is much longer than the time for ocean circulation (2000 yr). Such an estimate also suggests that sulfate is well mixed in the present ocean.

The output flux of marine sulfate includes evaporite and pyrite burial. The activity of sulfate-reducing bacteria in sediments plays a critical role in the burial of pyrite. Sulfate reducers utilize organic matter as an electron donor and sulfate as an electron acceptor, resulting in the production of hydrogen sulfide (H_2S). The hydrogen sulfide produced by sulfate reducers combines with reactive iron to form pyrite. The pyrite burial flux in marine environment is influenced by the redox state and the supply of organic matter. The current estimate for the pyrite burial flux in the present ocean is approximately 0.5×10^{12} mol/yr (Berner & Raiswell, 1983). On the other hand, evaporite burials primarily occur in arid climatic zones or specific sedimentary environments such as lagoons. Consequently, the burial flux of evaporites can vary depending on climate conditions and topography.

Reactions within the sulfur cycle result in the fractionation of stable sulfur isotopes between reactants and products (Habicht & Canfield, 1997; Habicht et al., 1998; Johnston et al., 2005a; Sim et al., 2011a, b; Leavitt et al., 2013a; Bradley et al., 2016), and these fractionation signatures are preserved in sedimentary rocks. Therefore, the analysis of stable sulfur isotope compositions in sedimentary rocks is crucial for reconstructing the sulfur cycle of the ancient Earth. There are four stable isotopes of sulfur:

^{32}S, ^{33}S, ^{34}S, and ^{36}S, with respective abundances of approximately 95%, 0.75%, 4.21%, and 0.02%. This thesis primarily focuses on the fractionation of the two most abundant isotopes, ^{32}S and ^{34}S. Stable sulfur isotope ratio is reported as standard delta notation relative to the Vienna Canyon Diablo Troilite (VCDT) standard.

$$\delta^{34}S = [(^{34}S/^{32}S)_{sample}/(^{34}S/^{32}S)_{standard} - 1] \times 1000$$

The sulfur isotope composition of sulfate can be obtained through the analysis of barite (Paytan et al., 2004), evaporite minerals (Holser et al., 1977; Claypool et al., 1980), and carbonate-associated sulfate (CAS; Strauss, 1999; Kampschulte et al.,2001; Hurtgen et al.,2002; Present et al., 2020). CAS refers to sulfate ions incorporated into the mineral structure of carbonate minerals and has been widely utilized in the study of ancient sulfur cycles. The isotopic composition of sulfide can be obtained from pyrite, and the sulfur isotope values of pyrite primarily reflect regional sulfur cycle.

Interpretation of sulfur isotope data obtained from sedimentary rocks requires the consideration of various parameters, including microbial metabolic processes, carbonate rock diagenesis, depositional environment, global geological events. Therefore, a comprehensive understanding of the sulfur cycle requires a broad range of knowledge about geology. In this chapter, the biological processes of sulfate reducers, the regional controls on sulfur isotope records, and the global factors influencing the sulfur cycle are summarized. The final part of the introduction outlines the research objectives and highlights how these studies will contribute to a deeper understanding of the Paleozoic biogeochemical cycle.

1.2 Sulfur isotope fractionation by microbial metabolic processes

Microorganisms control the partitioning of sulfur isotopes between sulfate and sulfide throughout Earth history. Therefore, a comprehensive understanding of their metabolism at the micro-scale is essential for studying the biogeochemical sulfur cycle.

All living organisms rely on the utilization of chemical energy generated through coupled reactions

between electron donors and electron acceptors. Oxygen, due to its high electronegativity and gaseous nature, is the most used electron acceptor by organisms. However, organisms living in anoxic environments are forced to use other alternatives. In marine sediments, electron acceptors are spatially segregated in the following order: oxygen, nitrogen, manganese, iron, sulfate, and carbon dioxide. This spatial order of electron acceptors is constrained by the thermodynamic yields of chemical reactions and the kinetics of metabolic pathways. Dissimilatory sulfate reduction is a metabolic process that uses sulfate as an electron acceptor to oxidize the coupling electron donor. Sulfate reduction is a common metabolic process observed in anoxic zones of marine sediments, where oxygen is lacking. This strict anaerobic characteristic restricts sulfate reduction to environments devoid of oxygen. The primary electron donors utilized in sulfate reduction are simple organic compounds, including acetate, lactate, malate, or glucose (Rabus et al., 2006). Despite its relatively low thermodynamic yield, sulfate reduction is considered a crucial metabolism in anaerobic marine environments due to the abundance of sulfate, which ranks as the third most prevalent salt in the ocean.

Sulfate-reducing bacteria (SRB) prefer to use ^{32}S during the process of sulfate reduction. As a result, the produced sulfide is depleted in ^{34}S compared to the initial sulfate. Previous investigations on SRB have aimed to determine the magnitude of sulfur isotope fractionation occurring during this metabolic process. In pure culture experiments, the maximum observed fractionation between sulfate and sulfide was 47‰ (Canfield & Teske, 1996). However, subsequent batch culture studies have reported fractionation values exceeding 65‰ (Sim et al., 2011a). These findings highlight the variability in sulfur isotope fractionation.

There is a variety of parameters that control the variability of isotopic fractionation between sulfate and sulfide including phylogeny, temperature, cell-specific sulfate reduction rate, sulfate concentration, and the availability of electron donors. However, the primary parameter for the size of fractionation is the availability of electron donors to the sulfate reducers. Microbial experiments conducted with pure cultures of sulfate reducers have explored the role of electron donors in sulfur isotope fractionation suggesting that the limitation of labile organic substrate increases the magnitude of isotopic

fractionation. (Sim et al., 2011a,b; Sim et al., 2012; Leavitt et al., 2013; Bradley et al., 2016; Sim et al., 2023).

Sulfide oxidation is another microbial metabolism process that contributes to isotopic fractionation. It converts sulfide to sulfate, which is the reverse process of sulfate reduction. Abiotic oxidation of sulfide can result in isotopic fractionations of up to 5‰ (Fry et al., 1988). In contrast, biological fractionation of sulfide oxidation is generally smaller, typically in the range of 1-2‰ (Zerkle et al., 2009). However, despite its relatively small isotopic fractionation size, sulfide oxidation may still have an important role in modulating the isotopic values of sulfur in a local scale. Further research is needed to fully understand the potential effects of sulfide oxidizers on the isotopic records of sulfur.

Sulfur disproportionation is the metabolic process that uses the intermediate valence of sulfur as both electron donors and acceptors simultaneously. Stoichiometry of disproportionation using elemental sulfur can be described as the following.

$$4S^0 + 4H_2O \rightarrow 3H_2S + SO_4^{2-} + 2H^+$$
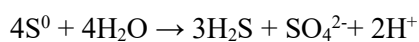
This metabolic process has been proposed to explain the large depletion of ^{34}S in sulfides (Canfield & Thamdrup, 1996). Sulfide produced after sulfate reduction can be oxidized to elemental sulfur, and subsequent disproportionation of elemental sulfur can produce sulfide that is further depleted in ^{34}S. Repeated reactions of sulfate reduction and sulfur disproportionation increase the offset between sulfate and sulfide. However, it was later found that sulfate reduction alone can produce isotopic fractionation up to 66‰, indicating that large isotopic offsets between sulfate and sulfide do not always require disproportionation (Sim et al., 2011a). More information, such as microbial community, depositional environment, or multiple sulfur isotope data, is needed to separate these two different cases.

The studies about microbiology of sulfate reducers summarized in this section are primarily those known from microbial culture experiments. Although the results of these experiments can be used to interpret ancient environments (Leavitt et al., 2013; Pasquier et al., 2017, 2021; Richardson et al., 2019; 2021) the behavior of sulfur isotopes in sediments and their preservation to sedimentary rocks require further study.

1.3 Influence of depositional environment on sulfur isotope records

Previous studies commonly used bulk rock CAS to reconstruct the ancient sulfur cycle. CAS is generally incorporated during carbonate precipitation and occurs within the water column (Staudt et al., 1994) and have considered as a reliable indicator of marine sulfate. However, the characteristics of the depositional environment and diagenetic processes can influence the CAS isotope signatures (Rennie & Turchyn, 2014; Present et al., 2019; Richardson et al., 2019; Rose et al., 2019; Ma et al., 2021; Richardson et al., 2021) due to authigenic carbonate precipitation in the pore water. Therefore, considering the sedimentology is necessary to interpret the CAS isotope values from bulk carbonate.

$\delta^{34}S_{CAS}$ records can be altered by changes in sea level and sedimentation rate. A relative sea level fall generally increases the sedimentation rate, which isolates the pore water sulfate reservoir from the overlying water column. This closed system can cause the pore water sulfate to be enriched with ^{34}S relative to seawater sulfate, and the input of heavy sulfate during the carbonate recrystallization process can increase the isotope value of CAS. Conversely, a rise in sea level generally decreases the sedimentation rate and creates a relatively open pore water environment. In such a situation, $\delta^{34}S_{CAS}$ values are similar to those of seawater due to enhanced water exchange between the pore water and seawater.

Consequently, the sulfate isotopic composition of bulk rock CAS may differ from that of seawater due to carbonate recrystallization, and this process is influenced by regional environmental changes. To overcome this potential bias, microscale analysis of sulfate using MC-ICP-MS has been developed (Das et al., 2012; Paris et al., 2013; Paris et al., 2014b), and several recent studies have reported $\delta^{34}S_{CAS}$ data from brachiopods (Wu et al., 2014; Johnson et al., 2020) and foraminifera (Rennie et al., 2018). When such samples are not available, interpretation of bulk rock CAS data requires consideration of regional environmental change.

However, it is unlikely that the change in isotope values due to authigenic carbonate will completely erase the seawater signal. Rennie & Turchyn (2014) evaluated the effect of early marine diagenesis on

CAS by comparing the isotopic record of CAS with that of coeval barite. Most of their CAS results agree well with those of barite within 2 and no more than 4 ‰. In addition, they developed a recrystallization model that illustrates the sensitivity of CAS isotope values to sedimentation rate, suggesting that the rate of carbonate recrystallization decreases exponentially, and that the degree of decrease is determined by the sedimentation rate. Using the pore water sulfate concentration profile and carbonate recrystallization rate to calculate the deviation of CAS isotope ratios, the model concluded that it is unlikely that CAS isotope values will deviate more than 4 ‰ from that of seawater.

The sulfur isotope record of sulfide can be obtained from pyrite, forms when hydrogen sulfide is scavenged by reactive iron. Because the isotopic value of seawater sulfate is nearly homogeneous in the modern ocean, changes in the offset between sulfate and sulfide at the local scale are mainly recorded in pyrite sulfur, indicating that $\delta^{34}S_{Py}$ is primarily controlled by changes in the depositional environment (Richardson et al., 2019; Rose et al., 2019; Pasquier et al., 2017, 2021). The magnitude of isotopic fractionation is determined by the delivery of labile organic carbon to the sulfate reducers (Canfield, 1994; Sim et al., 2011a,b; Sim et al., 2012; Leavitt et al., 2013; Bradley et al., 2016), which is influenced by water depth, sedimentation rate, sediment reworking, and redox conditions. In general, as water depth decreases, more organic carbon reaches the seafloor in a less decomposed state, increasing the availability of organic matter to sulfate reducers. Therefore, pyrite isotope values become heavier in a regressive environment. An increased sedimentation rate promotes a closed system behavior of pore water sulfate, resulting in progressive sulfate reduction and a parallel increase in CAS and pyrite isotope values. Recent studies support this hypothesis by reporting an increase in $\delta^{34}S_{Py}$ during the regressive phase (Pasquier et al., 2017, 2021; Richardson et al., 2019). Anoxic bottom water conditions also enhance the availability of organic carbon to the sulfate reducers, leading to an increase in $\delta^{34}S_{Py}$.

Sea level fall can increase the variability of pyrite isotope values due to the increased likelihood of bioturbation and storm forcing, leading to oxidative reworking of the pore water system (Aller et al., 2010; Richardson et al., 2019; Rose et al., 2019; Richardson et al., 2021). Oxidative reworking perturbs

the local sulfide reservoir, increasing the variability of its sulfur isotope values. In deep water, however, the pore water system is relatively less disturbed by sediment reworking, which may result in less variability in pyrite isotope values.

1.4 Global sulfur cycle

Although the consideration of local environmental changes and diagenetic processes is necessary, this does not imply that the isotopic compositions of bulk rocks are solely restricted to changes in depositional environment. In the absence of clear evidence of diagenetic alteration, it is unlikely for local effects to completely overwrite the seawater signal. CAS isotope data from bulk carbonate are still utilized as a global seawater signal, and changes in seawater sulfate isotope values are attributed to perturbations in the global sulfur cycle. Isotopic mass balance model of the global sulfur cycle in the steady state is expressed as this equation.

$$\delta^{34}S_{SO4} = \delta^{34}S_{in} + f \times \varepsilon_{avg}$$

where $\delta^{34}S_{in}$ is the isotopic value of riverine input sulfate, f shows the relative burial of pyrite exported from the marine sulfate reservoir, ε_{avg} is the mean fractionation offset between sulfate and sulfide (ε_{avg}), and $\delta^{34}S_{SO4}$ indicates sulfate isotope composition of seawater sulfate. Therefore, global seawater sulfate isotope composition is determined by variation of $\delta^{34}S_{in}$, pyrite burial rate, and $\varepsilon_{avg.}$

The source of riverine input sulfate comes from the weathering of [34]S-depleted pyrite sulfur and [34]S-enriched evaporite sulfate (Burke et al., 2018; Kemeny et al., 2021). Therefore, the isotopic composition of riverine input sulfate is determined by the relative ratio of evaporite and pyrite weathering, which can be further influenced by changes in geometry or tectonic events. For example, weathering of evaporite can increase due to the exposure of shelf areas in arid climate zones (Waldron et al., 2013; Shield et al., 2019; Johnson et al., 2020). Enhanced weathering of evaporite would increase $\delta^{34}S_{in}$, resulting in an increase in $\delta^{34}S_{SO4}$. However, tracking changes in pyrite and evaporite weathering

remains a challenge, and further studies on the weathering of sulfur-bearing minerals are needed (Burke et al., 2018).

The pyrite burial flux is recognized as the most important driver of the global sulfur cycle. Sulfate reduction produces [34]S-depleted hydrogen sulfides, a fraction of which is scavenged by reactive iron to form pyrite. The increased burial rate of pyrite results in the removal of [32]S from the marine sulfate reservoir, causing the remaining seawater sulfate to become isotopically heavier. Several factors determine pyrite burial rate: marine sulfate concentration, amount of electron donor (mainly organic matter), marine redox state, and supply of reactive iron to scavenge hydrogen sulfide. In general, sulfate concentrations below 200 μM can inhibit sulfate reduction, but seawater sulfate concentrations throughout the Phanerozoic are much higher (1-28 mM). Therefore, sulfate concentration is not an important variable in determining the burial rate of pyrite during the Phanerozoic. On the other hand, sulfur isotope fractionation hardly occurred in the Precambrian because the sulfate concentration of seawater was less than 200 μM (e.g., Guo et al. 2009, Paris et al. 2014a).

Because Phanerozoic seawater is rich in sulfate, the amount of organic matter remains the major limiting factor of sulfate reduction. Increasing the amount of organic matter available to the SRB promotes sulfate reduction, which promotes the production of hydrogen sulfide and pyrite burial flux. When other parameters such as sulfate concentration, sea surface temperature and iron availability are held constant, organic matter and pyrite burial show a positive correlation with each other. In terms of the isotopic system, increased organic matter burial would increase the carbon isotopic value of dissolved inorganic carbon (DIC), suggesting coupled sedimentary carbon and sulfur isotopic records (Gill et al., 2011; Yao et al., 2018; Johnson et al., 2020; Han et al., 2022).

Marine redox conditions are another important factor affecting the burial rate of pyrite. These conditions influence the availability of organic matter for sulfate-reducing bacteria (SRB), the location of the chemocline in the sediment, and sulfide reoxidation (Berner, 1983). In an anoxic environment, there is an increase in the burial of organic matter, extension of the sulfate reduction zone, and a decrease

in sulfide reoxidation, leading to an increased burial flux of pyrite. Therefore, a rapid increase in pyrite burial can indicate anoxic environmental conditions or a euxinic condition, which signifies the accumulation of hydrogen sulfide in both the water column and the underlying sediment. (Kurtz et al., 2003; Gill et al., 2011; Edward et al., 2018; Yao et al., 2018; He et al., 2020; Han et al., 2022).

Reactivity and amount of iron can be another limiting factor of pyrite formation in a specific environment. Sources of reactive iron include iron oxide, terrigenous clay minerals, or silt. In terrigenous marine sediments under the oxic water column, the supply of reactive iron in the marine sediment is greater than the production of hydrogen sulfide by sulfate reducers. In such marine sediments, reactive iron is generally not considered to be a limiting factor in pyrite formation. However, in a highly calcareous area consisting of high concentrations of carbonate, pyrite burial may be inhibited because carbonate has a much lower iron content than terrigenous material (Berner, 1984). Iron availability is also important for pyrite formation under euxinic conditions. Under these conditions, the amount of hydrogen sulfide produced may exceed the amount of available reactive iron and pyrite formation may be limited. When euxinic water is formed, the residual isotopic value of sulfate is enriched in ^{34}S (Gill et al., 2011; Yao et al., 2018). However, euxinic water can be easily oxidized compared to the solid form of pyrite.

Changes in the global average offset between seawater sulfate and pyrite (ε_{avg}) also potentially lead to variations in $\delta^{34}S_{SO4}$. On a global scale, ε_{avg} is influenced by the presence of shelf areas. Generally, ε_{avg} values in shelf environments are lower than those in the deep sea due to better organic matter availability for sulfate reducers in shelf. As a result, the sulfur isotope compositions of pyrite in shelf areas tend to be heavier compared to those in the deep sea. Thus, the distribution of shelf environments becomes an essential factor in determining ε_{avg}. Leavitt et al. (2013) statistically confirmed a negative correlation between the area of the continental shelf and ε_{avg} values on a global scale from the Triassic to the Cenozoic, but there is no clear correlation between them before the Triassic. According to Leavitt et al. (2013), a 1‰ increase in ε requires a decrease in shelf area equivalent to approximately 6×10^6 km2,

which corresponds to about 1.2% of the Earth's surface area. While several studies propose changes in the global average offset between seawater sulfate and pyrite to explain CAS isotope trends (Rennie et al., 2018; Johnson et al., 2020), further research on the mechanisms driving global ε_{avg} changes is necessary.

1.5 Purpose of this work

To enhance our understanding of the sulfur cycle on ancient Earth, it is crucial to obtain high-resolution and uncontaminated paired sulfur isotope data from diverse regions and interpret these data while considering various environmental parameters. Therefore, the objective of this thesis is to develop an experimental method for extracting carbonate-associated sulfur (CAS), present high-resolution sulfur isotope data from Middle Ordovician, Late Carboniferous, and Early Permian carbonate sequences, and provide interpretations of these sulfur isotope data on both regional and global scales.

Chapter 2 discusses carbon isotope chemostratigraphy and regional environmental changes during the Middle Ordovician. The Middle Ordovician has been extensively studied due to the Great Ordovician Biodiversity Event (GOBE), climate cooling, and marine oxidation. Stable carbon isotope values during the Middle Ordovician have been widely investigated to explore the potential link between the carbon cycle and the biodiversity event. In Korea, carbon isotope data have been reported in the Taebaek and Yeongwol areas, but an update of the biostratigraphy framework in the upper Joseon Supergroup requires additional carbon isotope data for a more precise chemostratigraphy and paleoenvironmental study of the MDICE. Therefore, paired carbon isotope compositions are measured in the lower to middle Darriwilian sections of the Taebaek and Yeongwol groups to enhance the carbon isotope chemostratigraphy correlation. In addition, pyrite sulfur isotope values are reported in the upper Joseon Supergroup in the Taebaek and Yeongwol areas. Considering the regional control on pyrite sulfur isotope values, a comparison of pyrite isotope compositions from the two areas is expected to elucidate the differences in depositional environments between Taebaek and Yeongwol and basin

evolution history of the Taebaeksan Basin.

Chapter 3 focuses on the late Paleozoic sulfur cycle. The Carboniferous and Permian have received considerable attention from researchers due to glacial events called the Late Paleozoic Ice Age (LPIA) and the formation of the supercontinent Pangea. However, only a few scattered CAS isotope values have been reported in the Early Permian, limiting the understanding of the sulfur cycle during the Late Paleozoic. In Chapter 3, high-resolution paired sulfur isotope values are measured in Late Paleozoic carbonate sequences from Svalbard (Gipsdalen Group). The new dataset shows an increasing pattern of sulfate isotope values superimposed by short-term oscillations of the Sakmarian, indicating the interconnected nature of geography, climate, and the sulfur cycle. The contents of this chapter was published in the May 2022 issue of Earth and Planetary Science Letters.

Chapter 4 discusses the experimental method of CAS extraction. With traditional CAS extraction methods (Hurtgen et al., 2002; Wotte et al., 2012), it is impossible to extract CAS from carbonates with low carbonate contents, and CAS data can be contaminated by pyrite oxidation during experiments. This suggests the need for an improved CAS extraction protocol. Therefore, Chapter 4 devises a bulk rock CAS extraction method for MC-ICP-MS analysis.

The interpretation of the global sulfur cycle is based on several previous studies of geologic events, and description of the regional sulfur cycle is closely related to sedimentological studies. Consequently, interpreting carbon and sulfur isotope records from the Joseon Supergroup and Gipsdalen Group would offer valuable insights into the influence of paleogeography, paleoclimate, and regional environmental changes to biogeochemical cycles during the Paleozoic.

Chapter 2. Spatial heterogeneity of the Darriwilian carbon and sulfur isotope record in the Taebaeksan Basin

2.1 Introduction

Carbon isotope records reconstructed from marine carbonate is considered as a robust archive for the biogeochemical carbon cycle and paleoenvironmental changes of ancient Earth. Global changes in organic matter burial flux perturb the global carbon isotopic system, leading to excursions in the carbon isotope records in ancient sedimentary rocks and excursions in carbon isotope values are often observed globally in various geological events (Kump et al., 1999). However, the global signal can be overprinted by the influence of changes in depositional environments. To distinguish these regional variations from the global signal, carbon isotope studies at multiple sections are needed, along with an understanding of the depositional environment of each region.

The Middle Ordovician is an interval of dynamic biogeochemical cycle and climate changes. To facilitate stratigraphic correlation and explore the potential link between the biogeochemical carbon cycle and geological events researchers have extensively studied stable carbon isotope excursions during the Middle Ordovician (Figure 2.1; Lehnert et al., 2014; Edward and Saltzman, 2014;2016; Edward et al., 2017; Bergström et al., 2020). Two international carbon isotope excursions have been identified in the Middle Ordovician: the Middle Darriwilian isotopic carbon excursion (MDICE) and the Lower Darriwilian negative isotopic carbon excursion (LDNICE). The MDICE record has been reported from various locations worldwide, including Sweden, Estonia, Siberia, North America, Argentina, Newfoundland, South China, the Tarim Basin, and North China (Figure 2.13; Buggisch et al., 2003; Ainsaar et al., 2010; Thompson and Kah, 2012; Albanesi et al., 2013; Edward and Saltzman, 2014; Lehnert et al., 2014; Young et al., 2016; Kah et al., 2016; Wu et al., 2017; Zhang and Munnecke, 2016; Yu et al., 2021; Jing et al., 2022). This widespread distribution indicates that the MDICE was a global extent. The LDNICE, a negative carbon isotope excursion occurring prior to the MDICE, has

been reported in North China, Estonia, North America, South China, Argentina, and the Tarim Basin (Lehnert et al., 2014; Edward and Saltzman, 2014; Young et al., 2016; Kah et al., 2016; Jing et al., 2022). While the MDICE and LDNICE records are global signal, the magnitude and pattern of isotope fluctuation in carbon isotope values vary by region, indicating the influence of depositional environment.

Taebaeksan Basin was part of the Sino-Korean Block, located in the equatorial peri-Gondwana region during the Ordovician. Because the Taebaeksan Basin has several areas showing different depositional environments, it is good location for comparing patterns of isotope values across depositional environments. Previously, Bang and Lee (2020) reported the Middle Ordovician carbon isotope data from the Taebaek and Yeongwol areas. Carbon isotope pattern in these two areas show significant difference, indicating possible influence of local environment to isotopic record. However, how differences in depositional environments affected carbon isotope record is still enigmatic. Additionally, conodont biostratigraphy was updated recently in Taebaek areas, requiring revision of the MDICE model in Bang and Lee (2020).

To achieve accurate carbon isotope chemostratigraphy and conduct a comprehensive paleoenvironmental study, it is crucial to obtain carbon isotope compositions covering a wide timescale but only data of the middle Darriwilian part was reported in the Joseon Supergroup (Bang and Lee, 2020). Moreover, interpreting heterogeneous carbon isotope patterns necessitates a detailed understanding of the depositional environment, but the available geochemical data is not sufficient to provide this information. Therefore, this study report carbon isotope values from the lower member of the Yeongheung Formation in the Yeongwol and the Makgol Formation in the Taebaek to establish better correlation of the MDICE record with other regions and explain the spatial heterogeneity of carbon isotope values. Furthermore, this study presents organic carbon and pyrite sulfur isotope records to understand regional carbon and sulfur cycle of the Taebaeksan Basin. It would be expected that high-resolution paired carbon isotope, pyrite sulfur isotope, and various geochemical data can enhance understanding of the influence of local environment to isotope record.
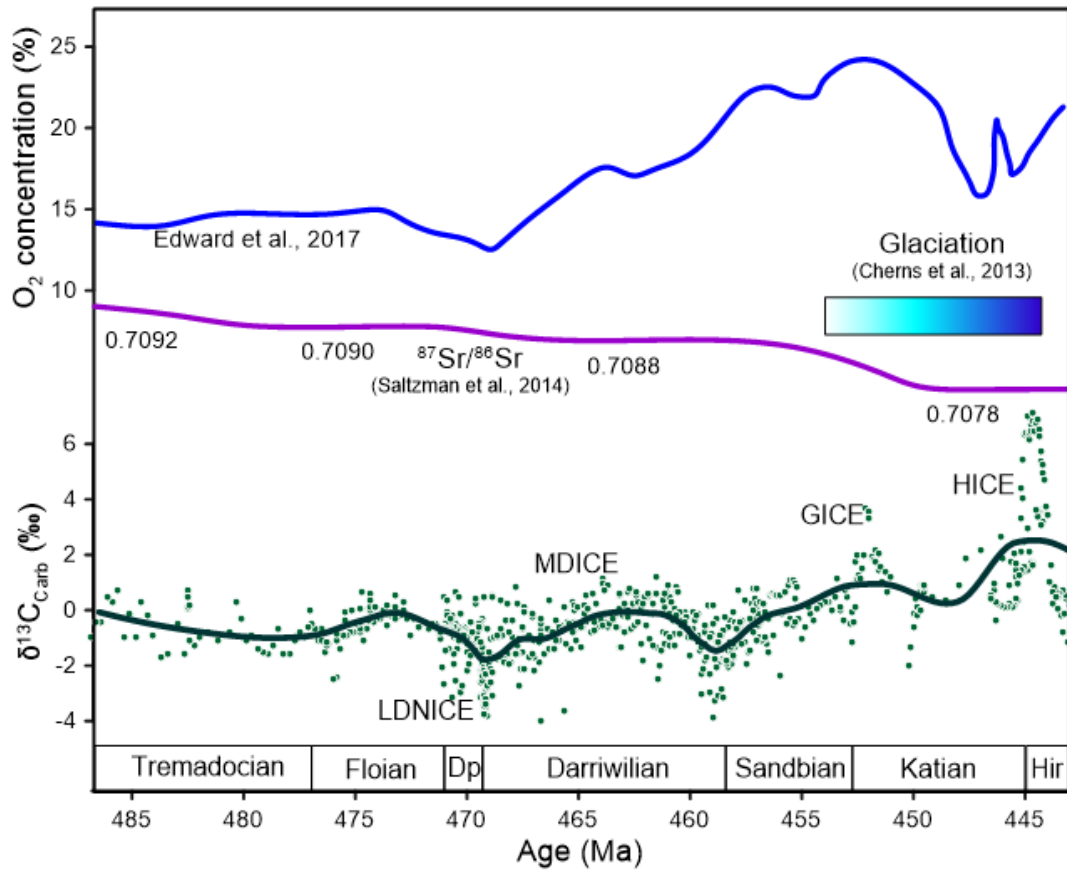
Figure 2.1. Carbon isotope curve and changes in global biogeochemical cycle during the Ordovician. Carbon isotope data from Young and Saltzman (2005), Thompson and Kah (2012), Johns and Fike (2013), Edward and Saltzman (2014), Kah et al. (2015), and Young et al. (2016). Green line indicates smoothed LOESS curve. Blue line represents atmosphere oxygen concentration during the Ordovician. Purple line indicates strontium isotope curve. Globally defined carbon isotope excursions are represented as the LDNICE, MDICE, GICE, and HICE. Time scale is based on GTS 2020 (Gradstein et al., 2020). Dp, Dapingian; Hir, Hirnantian.

2.2 Geological setting and study sites

During the early Paleozoic, the Taebaeksan basin was a part of the Sino-Korean Block (SKB) and located equatorial northeastern Gondwana (Figure 2.4; Kobayashi, 1966; Choi, 1998; Jeong and Lee 2000, 2004; Choi, 2019; Lee et al., 2023). The Cambrian-Ordovician sequences formed in central eastern Korea are referred to as the Joseon Supergroup. The Joseon Supergroup consists of a mixed carbonate-siliciclastic package that was deposited in an epicontinental sea situated in northern Gondwana. The Joseon Supergroup is subdivided into five lithologic units: the Taebaek, Yeongwol, Mungyeong, Pyeongchang, and Yongtan groups (Figure 2.5B; Choi, 1998). This study presents data obtained from the Taebaek and Yeongwol groups.

2.2.1 The Taebaek Group

The Taebaek Group is 1.5 km thick and consists of ten lithostratigraphic units: the Jangsan/Myeonsan, Myobong, Daegi, Sesong, Hwajeol, Dongjeom, Dumugol, Makgol, Jigunsan, and Duwibong formations in ascending order (Choi et al., 2004; Kwon & Chough, 2005; Kim & Lee, 2006). Among these ten formations, the Makgol, Jigunsan, and Duwibong formations correspond to the Middle Ordovician (Figures 2.2). The Makgol Formation is a 250-400 m thick carbonate sequence and consisting of lime and dolo mudstone, lime breccia, and bioclastic grainstone. The depositional environment of the Makgol Formations is described as a restricted shallow ramp to tidal flats characterized by repetition of subtidal and peritidal environment (Paik, 1987; Choi et al., 2004; Kwon et al., 2006). The age of the Makgol Formation to be from the middle Floian to the early Darriwilian (Figure 2.3; Kim, 1987; Choi et al., 2004; Lee & Seo, 2004; Cho et al., 2021; Lee et al., 2022).

The Jigunsan Formation is 30-60 m thick and is composed of greenish to gray shale and interbedded limestones. The Jigunsan Formation was deposited in suboxic deep subtidal environments (Woo & Chough, 2007; Byun et al., 2018). A sequence stratigraphic study interpreted that the lower part of the

16

Jigunsan Formation was deposited during a relative sea level rise (Woo & Chough, 2007; Byun et al., 2018). A single trilobite biozone (*Dolerobasilcus* zone; Choi et al., 2001) and the *E. suecicus – E. jigunsanensis* conodont biozone were identified in the Jigunsan Formation, indicating that deposition occurred during the middle Darriwilian (Figure 2.3; Lee & Lee, 1986; Lee & Lee, 1990; Cho et al., 2021).

The Duwibong Formation, the uppermost unit of the Taebaek Group, is 50 m thick and consists of bioclastic packstone to wackestone, and dark massive to graded grainstone. The Duwibong Formation was deposited in a carbonate ramp varying from mid ramp to peritidal environment (Lee, 1988; Lee et al., 2001). Trilobites, brachiopods, conodonts, gastropods, and bivalves indicate that the Duwibong Formation was deposited during the middle Darriwilian (Figure 2.3; Kobayashi 1966; Lee & Lee, 1986; Lee & Lee 1990; Hong et al., 2018; Cho et al., 2021). This Formation is unconformably overlain by the siliciclastic dominant Pyeongan Supergroup, deposited during the late Paleozoic.

The section studied for the Taebaek Group is the Seokgaejae section located in Bonghwa County, Gyeongsangbukdo Province (Figure 2.5D). The Seokgaejae section was sampled from the base of the Makgol Formation to the top of the Duwibong Formation. In the Seokgaejae section, the Makgol Formation is divided into four members: basal, lower, middle, and upper members. The lithology of the basal member of the Makgol Formation is dolo mudstone. The boundary between basal and lower members is characterized by subaerial exposure features such as mud crack, caliche, and lime breccia (Cho et al., 2021; Cho & Choh, 2021; Lee et al., 2022, Cho et al., 2022). The lower member consists of grainstone-mudstone couplets, stromatolitic limestone and bioturbated wackestone. The middle member is composed of massive dolostone and dolostone breccia. The upper member comprises bioturbated wackestone to grainstone, laminated dolomitic lime mudstone, and lime mudstone. The Jigunsan Formation in the Seokgaejae section is 40 m thick and consists of lower, middle, and upper units. The lower unit is 10 m thick, organic-rich, and characterized by the alteration of coarsely laminated lime mudstone and siliceous rock with calcareous nodules. The middle unit is ~20 m thick

and consists of dark gray mudstone, greenish-gray siltstone, and thin-bedded laminated grainstone. The boundary between the lower and middle units of the Jigunsan Formation is known as the maximum flooding surface (Woo & Chough, 2007; Byun et al., 2018). The upper unit of the Jigunsan Formation consists of gray siltstone, interbedded lime pebble conglomerate, and thin massive packstone to grainstone. The Duwibong Formation is about 45 m thick and consists of oncoid/ooid grainstone, massive packstone to grainstone with abundant bioclasts, and bioturbated wackestone (Figure 2.7).

2.2.2. The Yeongwol Group

The Yeongwol Group is located in the western Taebaeksan Basin and is subdivided into 5 lithostratigraphic units: the Sambangsan, Machari, Wagok, Mungok, and Yeongheung formations with decreasing age (Figure 2.2). The Yeongheung Formation is an Early to Middle Ordovician sequence (Late Tremadocian to Sandbian) based on conodont and trilobite biostratigraphic studies (Figure 2.3; Lee, 1989; Choi & Jeong, 1990; Yoo & Lee, 1997). The Yeongheung Formation is ~400 m thick and mainly composed of thick-bedded gray dolostone, solution collapsed lime breccia, bedded grainstone, and bluish-gray limestone. The depositional environment of the Yeongheung Formation is interpreted as a sabkha-type supratidal to shallow subtidal (Choi & Woo, 1993; Yoo & Lee, 1997; Hong et al., 2017; Kwon & Kwon, 2020). Extensive development of supratidal laminae, evaporite pseudomorphs, and evaporitic structures has been observed in the Yeongheung Formation, indicating high salinity and arid climatic conditions during deposition (Yoo et al., 1994; Yoo & Lee, 1997; Kwon & Kwon, 2020). The Yeongheung Formation is correlated with the Dumugol, Makgol, Jigunsan, and Duwibong formations in the Taebaek Group (Figure 2.2; Yoo et al., 1994; Yoo & Lee, 1997; Kwon & Kwon, 2020). The Yeongheung Formation is subdivided into three members: lower, middle, and upper members (Lee, 1989; Yoo & Lee, 1997; Kwon & Kwon, 2020). A conodont biostratigraphic study in the Yeongheung Formation indicated that the depositional age of the lower member is Arenigian, the middle member is Llanvirnian, and the upper member is Caradocian (Lee 1979; 1989; Lee & Yu, 1993; Kano et al. 1994;

Hong et al. 2017; Jeon et al. 2017; Park et al. 2017).

Previous studies conducted detailed geologic mapping and measured 12 sections within the Yeongheung Formation (Yoo & Lee, 1997; Choi, 1998; Kwon & Kwon, 2020). Among these sections, the Namgyo and Yeonduk sections were studied in this chapter. The Namgyo section represents the middle member of the Yeongheung Formation and is located in Omandong village, Yeongwol County (Figure 2.5). This section has a thickness of 100 meters, with a covered interval of 10 meters between 54 meters and 64 meters from the base. The Namgyo section consists of bedded grainstone, bedded lime-mudstone, and bioturbated lime mudstone (Figures 2.6C-D; Yoo & Lee, 1997; Kwon & Kwon, 2020).

In Bang and Lee (2020), an increasing trend of carbon isotope values representing the MDICE record was observed from the lowermost part of the Namgyo section. However, the negative excursion was not clearly shown in this section. To validate the presence of the LDNICE record, carbon isotope data from the Yeonduk section, which represents the lower member of the Yeongheung Formation, were analyzed. The Yeonduk section has a thickness of 43 meters and is predominantly composed of dolostone in the lower part. The middle part of the Yeonduk section consists of a solution-collapsed lime breccia bed and bedded grainstone (Figures 2.6E-F). A sequence boundary is defined at 28 meters from the base (Yoo & Lee, 1997; Kwon & Kwon, 2020). The upper part of the Yeonduk section correlates with the lower part of the Namgyo section and comprises bedded lime mudstone and laminated limestone with evaporite crystals (Kwon & Kwon, 2020).

2.2.3. Age model

The approximate absolute age should be estimated for each of the analyzed samples to globally correlate carbon isotope data. The robust biostratigraphy framework has been developed for the Ordovician succession of the Taebaek Group by analyzing conodont fossils (Lee & Lee, 1986; Lee &

Lee, 1990; Lee et al., 2001; Choi et al., 2001; Choi & Chough, 2005; Cho et al., 2021; Lee et al., 2022; Lee et al., 2023). The age of each lithostratigraphic boundary was calibrated primarily based on comparing the published conodont biozone to the Geologic Time Scale 2020 (Gradstein et al., 2020). Samples ages were then assigned according to their relative positions within the section by linear interpolation between the lithostratigraphic boundary. However, due to the uncertainty in converting conodont biozone to absolute ages, the absolute ages are not shown in the Table 2.1.

Biostratigraphy framework of the Ordovician Joseon Supergroup is summarized in Figure 2.3. Previous biostratigraphy frameworks suggested that the Makgol Formation was deposited continuously from the Floian to the early Darriwilian (Kim 1987; Choi et al., 2004; Lee & Seo, 2004). However, recent studies have established a contemporary biostratigraphy framework from the Makgol Formation to the Duwibong Formation (Cho et al., 2021; Lee et al., 2022). In the basal member of the Makgol Formation, Lee et al. (2022) identified a mid-Floian *Serratognathus bilobatus*, *Serratognathus extensus*, and *Perserratognathus obesus* conodont biozone. This study also observed a conodont barren interval with distinct changes in depositional characteristics and subaerial exposure from the uppermost basal member and lowermost lower member of the Makgol Formation in the Seokgaejae section, suggesting the Middle Floian to Early Darriwilian depositional hiatus. This hiatus can be correlated with the Huaiyuan epeirogeny that occurred in northern China (Zhen et al., 2016). The lower to upper members of the Makgol Formation are covered by the *Tangshanodus tangshanensis* zone (Cho et al., 2021; Lee et al., 2022).

In the Jigunsan Formation, two conodont biozones were identified, the lower *Tangshanodus tangshanensis* and the upper *Eoplacognathus suecicus* zones (Cho et al., 2021). Also, the *Dolerobasilcus* trilobite biozone was reported (Lee & Choi, 1992; Choi et al., 2001), indicating that deposition of Jigunsan Formation occurred during the middle Darriwilian. Throughout the Duwibong Formation, *Eoplacognathus suecicus* zone is identified, and the *Aurilobodus serratus* zone is locally identified in the uppermost part (Cho et al., 2021). The *Aurilobodus serratus* zone can be correlated to *P. serra* zone in the North China and Baltica (Lee & Seo, 2004; Wang et al., 2018).

In the Yeongwol Group, various fossils including crinoids ossicles, gastropods, brachiopods, trilobites, conodonts, sponge spicules have been reported in the Namgyo section (Yoo & Lee, 1997; Hong et al., 2017; Jeon et al., 2017; Park et al., 2017), suggesting that the depositional age of the Namgyo section is middle to late Darriwilian (Nestor & Webby, 2013; Jeon et al., 2017). The occurrence of conodonts such as *Plectodina*, *Erraticodon tangshanensis*, *Aurilobodus leptosomatus*, and *Scolopodus euspinus* also indicates that the Namgyo section was deposited in the middle Darriwilian and can be correlated from the middle member of the Makgol Formation to the Duwibong Formation (Lee, 1979; Lee, 1990; Cho et al., 2021). However, the biostratigraphy framework in the Yeongwol Group is not robust enough to constrain the biozone in each section, indicating that global correlation between Yeongwol and other regions is difficult.

Figure 2.2. Lithostratigraphic framework of the Ordovician sequences in the Taebaek and Yeongwol groups. Flo: Florian, Dp: Dapingian.

Age		Conodont Zonation		Taebaek		Yeongwol	
		N. China	N. America	Lithologic unit	Conodont biozone	Lithologic unit	Conodont biozone
Darriwilian	Dw3	*P. anserinus*	*C. sweeti*			Yeongheung	*Tasmanognathus careyi*
		Pygodus Serra	*Cahabaganathus friendsvillensis*		*Aurilobodus Serraus*		
	Dw2	*Eoplacognathus suecicus*	*Phragmodus polonicus*	Duwibong	*P. onychodonta*		*P. onychodonta*
					E. suecicus		
		Tangshanodus tangshanensis	*Histiodella holodentata*	Jigunsan	*E. Jigunsanensis*		
	Dw1			Makgol	*T. tangshanensis*		
Dapingian	Dp3	?	*H. sinuosa*	hiatus			
	Dp2		*H. altifrons*				
	Dp1		*Tripodus laevus*				

Figure 2.3. Biostratigraphy framework of the Taebaek and Yeongwol groups during the Dapingian and Darriwilian, correlated with the North America and North China conodont biozone (Gradstein et al., 2020). Information on the conodont biozone for the Taebaek and Yeongwol groups is compiled from Lee, (1979); Lee (1989); Lee & Lee (1990); Lee et al. (2001); Choi et al. (2001); Choi & Chough (2005); Cho et al. (2021); and Lee et al. (2022).

Middle Ordovician (460 Ma)
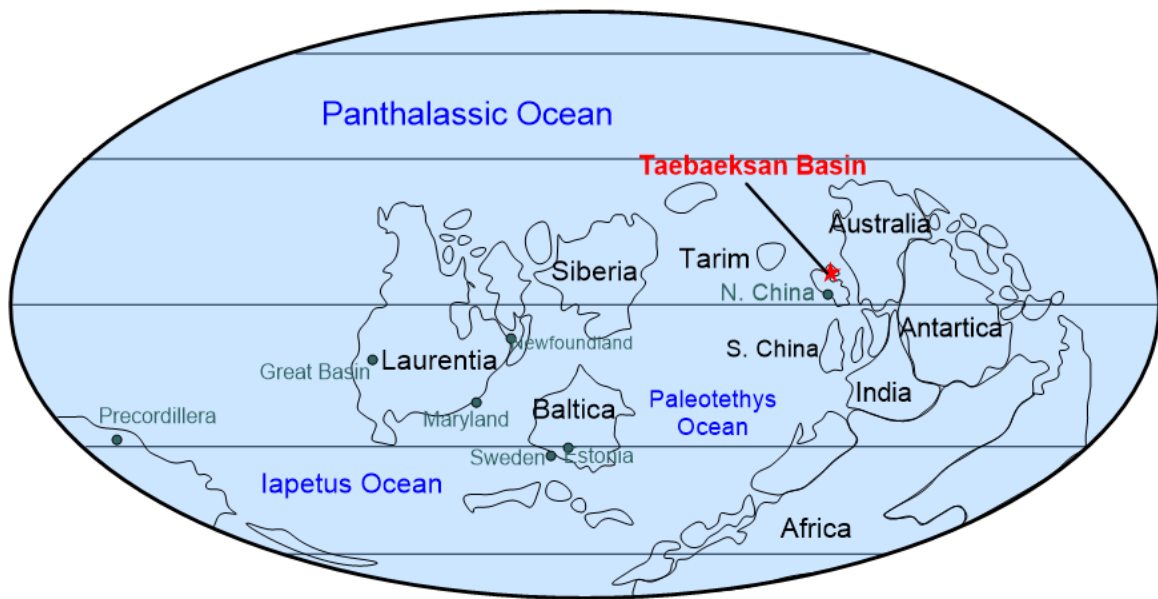
Figure 2.4. Paleogeography map and showing locations of previously studied MDICE sections (green dots) and sections of this study (red star) in the Middle Ordovician. The paleogeographic map is based on Scotese and Golonka (1997). Studied sections in previous studies are represented as green letters. Studied sections are from Buggisch et al. (2003); Ainsaar et al. (2010); Thompson & Kah, (2012); Albanesi et al. (2013); Edward & Saltzman, (2014); Lehnert et al. (2014); Young et al. (2015); Kah et al. (2015); Wu et al. (2017); Zhang and Munnecke, (2016); Yu et al. (2021); Jing et al. (2022).
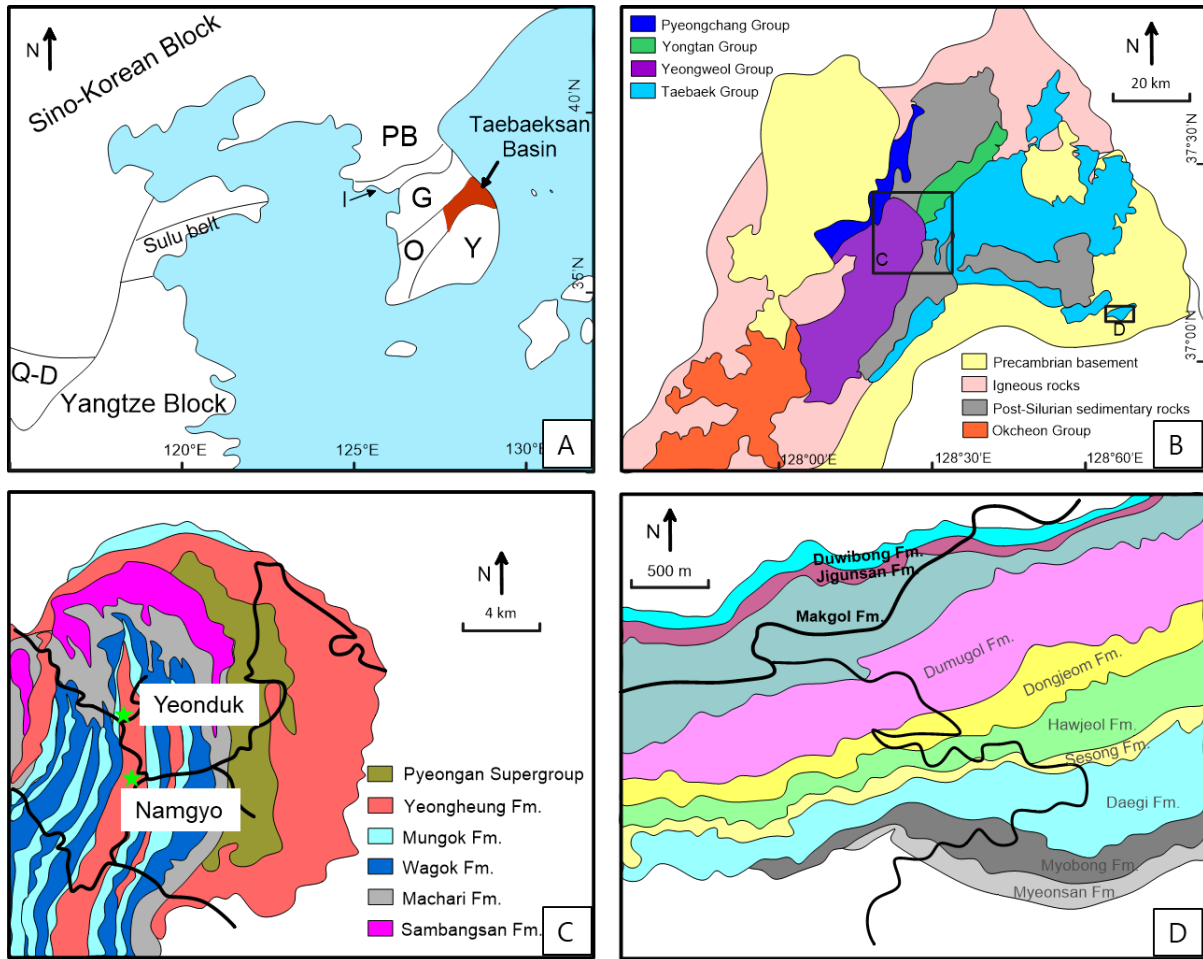
Figure 2.5. Geological map of the Taebaeksan Basin and location of sampling sites. (A) Tectonic divisions of the Korean Peninsula and the location of the Taebaeksan Basin. G: Gyeonggi Massif, O: Okcheon Belt, Y: Yeongnam Massif; Q-D: Qinling-Dabie Belt. I: Imjingang Belt; PB: Pyeongnam Basin. (Modified after Chough, 2013; Kwon & Kwon, 2020) (B) Geological map showing the Taebaeksan Basin and distribution of the Joseon Supergroup. Modified after Choi & Chough, (2005). (C) Detailed geological map of the Yeongwol area (modified after Yoo & Lee, 1997). Study sites are marked by green stars (D) Geological map of the Seokgaejae section (Modified from Choi et al., 2004).
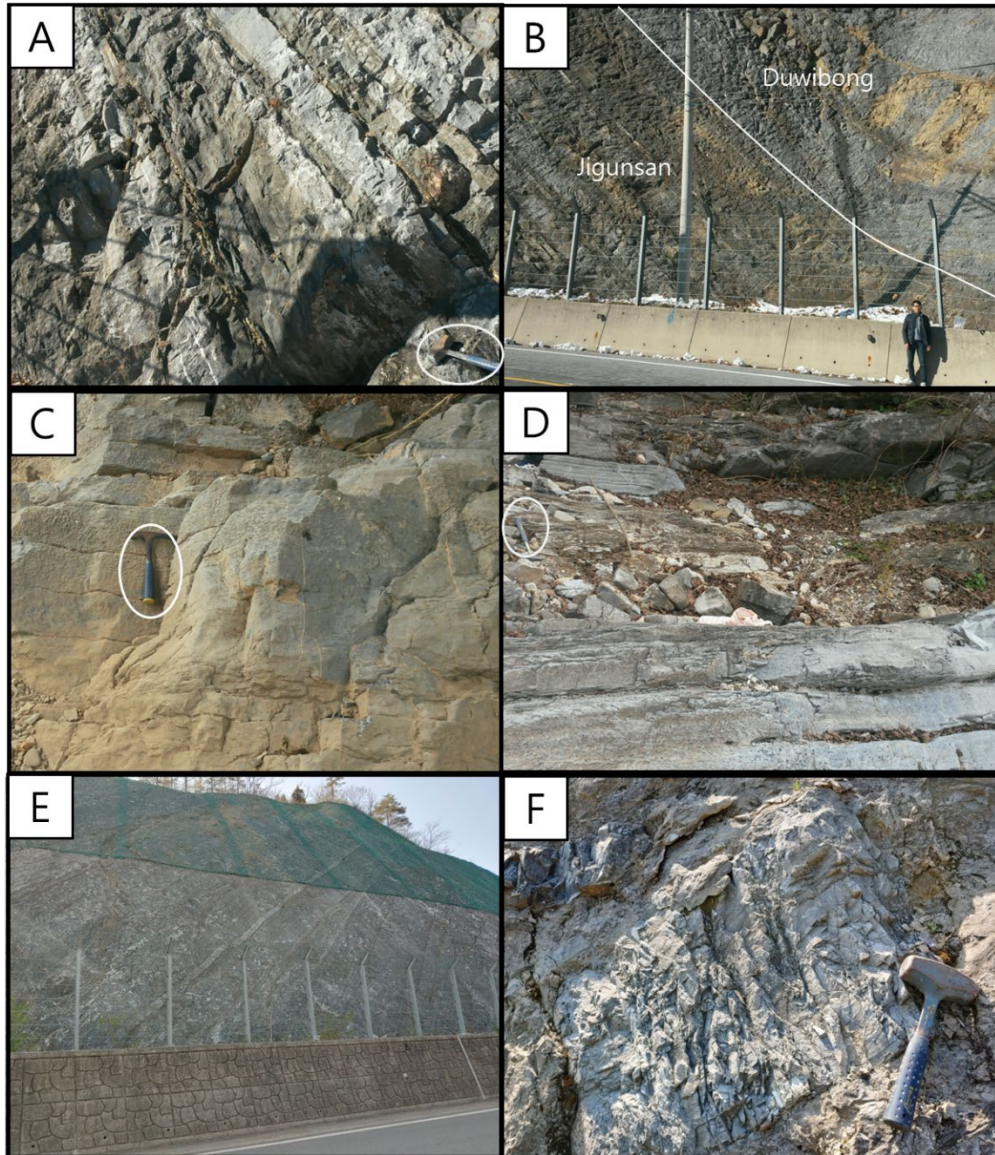
Figure 2.6. Outcrop of the Seokgaejae, Namgyo, and Yeonduk sections. White circle in figures A, B, and C indicates hammer for scale. (A) interbedded limestone in the upper Jigunsan Formation. (B) Boundary between the Jigunsan and Duwibong formations. (C) Packstone to grainstone layer in the middle part of the Namgyo section. (D) Lower boundary of the covered interval in the Namgyo section. (E) Panoramic view of the Yeonduk section. (F) Solution collapsed breccia bed with boulder size clast in the Yeonduk section
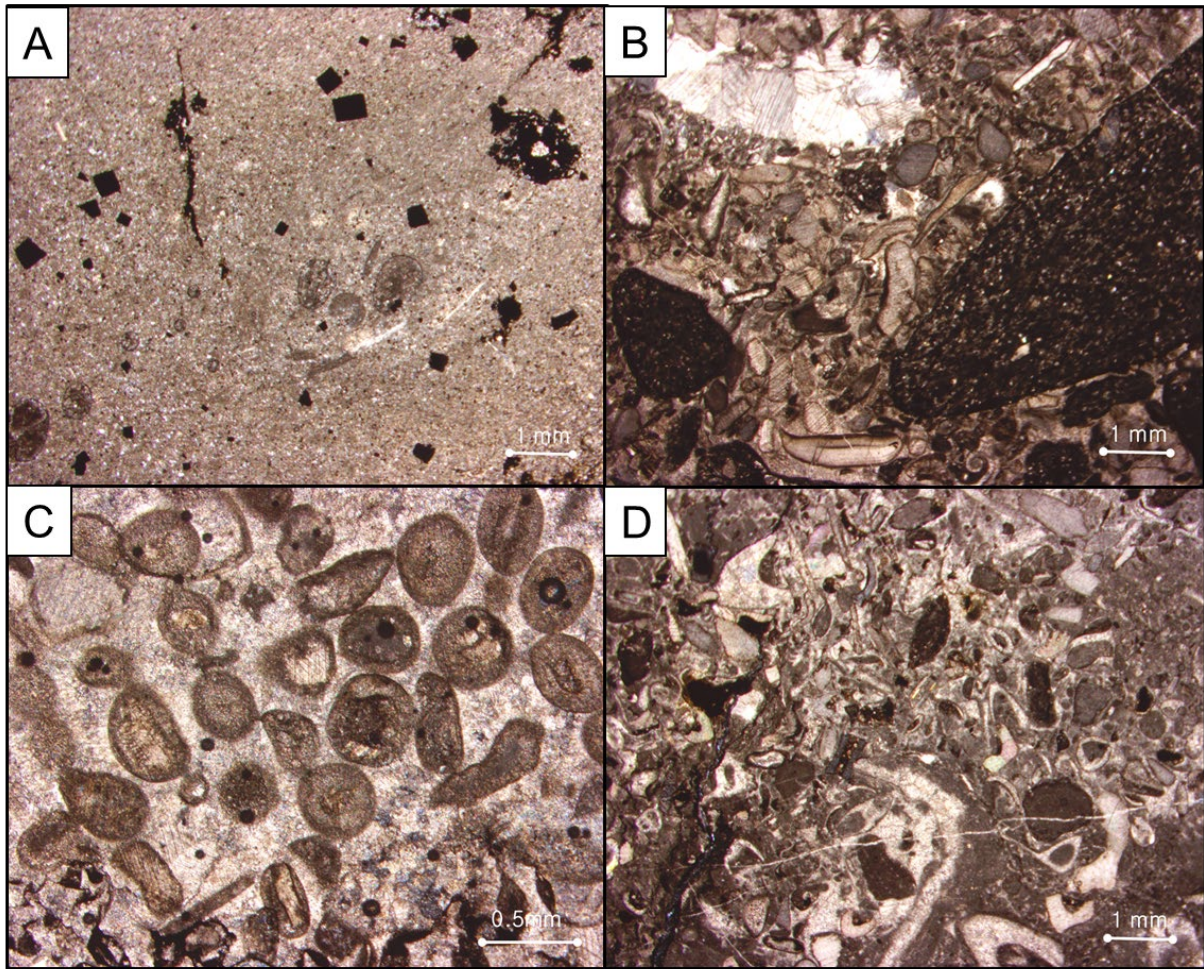
Figure 2.7. Microscopic images of thin sections from Jigunsan and Duwibong formations. (A) Laminated lime mudstone with euhedral pyrite crystals in the Jigunsan Formation (B) Bioclastic grainstone (C) Ooid packstone to grainstone (D) Skeletal packstone to grainstone.

2.3 Methods

2.3.1 Sample preparation

  Samples from the Seokgaejae and Namgyo sections were collected during a field trip in November 2015. Samples from outcrops in the Yeonduk section were collected during a field trip in April 2021. Rock samples were cut into 3-5 cm cubes, crushed to less than 1×1 cm using a jaw crusher, and ground with an agate mortar. During this process, all contaminated crusts, sample markings, and veins were removed.

2.3.2 Carbonate carbon isotope analysis

  For carbonate carbon and oxygen isotope analysis of samples from the upper and basal members of the Makgol Formation, carbonate powders were reacted with 10% phosphoric acid. Evolved carbon dioxide gas was analyzed on Thermo Finnigan Gasbench II coupled to a DeltaPlus XP Isotope Ratio Mass Spectrometer at Washington University. Carbon and oxygen isotope ratios of samples from the Yeonduk section were analyzed by Thermo Delta V IRMS coupled to a gas bench instrument at the Department of Earth and Planetary Sciences, Northwestern University. Previously reported carbon and oxygen isotope data were included in study from the Jigunsan Formation, Duwibong Formation, middle and lower members of the Makgol Formation in the Taebaek, and Namgyo section in the Yeongwol (Bang and Lee, 2020; Cho et al., 2022). Isotopic data were presented in δ notation with a VPDB scale and a reproducibility of $\pm$ 0.1‰ (1σ).

2.3.3 Organic carbon isotope analysis

  For organic carbon isotope analysis, samples were treated with 6 M HCl for 1 day. Elimination of carbonate component in the samples was confirmed by MiniFlex 600 X-ray diffraction at the School of

Earth and Environmental Sciences, Seoul National University. The insoluble residue was combusted in a Costech ECS 4010 Elemental Analyzer and the isotopic value of CO_2 was analyzed by Thermo Finnigan Delta V Advantage gas source mass spectrometer at Washington University. Samples were measured in duplicate with analytical errors of <0.25‰ and are reported in δ notation with a VPDB scale.

2.3.4 Sulfur extraction and isotopic analysis

Pyrite sulfur was extracted from the dried insoluble residue according to a procedure modified after Canfield et al. (1986). Pyrite extraction experiment required three solutions including chromium solution to release the pyrite, zinc acetate to trap the sulfide as a form of ZnS, and silver nitrate to covert ZnS to Ag_2S. Chromium reduction solution was made by reduce the $CrCl_3$ solution (266.45g $CrCl_3$, 1 L of DW and 41.25 ml of 12 N hydrochloric acid) to zinc shot. Zinc acetate solution was made by 1L of DW, 40 g of zinc acetate dihydrate and 30 ml acetic acid. Silver nitrate solution was made by 17 g of silver nitrate powder and 1L of DW.

100 ml of Zn acetate solution was filled in the bottle for H_2S trap. Nitrogen gas was circulated in the in the extraction line and the chromium reduction solution was put into bowl flask by a syringe. Samples were heated up to 130°C for 2 hours. H_2S reduced by the chromium solution was collected into Zn trap as a form of zinc sulfide. The aggregated ZnS was precipitated as silver sulfide by dropping 5 ml of $AgNO_3$ solution. Ag_2S was harvested by either filtration or centrifugation. If large amount of silver sulfide was precipitated, samples were filtered by 0.45 μm cellulose nitrate membrane filters and drying at 60°C for one day. In case of the small amount of silver sulfide precipitation, centrifugation method was used to harvest the silver sulfide. Precipitated samples and solutions were certificated for 10 minutes at 2000 rpm to settling the silver sulfide. The supernatant liquid was decanted and diluted with deionized water. This process was repeated three times and samples were dried at 60 °C for one day. Dried samples were weighed and placed in a vial.

The sulfur isotope compositions of precipitated silver sulfide from the Jigunsan and Duwibong samples were measured using a Thermo Delta V continuous-flow isotope ratio mass spectrometer (IRMS) at the Department of Earth and Planetary Sciences, Northwestern University, Evanston, USA. The sulfur isotope compositions in the Makgol Formation were measured by Thermo Finnigan Delta V Advantage gas source mass spectrometer at Washington University. Sulfur isotope ratios are reported as $\delta^{34}S$ relative to Vienna Canyon Diablo Troilite (VCDT).

2.4 Results

2.4.1 Seokgaejae section

Carbon isotope compositions from the Makgol, Jigunsan, and Duwibong formations of Seokgaejae section are described in Figure 2.8. Isotopic values of carbonate carbon, carbonate oxygen, organic carbon, and pyrite from the *T. tangshanensis* zone – barren interval boundary are described in Table 2.1 and Figure 2.9. Contents of carbonate, total organic carbon, and pyrite in the Seokgaejae section are presented in Table 2.1 and Figure 2.10. Carbonate carbon isotope data in the lower and middle part (0-114 m) of the Makgol Formation are from Cho et al. (2022) and are not presented in Table 2.1. Carbon isotope data from the subaerial exposure samples in the Makgol Formation are not shown in Figure 2.9. For CAS isotope data, barium chloride was not precipitated enough (> 2 mg) in most of the Taebaek samples due to low CAS contents. In addition, some of the data show 10-15‰ lower value than the Ordovician CAS isotope values from other regions (Figure 4.1 in Chapter 4). Considering extremely low $\delta^{34}S_{CAS}$ values and high pyrite contents, CAS isotope values were probably altered by experimental pyrite oxidation. Therefore, CAS isotope data are not presented in this chapter.

Carbon isotope values in the Seokgaejae section range from -6.8 to -0.1‰. $\delta^{13}C_{Carb}$ values are -2‰ in the basal member of the Makgol Formation. In the lower member of the Makgol Formation, $\delta^{13}C_{Carb}$ values stay between -3.9 and -1.9‰. Moving upward stratigraphically, $\delta^{13}C_{Carb}$ values shift heavier to -

1‰ in the middle member of the Makgol Formation. In the upper member of the Makgol Formation, heavier $\delta^{13}C_{Carb}$ compositions stay between -1.5 and -0.1‰ are observed. In the lower Jigunsan Formation, which covers the upper part of the *T. tangshanensis* conodont biozone, a prominent -5‰ negative trend of $\delta^{13}C_{Carb}$ is detected. Above this interval, a positive shift of carbon isotope values from the middle Jigunsan to upper Duwibong formations is presented, reaching -0.3‰ (Figure 2.8).

Pyrite sulfur isotope compositions range from -19.3 to 15.9‰ in the Seokgaejae section. Pyrite isotope composition stays heavier than 0‰ from the lower to middle members of the Makgol Formation. $\delta^{34}S_{Py}$ values decrease from 5‰ to -10‰ in the upper member of the Makgol Formation. In the lower part of the Jigunsan Formation, $\delta^{34}S_{Py}$ values range increase from -10 to 1‰. Higher stratigraphically, $\delta^{34}S_{Py}$ decreases to -20‰, followed by a continuous increase in the upper Jigunsan and Duwibong formations. In the Seokgaejae section, pyrite contents range from 78 to 8500 ppm.

The isotope composition of the organic carbon is analyzed from base of the *T. tangshanensis* zone to the uppermost part of the Duwibong Formation. $\delta^{13}C_{Org}$ value in the Seokgaejae section range from -28.6 to -23.0‰ and average value is -25.0‰. In the lower member of the Makgol Formation, $\delta^{13}C_{Org}$ value increases from -28 to -25‰. In the middle member of the Makgol Formation, organic carbon isotope values stay around -25‰, followed by decrease trend in the upper member. In the uppermost part, $\delta^{13}C_{Org}$ increase to -24‰. In the lower to middle Jigunsan Formation, a -4‰ of negative excursion in organic carbon isotope values is observed. From the upper Jigunsan to the Duwibong formations, $\delta^{13}C_{Org}$ show steady increase trend up to 23‰.

2.4.2 Yeonduk and Namgyo sections

The analytical results for the $\delta^{13}C_{Carb}$, $\delta^{13}O_{Carb}$, $\delta^{34}S_{Py}$, and pyrite contents in the Namgyo section are presented in Table 4.2 and those of the Yeonduk section are presented in Table 4.3. $\delta^{13}C_{Carb}$, $\delta^{34}S_{Py}$ and pyrite contents from the composite of the two sections are described in Figure 2.11. For CAS isotope

data, barium chloride was not precipitated enough (> 2 mg) in most of the Joseon Supergroup samples due to low CAS contents like Taebaek samples, and CAS isotope values are not reported in this chapter. In the lowermost part of the Yeonduk section, the carbon isotope values are lighter than -2‰, representing prominent negative excursion. From the middle part of the Yeonduk section to the middle part of the Namgyo section, $\delta^{13}C_{Carb}$ values show a steady increasing trend from -2‰ to 0.5‰, and no negative excursion is observed in this interval. Above the covered interval, $\delta^{13}C_{Carb}$ varies over a wide range between -2.5 and 1‰ with no stratigraphic pattern (Figure 2.11).

Pyrite sulfur isotope compositions from the Yeongwol Group vary over a wide range between -10 and 25‰. However, there is no stratigraphic pattern in the $\delta^{34}S_{Py}$ data from the Yeongwol Group, and the point-to-point variation in $\delta^{34}S_{Py}$ is larger than that of the Taebaek Group (Figure 2.11). Pyrite contents range from 12 to 1004 ppm, which is relatively lower than that of the Taebaek Group.

2.5 Discussion

2.5.1 Preservation of primary marine signal

  It is important to consider the effect of diagenesis on stable isotope values prior to interpreting the global and regional significance of the data. Previous studies have concluded that diagenesis can alter the original isotopic signals. A positive correlation between $\delta^{13}C_{Carb}$ and $\delta^{18}O_{Carb}$ is one of the useful criteria that can indicate the influence of diagenetic alteration by meteoric fluid, which is more depleted in $\delta^{13}C$ and $\delta^{18}O$ than seawater (Given & Lohmann, 1986; Darry, 2010). In the Seokgaejae section, a cross plot of $\delta^{13}C_{Carb}$ and $\delta^{18}O_{Carb}$ shows little correlation in the Makgol, Jigunsan, and Duwibong formations, with R^2 value of 0.0232, 0.1841, and 0.0051, respectively (Figure 2.12A). A cross plot of $\delta^{13}C_{Carb}$ and $\delta^{18}O_{Carb}$ indicate that the R^2 value is 0.07 for the Namgyo section and 0.16 for Yeonduk section, representing little covariation (Figure 2.12B). Although oxygen isotope values in the Seokgaejae section is generally low, alteration of $\delta^{13}C_{Carb}$ during diagenesis or sample preparation is not apparent in the studied section.

2.5.2 Spatial heterogeneity of carbon isotope data in Taebaek and Yeongwol areas

  The middle Yeongheung Formation, along with the Makgol, Jigunsan, and Duwibong Formations, was deposited in the same basin during the Ordovician, leading to the expectation of similar isotope patterns in these regions. Bang and Lee (2020) identified the range of the MDICE as occurring from the middle Jigunsan (30 m from the basal) to the upper Duwibong Formation in the Taebaek area and from the lower part of the Namgyo section (5 m from the base) to the lower boundary of the covered interval in the Yeongwol area. This study reported the LDNICE records in both sections. In the Taebaek section, there is a prominent -4‰ negative excursion in the lower Jigunsan Formation and a -1‰ short negative excursion in the lowermost part of the Namgyo section. Because the ambiguous negative excursion in the Yeongwol area could be attributed to the short temporal coverage of carbon isotope data, additional carbon isotope compositions are measured from the Yeonduk section and Makgol

Formation.

The basal member of the Makgol Formation displays $\delta^{13}C_{Carb}$ values around -2‰, slightly lighter than the $\delta^{13}C_{Carb}$ values observed in the in other regions (Figure 2.8; Thompson & Kah, 2012; Edwards & Saltzman, 2014). A rapid shift in isotopic values occurs at the boundary between the basal and lower members, supporting a Floian-Darriwilian hiatus within the Makgol Formation (Lee et al., 2022). However, since the Yeonduk section may not cover the middle Floian, it is not possible to compare the basal member of the Makgol Formation with the Yeongwol Group. In the lower member of the Makgol Formation, a negative excursion of -3‰ in $\delta^{13}C_{Carb}$ values is observed, which gradually increases to around -1‰ in the middle and upper members (Figure 2.9). This isotopic trend is also evident in the Yeonduk section, with a negative excursion of -3‰ in the lower part and a consistent increasing trend in the upper part (Figure 2.11). Therefore, the negative excursion in the lower part of the Yeonduk section may be correlated to that in the lower member of the Makgol Formation.

However, the Taebaek and Yeongwol groups still exhibit notably different patterns in $\delta^{13}C_{Carb}$ values after the measurement of the carbon isotope composition in the Yeonduk section and Makgol Formation above the sequence boundary. In the middle Jigunsan Formation, a significant negative excursion is observed in the carbon isotope values (Figure 2.9). However, no such negative excursion is observed in the Namgyo and Yeonduk sections above the sequence boundary. Instead, the carbon isotope values of lower part of the Namgyo and upper part of the Yeonduk sections display a consistent increasing trend (Figure 2.11). Despite uncertainties in the age control of the Yeongwol group, it is important to note that the Namgyo section was deposited during the Darriwilian and corresponds to the Jigunsan and Duwibong formations (Yoo et al., 1994; Yoo & Lee, 1997; Kwon & Kwon, 2020), and the difference in $\delta^{13}C_{Carb}$ values between these two sections is not solely attributed to age control and carbon isotope data can be significantly influenced by local environmental factors.
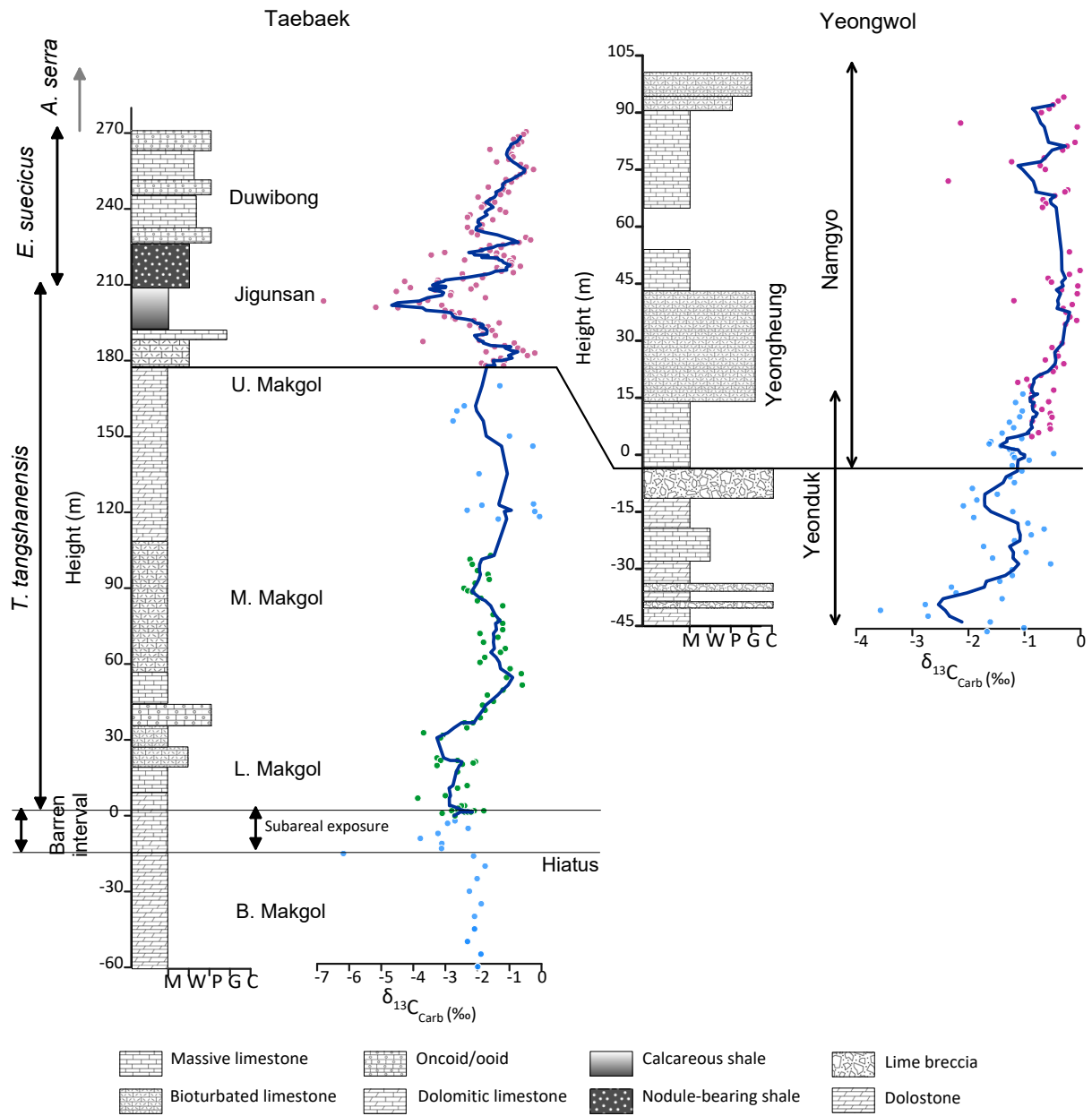
Figure 2.8. Biostratigraphic subdivision and high-resolution carbon isotope data of the Middle Ordovician succession in the Seokgaejae, Yeonduk, and Namgyo sections. Data from Bang & Lee. (2020) are shown as purple dots, from Cho et al. (2022) are represented as green dots. Blue line indicates five-point moving average curve from the base of *T. tangshanensis* zone.
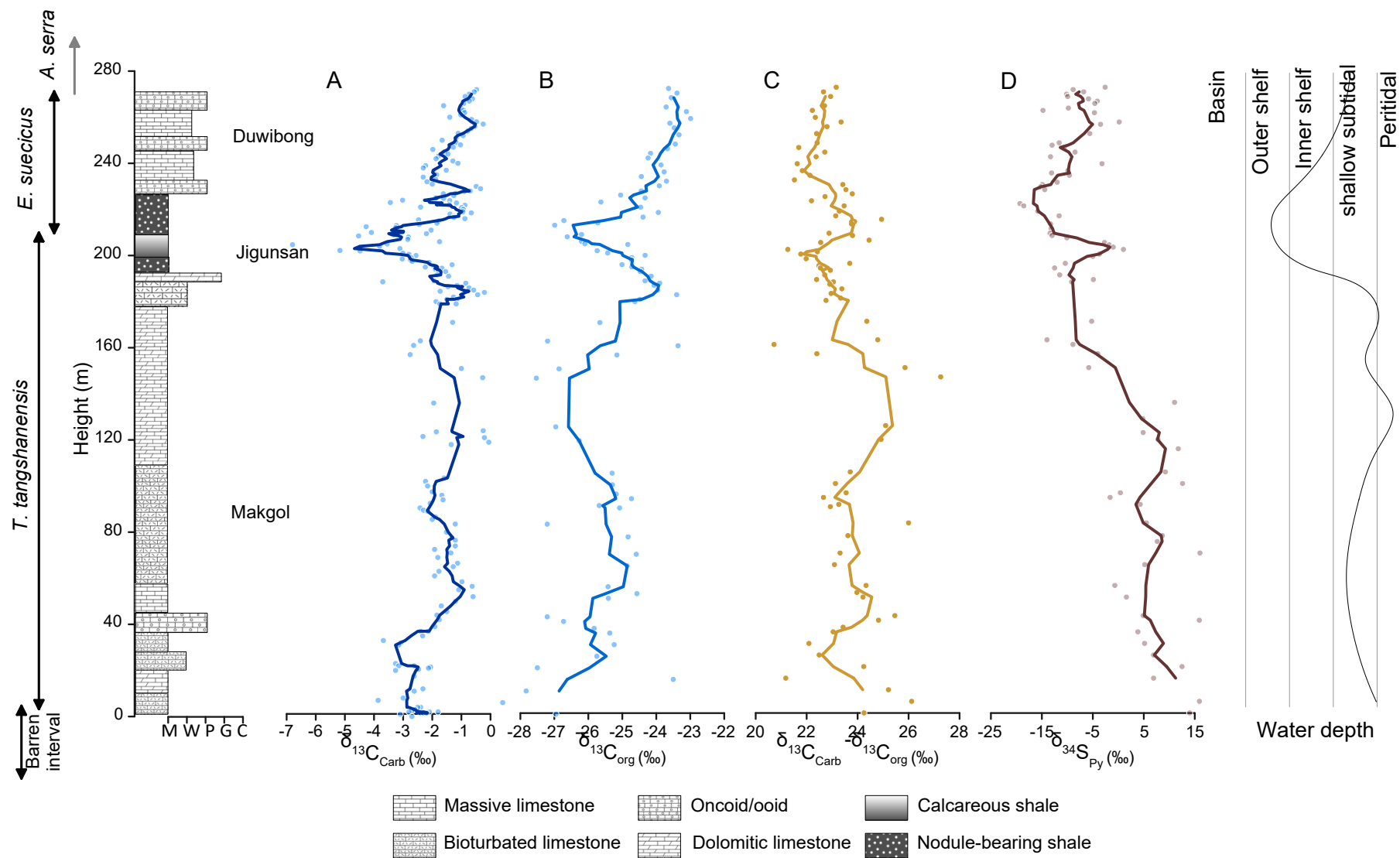
Figure 2.9. Plot of carbonate carbon isotope, organic carbon isotope, difference between carbonate and organic carbon isotope value, and pyrite sulfur isotope value with water depth curve (modified after Woo & Chough, 2007; Byun et al., 2018; Kwon & Kwon, 2020) and conodont biozone (modified after Cho et al., 2021; Lee et al., 2022) in the Seokgaejae section from the base of the *T. tangshanensis* zone. Isotopic data from the samples with subaerial exposure were excluded in this plot. The $\delta^{13}C_{Carb}$ - $\delta^{13}C_{org}$ values for the lower and middle members of the Makgol Formation were calculated using the carbonate carbon isotope data from Cho et al. (2022) at the same stratigraphic level as the organic carbon isotope data. Deep blue, light blue, yellow, and brown curves indicate 5-point moving average of carbonate carbon isotope, organic carbon isotope, difference between carbonate and organic carbon isotope value, and pyrite sulfur isotope, respectively.
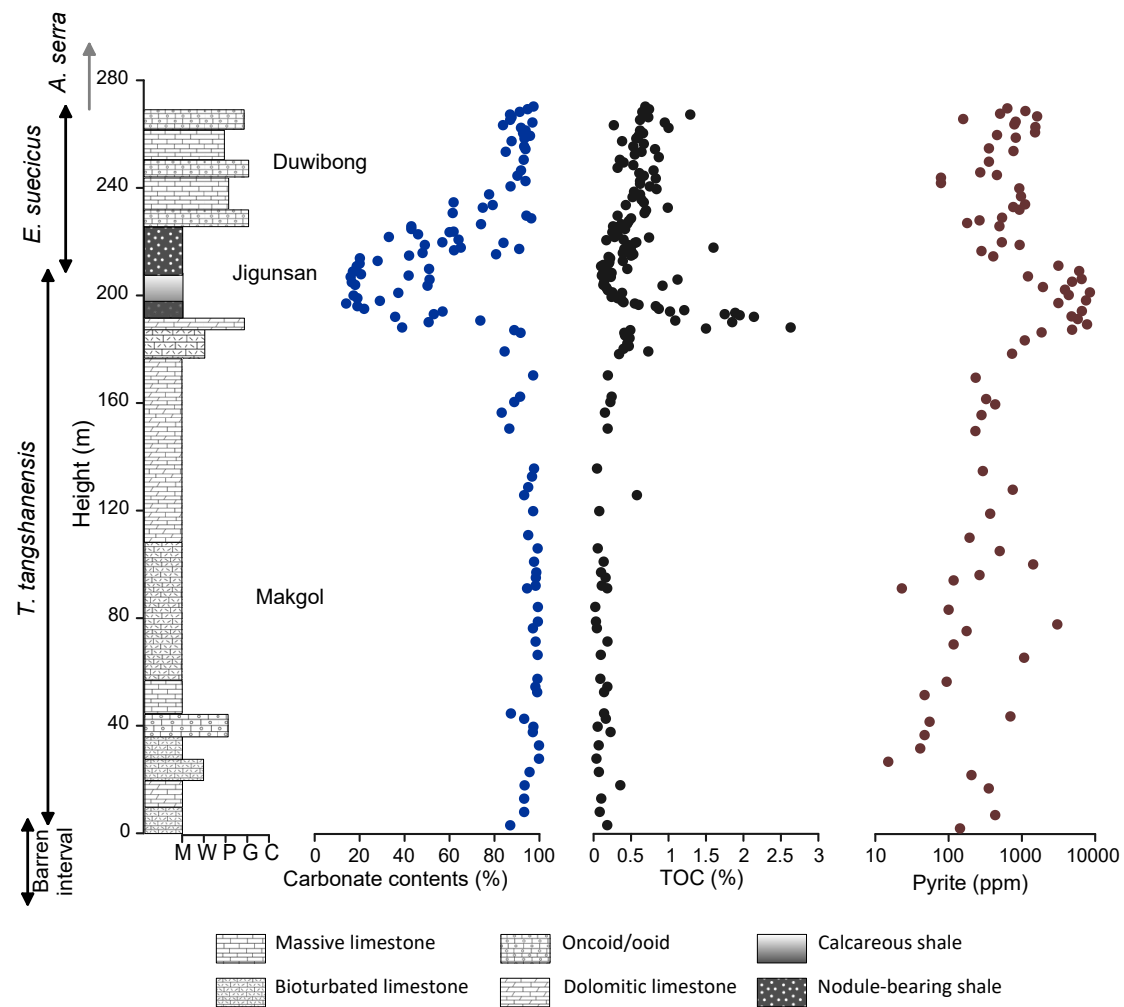
Figure 2.10. Plot of carbonate contents, total organic carbon, and pyrite contents in the Seokgaejae section from the base of *T. tangshanensis* zone.

38
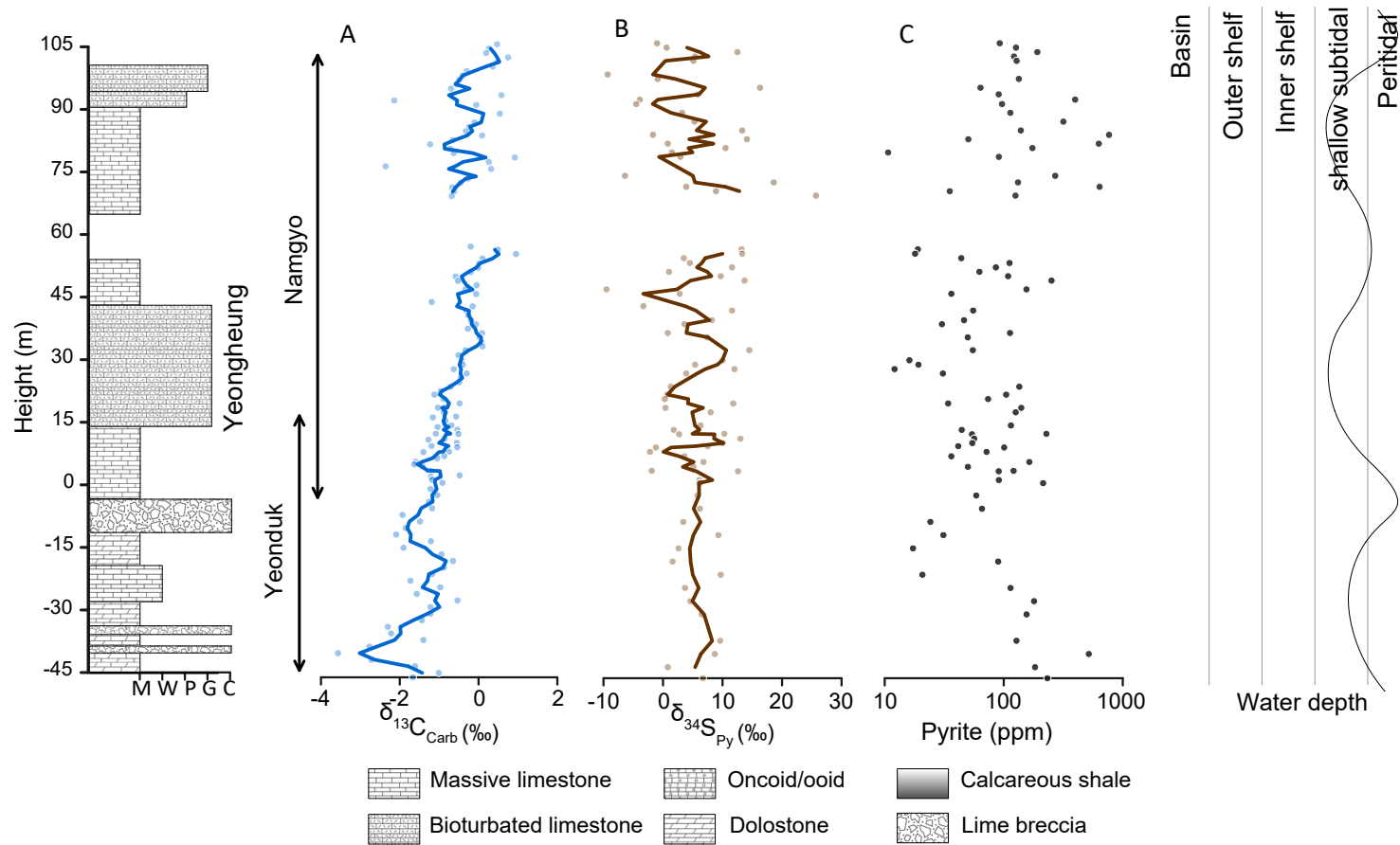
Figure 2.11. Plot of carbonate carbon, pyrite sulfur isotope compositions, and pyrite contents in the Yeongwol Group (composite of Namgyo and Yeonduk sections) with water depth curve (modified after Kwon, 2012). Blue and brown lines in figures A and B represent 5-point moving average curve of carbon and pyrite sulfur isotopic data, respectively.
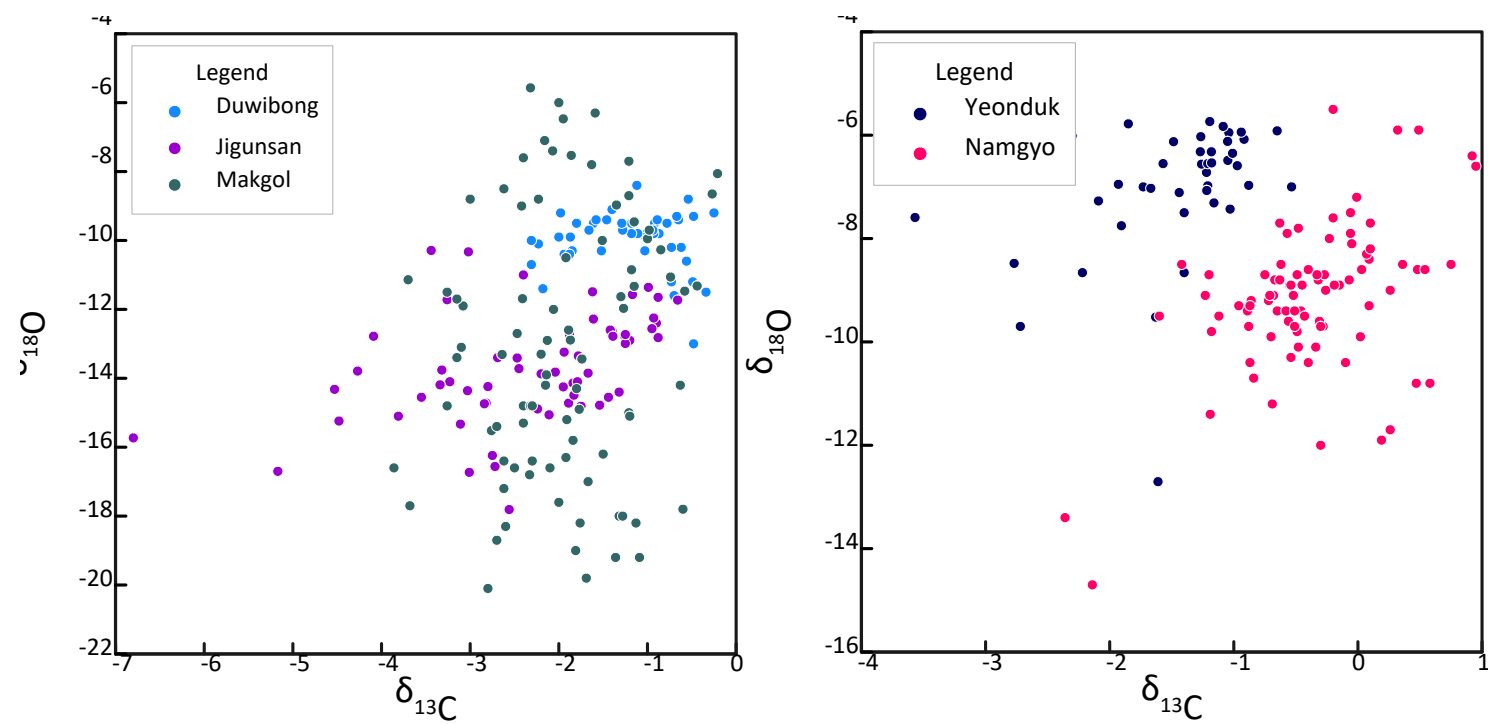
Figure 2.12. Cross plots of carbonate carbon isotope and oxygen isotope data from the Taebaek (A) and Yeongwol (B) areas.
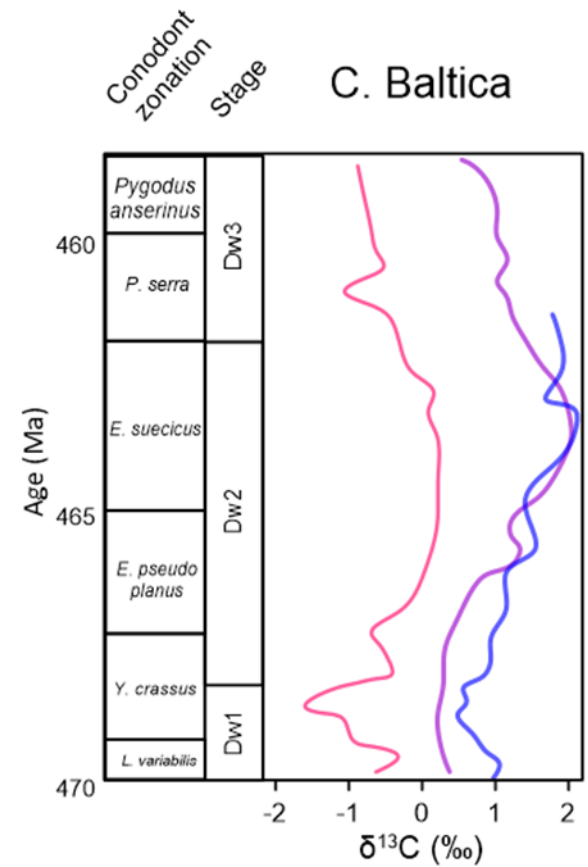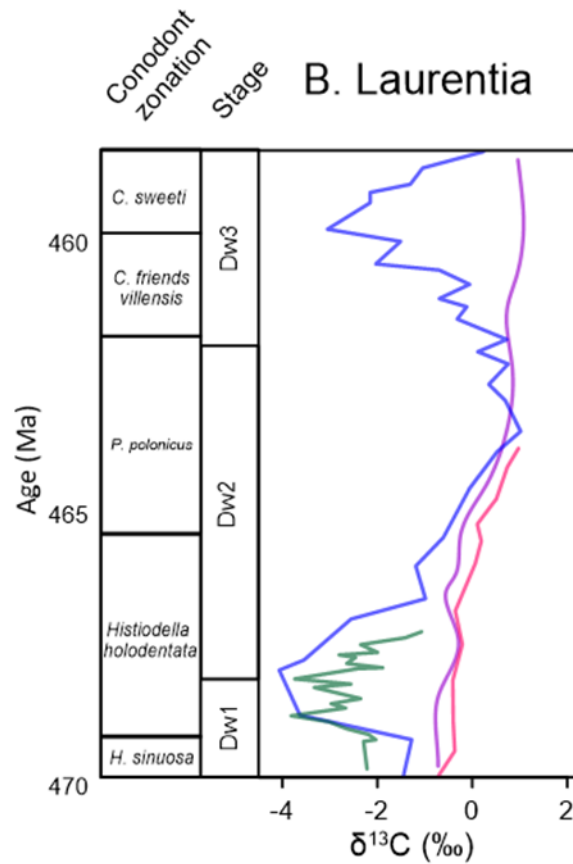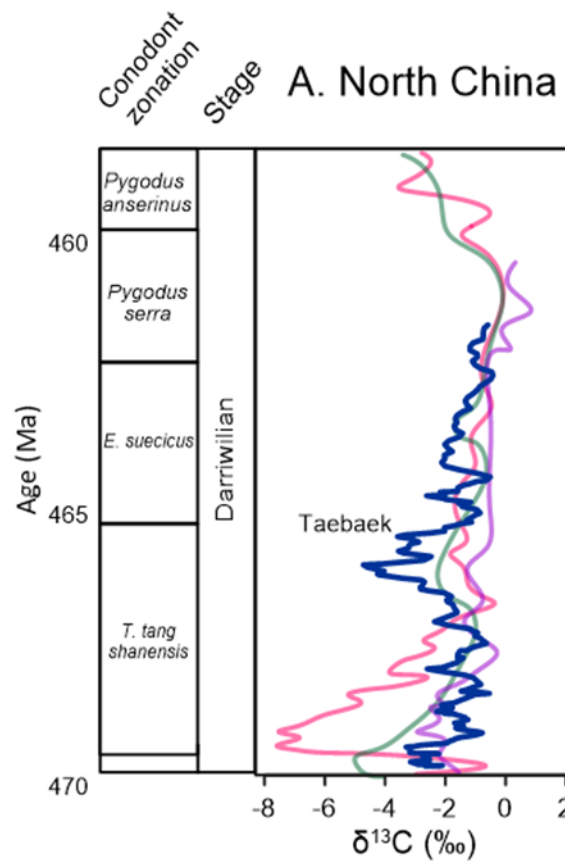
Figure 2.13. Correlation of conodont biostratigraphy and carbon isotope curve among the Darriwilian carbonate successions in (A) North China, (B) Laurentia, and (C) Baltica. In Figure A, the thick blue line represents the carbon isotope curve of Taebaek, the red line indicates the Tao-112 core, the green line shows the composite of Hejin and Linfen outcrops, and the purple line represents the Yangjikan outcrop. In Figure B, blue line represents data from the Clear spring section in Maryland (Young et al., 2015), red line indicates western Newfoundland (Thompson and Kah, 2012), green line shows Shingle Pass in the Great Basin (Edward and Saltzman, 2014), and purple line represents data from Precordillera (Buggisch et al., 2003; Thompson and Kah, 2012; Kah et al., 2015). Although Precordillera is located in Argentina, they are shown together in figure B because this area shares the same conodont zonation with North America. In Figure C, the red line indicates data from the Mehikooma 421 drill core in Estonia (Ainsaar et al., 2010), the blue line represents the Mora 001 drill core in Sweden (Lehnert et al., 2014), and the purple line shows the Tingskullen drill core in Sweden (Wu et al., 2017). Sample locations for each region are shown in Figure 2.4. Abbreviations: Dw=Darriwilian

Table 2.1. carbonate contents, carbonate carbon isotope, total organic carbon, organic carbon isotope, pyrite contents and pyrite sulfur isotope data from the Seokgaejae section with conodont biozone. Carbon and oxygen isotope data from Cho et al. (2022) are not presented in this Table.

Sample	Height (m)	CaCO$_3$ %	$\delta^{13}C_{carb}$ (‰)	$\delta^{18}O$ (‰)	TOC %	$\delta^{13}C_{org}$ (‰)	Pyrite (ppm)	$\delta^{34}S_{Py}$ (‰)	biozone
D45	270	97.36	-0.5	-13.0	0.69	-23.6	633	-2.6	*A.serra*
D44	269	94.74	-0.6	-10.6	0.74		1115	-8.9	*A.serra*
D43	268	91.22	-0.7	-11.2	0.65	-23.4	504	-6.8	*A.serra*
D42	267	86.92	-0.9	-9.8	1.29		1613	-10.2	*A.serra*
D41	266	87.6	-0.6	-10.2	0.73	-23.6	158	-9.9	*A.serra*
D40	265	87	-0.7	-10.2	0.62		823	-5.9	*A.serra*
D39	264	96.88	-0.9	-9.5	0.95		789	-4.1	*A.serra*
D38	263	83.8	-1.6	-9.5	0.27		1526	-4.6	*A.serra*
D37	262	91.8	-1.0	-9.8	1	-23.7			*A.serra*
D36	261	93.82	-0.9	-9.8	0.62		1512	-9.8	*A.serra*
D35	260	92.72	-0.9	-9.4	0.66	-23.1	458	-14.8	*A.serra*
D34	259	95.8	-1.0	-9.9	0.6		825	-4.7	*E. suecicus*
D33	258	93.34	-1.4	-9.1	0.57				*E. suecicus*
D32	257	87.6	-0.7	-9.4	0.38	-23.0			*E. suecicus*
D31	256		-0.5	-9.3	0.67				*E. suecicus*
D30	255	93.2	-0.3	-9.2	0.53	-23.6	355	0.2	*E. suecicus*
D29	254	93.8	-0.5	-8.8	0.82		767	-3.5	*E. suecicus*
D28	253	85	-0.7	-9.3	0.64				*E. suecicus*

D27	252		-0.8	-9.5	0.55				*E. suecicus*
D26	251		-1.1	-9.8	0.87				*E. suecicus*
D25	250	93	-0.9	-9.7	0.35	-23.3	355	-5.6	*E. suecicus*
D24	249		-1.2	-9.8	0.4				*E. suecicus*
D23	248		-1.7	-9.7	0.53				*E. suecicus*
D22	247		-1.2	-9.5	0.32				*E. suecicus*
D21	246	91.8	-1.0	-10.3	0.8	-23.4	270	-11.6	*E. suecicus*
D20	245		-1.3	-9.7	0.61		456	-13.0	*E. suecicus*
D19	244	90.2	-2.0	-9.2	0.67	-23.7	79	-10.6	*E. suecicus*
D18	243		-1.6	-9.4	0.83				*E. suecicus*
D17	242	93.8	-1.5	-9.4	0.62	-24.2	79	-8.5	*E. suecicus*
D16	241		-1.8	-9.5	0.62				*E. suecicus*
D15	240	87.14	-1.9	-9.9	0.75	-24.2	921	-13.3	*E. suecicus*
D14	239		-1.3	-9.5	0.84				*E. suecicus*
D13	238		-1.1	-8.4	0.54				*E. suecicus*
D12	237	77.6	-2.2	-10.1	0.62	-23.9	972	-3.2	*E. suecicus*
D11	236		-2.3	-10.0	0.52				*E. suecicus*
D10	235		-1.5	-10.3	0.64				*E. suecicus*
D9	234	61.8	-1.9	-10.4	0.67	-23.8	1105	-9.9	*E. suecicus*
D8	233	79.2	-1.9	-10.3	0.43		762	-13.1	*E. suecicus*
D7	232	74.8	-2.3	-10.7	0.99	-24.4	925	-9.6	*E. suecicus*
D6	231		-1.9	-10.4	0.7				*E. suecicus*
D5	230	61.4	-2.2	-11.4	0.68	-23.7			*E. suecicus*
D4	229	94.2	-2.0	-9.9	0.32		536	-12.0	*E. suecicus*

D3	228	96.36	-0.5	-11.2	0.5	-23.9	264	-14.9	*E. suecicus*
D2	227		-0.3	-11.5	0.47		179	-15.2	*E. suecicus*
D1	226		-0.7	-11.6	0.45				*E. suecicus*
J2-25	225.8	74	-0.9	-12.4	0.37	-24.4	494	-14.4	*E. suecicus*
J47	225	43	-1.2	-12.9	0.26				*E. suecicus*
J2-24	224.8		-1.6	-11.5	0.33				*E. suecicus*
J46	224	43	-1.3	-12.8	0.42	-25.1			*E. suecicus*
J45	223	61.8	-1.9	-12.7	0.31				*E. suecicus*
J2-23	222.8	60	-1.6	-12.3	0.25	-24.3			*E. suecicus*
J44	222	46	-3.0	-10.3	0.32				*E. suecicus*
J2-22	221.8		-1.4	-12.6	0.29				*E. suecicus*
J43	221	33	-3.4	-10.3	0.28	-25.6			*E. suecicus*
J2-21	220.8		-1.2	-11.6	0.74				*E. suecicus*
J42	220	64	-1.4	-12.6	0.4				*E. suecicus*
J2-20	219.8		-0.9	-11.7	0.17		532	-19.3	*E. suecicus*
J41	219	56.8	-2.4	-11.0	0.57				*E. suecicus*
J2-19	218.8	84	-1.0	-11.4	0.55	-24.5	931	-18.6	*E. suecicus*
J40	218	49	-0.9	-12.3	0.46				*E. suecicus*
J39	217	65	-1.0	-12.6	1.6				*E. suecicus*
J2-18	216.5	91	-0.7	-11.7	0.41	-23.9	281	-15.8	*E. suecicus*
J38	216	62	-1.4	-12.8	0.5				*E. suecicus*
J37	215	48	-1.3	-13.0	0.39				*E. suecicus*
J2-17	214.5	80.7	-1.3	-12.7	0.53	-24.4	406	-11.6	*E. suecicus*
J36	214	42	-0.9	-12.8	0.5				*E. suecicus*

J2-16	213.5		-2.5	-13.4	0.2				*E. suecicus*
J35	213	20.1	-1.8	-13.4	0.22	-26.7			*E. suecicus*
J34	212	28	-1.8	-14.1	0.39	-25.7			*E. suecicus*
J2-15	211.5		-2.5	-13.7	0.21				*E. suecicus*
J33	211	20	-3.2	-14.1	0.2	-27.0	3145	-13.3	*E. suecicus*
J2-14	210.5		-4.3	-13.8	0.13				*E. suecicus*
J32	210	18.7	-3.3	-11.7	0.1				*E. suecicus*
J31	209	50.9	-2.0	-13.8	0.45		6048	-13.2	*E. suecicus*
J2-13	208.5		-3.3	-14.2	0.14				*E. suecicus*
J30	208	17	-4.1	-12.8	0.18				*E. suecicus*
J2-12	207.5		-2.2	-13.9	0.24				*T. tangshanensis*
J29	207	20.6	-3.3	-13.8	0.12	-26.2	1210	-13.4	*T. tangshanensis*
J2-11	206.5	41.8	-4.5	-14.3	0.11				*T. tangshanensis*
J28	206	16	-2.8	-14.7	0.23	-26.6	6532	-13.0	*T. tangshanensis*
J27	205	51.1	-2.8	-14.7	1.12		4839	-10.1	*T. tangshanensis*
J26	204	16.5	-1.8	-14.8	0.14	-26.2			*T. tangshanensis*
J25	203	18	-3.6	-14.6	0.13	-26.1	1935	-2.7	*T. tangshanensis*
J2-10	202.7	50.2	-6.8	-15.7	0.92	-24.8			*T. tangshanensis*
J24	202		-3.8	-15.1	0.17		3871	-1.8	*T. tangshanensis*
J23	201		-3.1	-15.3	0.19		8468	-1.0	*T. tangshanensis*
J2-9	200.2		-5.2	-16.7	0.25				*T. tangshanensis*
J22	200	37.2	-4.5	-15.2	0.38	-25.7	4355	1.0	*T. tangshanensis*
J10	199	17.3	-3.0	-16.7	0.25	-25.4			*T. tangshanensis*
J2-8	198.5		-2.8	-14.2	0.24				*T. tangshanensis*

J9	198	19	-2.6	-17.8	0.32	-24.3	7500	-3.7	*T. tangshanensis*
J8	197	29	-2.7	-16.6	0.38	-24.7	3145	-5.0	*T. tangshanensis*
J2-7	196.5		-3.0	-14.4	0.4				*T. tangshanensis*
J7	196	14	-2.8	-16.2	0.55	-24.7			*T. tangshanensis*
J2-6	195.5		-2.7	-13.4	0.6				*T. tangshanensis*
J6	195	19	-2.1	-15.1	0.83				*T. tangshanensis*
J5	194	22	-1.3	-14.4	0.87	-25.0	6581	-10.4	*T. tangshanensis*
J2-5	193.5		-2.0	-14.3	1.21				*T. tangshanensis*
J4	193	56.9	-2.2	-14.9	1.02	-24.7			*T. tangshanensis*
J2-4	192.5		-1.7	-13.9	1.89				*T. tangshanensis*
J3	192	53	-1.9	-14.7	1.75	-24.4	1476	-12.5	*T. tangshanensis*
J2-3	191.6		-1.8	-14.1	1.95				*T. tangshanensis*
J2	191	35.8	-1.5	-14.8	2.14	-24.5			*T. tangshanensis*
J2-2	189.6	73.7	-1.8	-14.5	1.09				*T. tangshanensis*
J1	189	50.7	-1.4	-14.6	1.85	-24.2	7742	-11.5	*T. tangshanensis*
25-45	187	38.9	-1.9	-13.2	2.63	-24.3	484	-4.9	*T. tangshanensis*
J2-1	186.6		-3.7	-11.1	1.5				*T. tangshanensis*
m10	186	88.8	-0.9	-10.3	0.49	-23.9	1856	-9.2	*T. tangshanensis*
25-44	186			-9.5					*T. tangshanensis*
m9	185	91.6	-1.2	-11.1	0.41	-24.1			*T. tangshanensis*
m8	184		-0.7	-11.5	0.42				*T. tangshanensis*
m7	183		-0.6		0.48	-24.0			*T. tangshanensis*
25-46	182			-8.1					*T. tangshanensis*
m6	182		-0.2	-11.3					*T. tangshanensis*

m5	181		-0.4	-12.0	0.45	-23.4			*T. tangshanensis*
m4	180		-1.3		0.47				*T. tangshanensis*
m3	179		-1.2	-11.3	0.4	-24.5			*T. tangshanensis*
m2	178	84.5	-1.9	-12.9	0.73	-24.6			*T. tangshanensis*
m1	177		-1.7	-13.4	0.34				*T. tangshanensis*
25-47	177		-1.2	-10.9					*T. tangshanensis*
25-48	169	97.2	-1.3	-11.6	0.19	-25.7	234	-5.2	*T. tangshanensis*
25-49	161	91.4	-2.4	-11.7	0.24	-27.2	325	-14.0	*T. tangshanensis*
25-50	159	88.8	-2.6	-13.3	0.22	-23.4	432	-8.9	*T. tangshanensis*
25-51	155	83.2	-2.8	-15.5	0.15	-25.2	281	-4.1	*T. tangshanensis*
25-52	149	86.6	-1.0	-10.0	0.19	-26.9	232	-5.8	*T. tangshanensis*
25-53	145		-0.3	-8.7					*T. tangshanensis*
25-54	134	97.6	-2.0	-6.5	0.05	-27.5	293	11.0	*T. tangshanensis*
25-55	131	96.7							*T. tangshanensis*
25-56	127	95					750	4.8	*T. tangshanensis*
25-57	124	94.5	-1.9	-7.5	0.58	-27.0			*T. tangshanensis*
25-58	121		-2.3	-5.6				4.9	*T. tangshanensis*
25-59	118	97.2	-1.4	-9.0	0.08	-26.3	369	7.8	*T. tangshanensis*
25-60	114							11.8	*T. tangshanensis*
25-61	109	95					193		*T. tangshanensis*
25-62	104	99.2			0.06	-25.3	498	9.2	*T. tangshanensis*
25-63	99	97.6			0.13	-25.3	1424	12.6	*T. tangshanensis*
25-64	97								*T. tangshanensis*
25-65	95	98.6			0.10	-25.2	264	0.4	*T. tangshanensis*

25-66	94							*T. tangshanensis*
25-67	93	98.4		0.16	-24.7	117	-1.6	*T. tangshanensis*
25-68	92							*T. tangshanensis*
25-69	90	98.3		0.11	-25.7	23	4.3	*T. tangshanensis*
25-70	89			0.18	-25.1			*T. tangshanensis*
25-71	88							*T. tangshanensis*
25-72	82	99.3		0.02	-27.2	100	5.5	*T. tangshanensis*
25-73	79							*T. tangshanensis*
25-74	76.5	99.3		0.03	-24.8	3040	8.6	*T. tangshanensis*
25-43	75.5							*T. tangshanensis*
25-75	74	97.1		0.04		176	7.6	*T. tangshanensis*
25-42	73							*T. tangshanensis*
25-76	69	98.3		0.19	-24.6	117	16.0	*T. tangshanensis*
25-77	64	99.2		0.10	-24.9	1072	5.2	*T. tangshanensis*
25-78	56							*T. tangshanensis*
25-41	55	99.1		0.09	-25.4	94	-0.7	*T. tangshanensis*
25-79	52	98.2		0.18	-24.6			*T. tangshanensis*
25-40	50	99		0.14	-25.4	47	1.6	*T. tangshanensis*
25-80	47							*T. tangshanensis*
25-39	45							*T. tangshanensis*
25-81	42	87.3		0.14	-27.2	697	4.9	*T. tangshanensis*
25-38	40	93.2		0.16	-26.7	55	15.9	*T. tangshanensis*
25-82	37	97.3		0.02	-25.8			*T. tangshanensis*
25-37	35	97.06		0.23	-25.4	47	3.8	*T. tangshanensis*

25-36	30	99.8		0.07	-25.2	41	5.2	*T. tangshanensis*
25-35	25	99.8		0.04	-25.8	15	6.9	*T. tangshanensis*
25-34	20	95.6		0.07	-27.5	205	12.5	*T. tangshanensis*
25-33	15	93.4		0.36	-23.5	353	6.9	*T. tangshanensis*
25-32	10	93.2		0.10	-27.8			*T. tangshanensis*
25-31	5	93.2		0.08	-28.5	432	15.9	*T. tangshanensis*
25-30	0	87		0.18	-27.0	143	14.0	*T. tangshanensis*
25-29	-2		-2.7					*barren interval*
25-28	-3		-2.93					*barren interval*
25-27	-5		-2.29					*barren interval*
25-26	-7		-3.23					*barren interval*
25-25	-9		-3.78					*barren interval*
25-24	-11		-3.11					*barren interval*
25-23	-13		-3.12					*barren interval*
25-22	-15		-6.18					*barren interval*
25-21	-16		-2.12					*P. obsesus*
25-20	-20		-1.76					*P. obsesus*
25-19	-25		-2.01					*P. obsesus*
25-18	-30		-2.25					*P. obsesus*
25-17	-35		-1.88					*P. obsesus*
25-16	-40		-2.09					*P. obsesus*
25-15	-45		-2.09					*P. obsesus*
25-14	-50		-2.31					*S. extensus*
25-13	-55		-1.89					*S. extensus*

25-12	-60	-1.99	*S.bilobatus*
25-15	-45	-2.09	*S.bilobatus*
25-14	-50	-2.31	*S.bilobatus*
25-13	-55	-1.89	*S.bilobatus*
25-12	-60	-1.99	*S.bilobatus*

Table 2.2 Carbonate carbon isotope, oxygen isotope, pyrite contents and pyrite isotope data from the Namgyo section. Information about the age is note presented due to poor biostratigraphy in the Yeongwol.

Sample	Height (m)	$\delta^{13}C$ (‰)	$\delta^{18}O$ (‰)	Pyrite (ppm)	$\delta^{34}S_{Py}$ (‰)
NG87	99.2	0.5	-10.8	93	-1
NG86	98.2	0.3	-11.7	127	0.6
NG85	97.2	0.2	-11.9	192	12.5
NG84	96.2	0.8	-8.5	122	5.4
NG83	95.2	0.5	-8.6	128	5.1
NG82	94.1	0.4	-8.5		
NG81	93.1	-0.3	-12		
NG80	92.1	-0.4	-10.4	1004	-9.3
NG79	91.1	-0.5	-9.8	134	-0.9
NG78	90.1	-0.6	-9.6		
NG77	89.1	-0.7	-9.9	64	16.3
NG76	87.6	0.6	-10.8	91	5.8
NG75	86.4	-2.1	-14.7	398	-3.9
NG74	85.4	-0.1	-7.9	97	-4.5
NG72	83.4	0.5	-8.6	114	3.2
NG71	81.4	-0.1	-10.4	317	5.3
NG70	80.4	-0.2	-0.1		
NG69	79.4	-0.3	-8.8	139	13.3
NG68	78.4	0.1	-8.4	767	-1.7
NG67	77.4	-0.7	-9.4	50	14.1
NG66	76.4	-1.2	-9.1	629	0.8
NG65	75.4	-0.7	-9.2	174	10.5
NG64	74.4	-0.6	-7.7	11	1.5
NG63	73.4	0.9	-6.4	91	2.9
NG62	72.4	0.3	-9		
NG61	71.4	-2.4	-13.4		
NG60	70.8	0.3	-5.9		
NG59	69.1	-0.2	-8	271	-6.4
NG58	68.6	-0.3	-9.7		
NG57	67.6	-0.5	9.4	132	18.6

NG56	66.6	-0.7	-8.8	639	3.9
NG55	65.6	-0.6	-8.5	35	8.9
NG54	64.6	-0.7	-9.1	125	25.7
NG53	53.1	-0.2	-7.6		
NG52	52.4	0.5	-5.9	19	13.2
NG51	51.4	1.0	-6.6	18	13.3
NG50	50.4	0.1	-7.7	44	3.5
NG49	49.3	0.0	-9.9	112	4.5
NG48	48.3	0.0	-7.2	86	11.6
NG47	47.3	-0.2	-5.5	63	1
NG46	46.3	-0.6	-9.4	109	9.7
NG45	45.3	-0.5	-9.1	252	13.7
NG44	44.3	-0.1	-8.1		
NG43	43.3	-0.3	-10.1	155	-9.5
NG42	42.3	-0.1	-7.5	36	2.8
NG41	40.5	-1.2	-11.4		
NG40	39.5	-0.2	-8.9	234	-3.3
NG39	38.5	-0.3	-9.6	55	11.6
NG38	37.5	-0.3	-9		
NG37	36.3	-0.2	-8.9	46	8.2
NG36	35.4	-0.1	-8.8	30	3.6
NG35	34.4	-0.3	-8.7		
NG34	33.4	0.1	-9.3	113	0.8
NG33	32.4	0.0	-8.6	50	7.4
NG32	31.4	0.1	-8.3		
NG31	30.4	0.1	-8.2		
NG30	29.5	-0.3	-8.7	55	14.5
NG29	28.4	-0.5	-9.4		
NG28	27.2	-0.4	-9.5	16	10
NG27	26.2	-0.4	-8.6	19	5.4
NG26	25.2	-0.6	-8.8	12	12
NG25	24.2	-0.3	-9.7	31	3.9
NG24	23.2	-0.5	-8.9		
NG23	22.2	-0.5	-8.7		
NG22	21.2	-0.7	-9.1	135	1.3
NG21	20.2	-1.0	-9.3		
NG20	19.4	-1.1	-9.5	105	0.7

NG19	18.4	-0.9	-9.4	74	0.3
NG18	17.4	-0.5	-10.1	34	11.8
NG17	16.4	-0.9	-10.4	140	0.4
NG16	15.4	-0.9	-9.7	126	8
NG15	14.4	-0.6	-7.9		
NG14	13.4	-0.8	-10.7		
NG13	12.4	-0.7	-11.2	115	6.3
NG12	11.4	-0.5	-10.3	44	1.8
NG11	10.4	-0.5	-9.7	54	2.7
NG10	9.4	-0.9	-9.2	56	13
NG9	8.4	-0.6	-8.9	54	10
NG8	7.4	-0.5	-8.9	101	-1.2
NG7	6.4	-0.8	-8.7	72	-2.2
NG6	5.4	-0.9	-9.3	36	3.6
NG5	4.1	-1.6	-9.5	164	6.8
NG4	3	-1.4	-8.5	50	5.1
NG3	2	-1.2	-8.7	91	12.6
NG2	1	-0.5	-7.8		
NG1	0	-1.2	-9.8	91	6.1

Table 2.3 Carbonate carbon isotope, oxygen isotope, pyrite contents and pyrite isotope data from the Yeonduk section.

Sample	Height (m)	$\delta^{13}C$ (‰)	$\delta^{18}O$ (‰)	Pyrite (ppm)	$\delta^{34}S_{Py}$ (‰)
YD43	43	-1.0	-7.4		
YD41.5	41.5	-1.2	-7.3		
YD40	40	-1.0	-6.0		
YD39	39	-1.1	-5.8	228.1	10.3
YD38	38	-1.3	-6.3		
YD37	37	-1.2	-5.7	41.5	7.5
YD36	36	-1.4	-7.5		
YD35	35	-1.1	-6.1		
YD34	34	-1.6	-9.5		
YD33	33	-1.3	-6.0	121.0	-1.9
YD32	32	-1.2	-7.0		
YD31	31	-0.9	-6.1	214.3	6.2
YD30	30	-1.2	-6.7		
YD29	29	-1.0	-6.5	58.8	5.8
YD28	28	-1.3	-6.6		
YD27	27	-1.2	-6.3	65.7	6.2
YD26	26	-1.9	-7.0		
YD25	25	-1.5	-6.1	24.2	3.4
YD24	24	-1.9	-5.8		
YD23	23	-2.1	-7.3	31.1	9.3
YD22	22	-1.2	-6.6		
YD21	21	-1.9	-7.8	17.3	2.6
YD20	20	-0.9	-5.9		
YD19	19	-0.7	-5.9	89.9	1.6
YD18	18	-0.9	-7.0		
YD17	17	-1.2	-6.5	20.7	9.7
YD16	16	-1.7	-7.0		
YD15	15	-1.0	-6.6	114.1	3.7
YD14	14	-1.6	-6.6		
YD13	13	-0.5	-7.0	179.7	4.6
YD12	12	-1.2	-7.1		
YD11	11	-1.2	-7.1	155.5	6.5

YD10	10	-1.4	-7.1		
YD9	9	-2.3	-6.0		
YD8	8	-2.2	-8.7		
YD7	7	-1.4	-8.7	127.9	9.6
YD6	6	-2.8	-8.5		
YD5	5	-3.6	-7.6	518.4	8.7
YD4	4	-2.7	-9.7		
YD3	3	-1.6	-12.7	183.2	0.8
YD2	2	-1.0	-6.4		
YD1	1	-1.7	-7.0	232.6	6.7

2.5.3 δ¹³C correlation with other regions

Given that carbon isotope data were analyzed in the Yeongheung Formation and Makgol Formation, and biostratigraphy has been re-established in the Taebaek and Yeongwol areas, it is necessary to update the MDICE chemostratigraphy by correlating δ¹³C values with other regions. Comparison of the carbon isotope data with other regions can help determine which section exhibits a stronger correlation with the global trend and is crucial in explaining the local differences observed between the Taebaek and Yeongwol. This correlation is mainly focused on the Taebaek Group due to the relatively reliable biostratigraphy framework.

Sections in the North China, where the Darriwilian carbon isotope curve has recently been extensively studied (Figure 2.13A; Zhang and Munnecke, 2016; Jing et al., 2022), were deposited in the same craton as the Taebaeksan Basin and have a similar conodont biozone. Carbon isotope data from the Tao-112 drillcore in North China reveals a significant -6‰ negative excursion in the lower part of the *T. tangshanensis* zone (Jing et al., 2022). Similarly, carbon isotope data from the composite of the Hejin and Linfen outcrop sections (Guo et al., 2014) and the Yangjikan outcrop (Zhang and Munnecke, 2016) also exhibit a -4‰ negative excursion in the lower *T. tangshanensis* zone (Figure 2.13A). These negative excursions correlate well with the light isotope compositions observed in the lower member of the Makgol Formation. From the upper *T. tangshanensis* zone to the *E. suecicus* zone, carbon isotope values in these North China sections show an increasing trend, reaching 0‰. This pattern represents the MDICE records in the Sino-Korean Block (Bang & Lee, 2020; Jing et al., 2022). However, no negative excursion is observed around this interval in the North China sections.

Carbon isotope excursion records from the Laurentia (North America at present) are valuable for chronostratigraphic correlation due to well-constrained conodont biostratigraphy and sedimentology framework. In the Great Basin, Edward & Saltzman (2014) reported δ¹³C$_{Carb}$ values from the Shingle Pass section, revealing a significant -4‰ negative excursion in the early Darriwilian. Because the carbon isotope data in this area cover the Tremadocian to early Darriwilian interval, the MDICE record

57

was not specifically presented (Figure 2.13B). Data from Western Newfoundland show a -1‰ negative excursion in the early Darriwilian, followed by a steady increasing trend from the middle Darriwilian Figure 2.13B; Thompson and Kah, 2012; Kah et al., 2016).

Data from the Clear Spring section in Maryland was selected as a representative section in the Laurentia (Young et al., 2016; Saltzman & Edward, 2017). This section was deposited in a warm and shallow marine platform environment and exhibits clear records of both LDNICE and MDICE. The LDNICE record in the Clear Spring section extends from the upper *Histiodella sinuosa* zone to the lower *H. holodentata* zone (Figure 2.13B). The MDICE record, on the other hand, covers the upper *H. holodentata* zone and the lower *Cahagnathus sweeti* zone. The *H. holodentata* zone corresponds to the *T. tangshanensis* biozone in North China, indicating a good temporal correlation between the negative excursion observed in the lower member of the Makgol Formation and the LDNICE records in the Laurentia. However, negative excursion is not reported in the upper interval of the *H. holodentata* zone (Figure 2.13B).

The LDNICE and MDICE records have been reported in both shelf and basinal environments in Baltica. $\delta^{13}C_{Carb}$ curves from the Mehikooma 421 drillcore in Estonia (Ainsaar et al., 2010) and the Mora 001 drillcore (Lehnert et al., 2014) show -1‰ negative excursion in the *Y. crassus* zone and represent a steady increasing trend from the *E. pseudoplanus* to *the E. suecicus* zone (Figure 2.13C). $\delta^{13}C_{Carb}$ data from Tingskullen cores in Sweden (Wu et al., 2017) show no negative excursion, but positive excursion was observed in the *E. pseudoplanus* and *E. suecicus* zones (Figure 2.13C).

Comparing the carbon isotope curve with other regions, the negative excursion of the paired carbon isotope data in the lower member of the Makgol Formation represent good agreement with LDNICE record reported in other regions. Additionally, the increasing trend of $\delta^{13}C_{Carb}$ in the *E. suecicus* zone is observed globally, further supporting a consistent pattern. Therefore, carbon isotope pattern from the middle member of the Makgol Formation indicate the MDICE record of the Joseon Supergroup. However, the negative excursion in the upper *T. tangshanensis* zone in the Seokgaejae section contrasts

with the findings in other regions, suggesting that the $\delta^{13}C_{Carb}$ shift observed in the Jigunsan Formation represents a local trend rather than a global signal, and explanation for this negative excursion is required.

2.5.4 Local influence for carbon isotope curve in the middle Jigunsan Formation.

The negative excursion in the Jigunsan Formation is not observed in the other regions including the Yeongwol Group, suggesting that it is a local signal. Therefore, various sedimentological observation and geochemical data should be considered to interpret this isotopic pattern. According to sedimentological and paleontological research for the Joseon Supergroup, Taebaek area was likely to be deposited in a semi-restricted environment during the early Paleozoic (Lee et al., 2001; Woo and Chough, 2007; Choi, 2011; Byun et al., 2018; Woo et al., 2023). The depositional environmental changes observed in the lower to middle part of the Jigunsan Formation is deepening of water depth, slow sedimentation rates (Choi et al., 2004; Woo and Chough, 2007). Redox condition in the Jigunsan Formation is interpreted as the water column might be in a suboxic condition and anoxic conditions existed below the sediment-water interface (Byun et al., 2018). Pyrite contents and isotopic values increase in the lower to middle Jigunsan Formation (Figure 2.14), indicating increased degradation of organic matter by sulfate reducers. Organic carbon isotope composition in the Jigunsan Formation show paired negative excursion with carbonate carbon (Figure 2.14), indicating that isotope composition of dissolved inorganic carbon in the water column become light during the deposition.

Based on sedimentological evidence and geochemical data observed in the Jigunsan Formation (Figure 2.14; Woo and Chough, 2007; Byun et al., 2018), the best explanation for the negative excursion is an increase in organic matter decomposition due to decreased sedimentation rate. Enhanced organic matter degradation promote the production of DIC with light isotopic compositions, which was then introduced into the water column via benthic fluxes, resulting in lighter DIC isotopic compositions of the water column. As sedimentation rates slow, the increased exposure time of organic matter to electron

acceptors in the sediment leads to enhanced decomposition of organic matter. Furthermore, for the light isotopic composition of DIC in pore water to influence the water column, it must be introduced into the water column by benthic flux, and slow sedimentation rates allow for greater input of light DIC (Figure 2.14; Ding et al., 2021). The increase in organic matter decomposition with decreasing sedimentation rates is likely to mainly driven by sulfate reducers rather than aerobic bacteria in the Jigunsan Formation, which is supported by increased pyrite content and isotopic values (Figure 2.14). Previous studies have also investigated the relationship between sedimentation rate and suggested a trend that slow sedimentation rate leads to decrease of TOC due to enhanced degradation of organic matter in oxic to suboxic environment (Stein, 1986; Stein; 1990; Ding et al., 2015), also supporting a decrease trend of TOC in this interval.

It is important to note that the Taebaek area was deposited in a restricted environment and has a small DIC reservoir size. In the open ocean environment, the benthic flux can only affect the DIC isotope composition around the seafloor. However, since Taebaek was a restricted environment and have small DIC reservoir size (Figure 2.15; Woo and Chough, 2007; Choi, 2011; Byun et al., 2018), it is plausible that benthic flux could have spread throughout the water column. Therefore, input of benthic flux can explain a concomitant decrease in organic carbon isotopic values.

The second explanation for the negative excursion is a decrease in local productivity due to marine acidification. A recent study using boron isotopes suggests that during the deposition of the Jigunsan Formation, the Taebaek area experienced intense rainfall and subsequent ocean acidification, which may have led to biotic turnover (Bang, 2023). Indeed, marine acidification can lead to a decrease in local productivity, which in turn can disrupt the local isotopic system and potentially decrease the isotopic composition of DIC. The decline in marine productivity has a significant impact on the decrease in TOC, thus marine acidification can explain TOC trend within this interval (Byun et al., 2018). While it is not certain how much ocean acidification can reduce marine productivity, it remains a potential explanation for the carbon isotope excursion in the Jigunsan Formation.
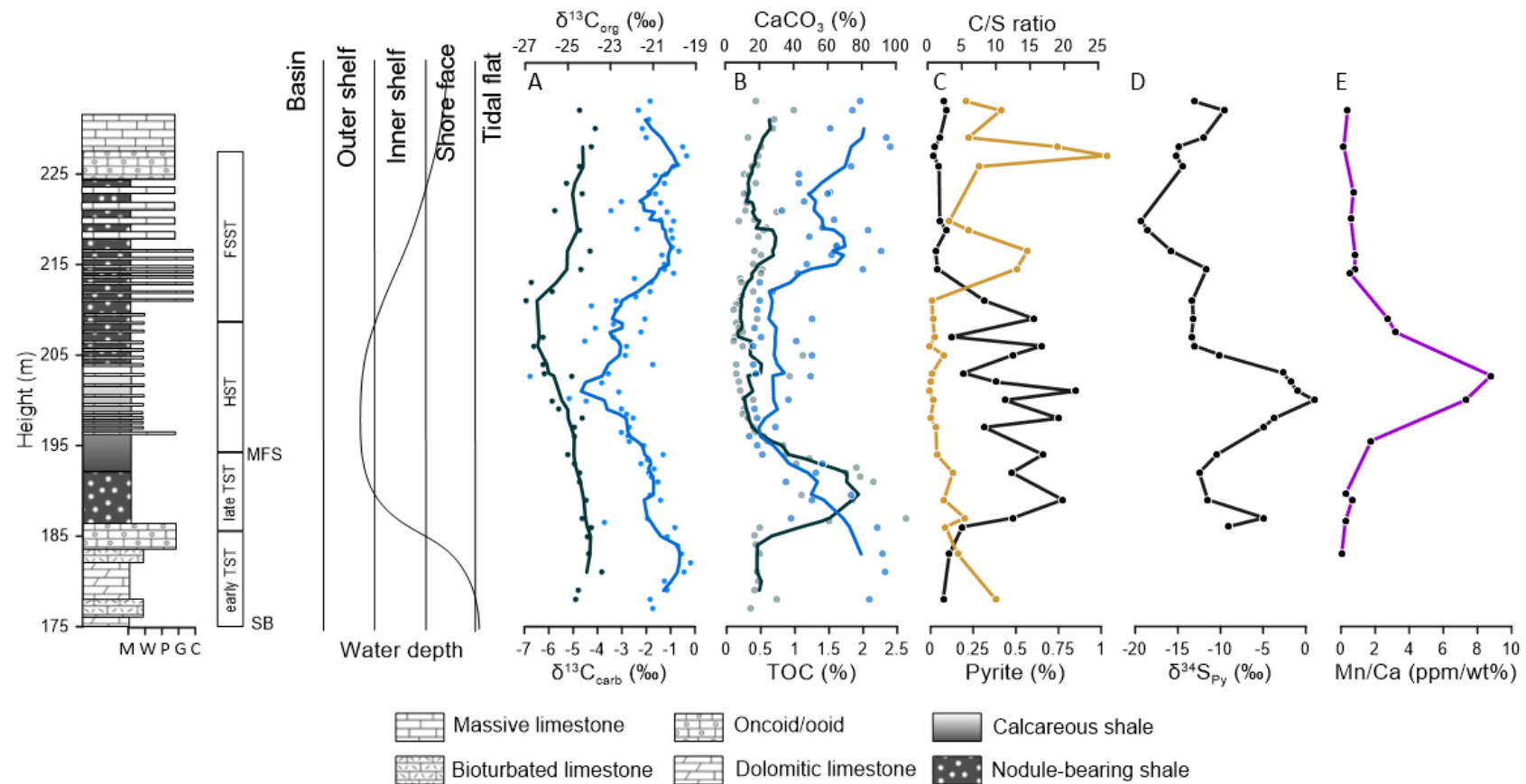
Figure 2.14. Detailed lithology, sequence stratigraphy, water depth curve, carbonate carbon isotope, organic carbon isotope, total organic carbon, carbonate contents, weight ratio of organic carbon and pyrite sulfur, pyrite contents, and pyrite sulfur isotope values in the uppermost Makgol and Jigunsan formations, Seokgaejae section. Mn concentration data are from Bang (2023).
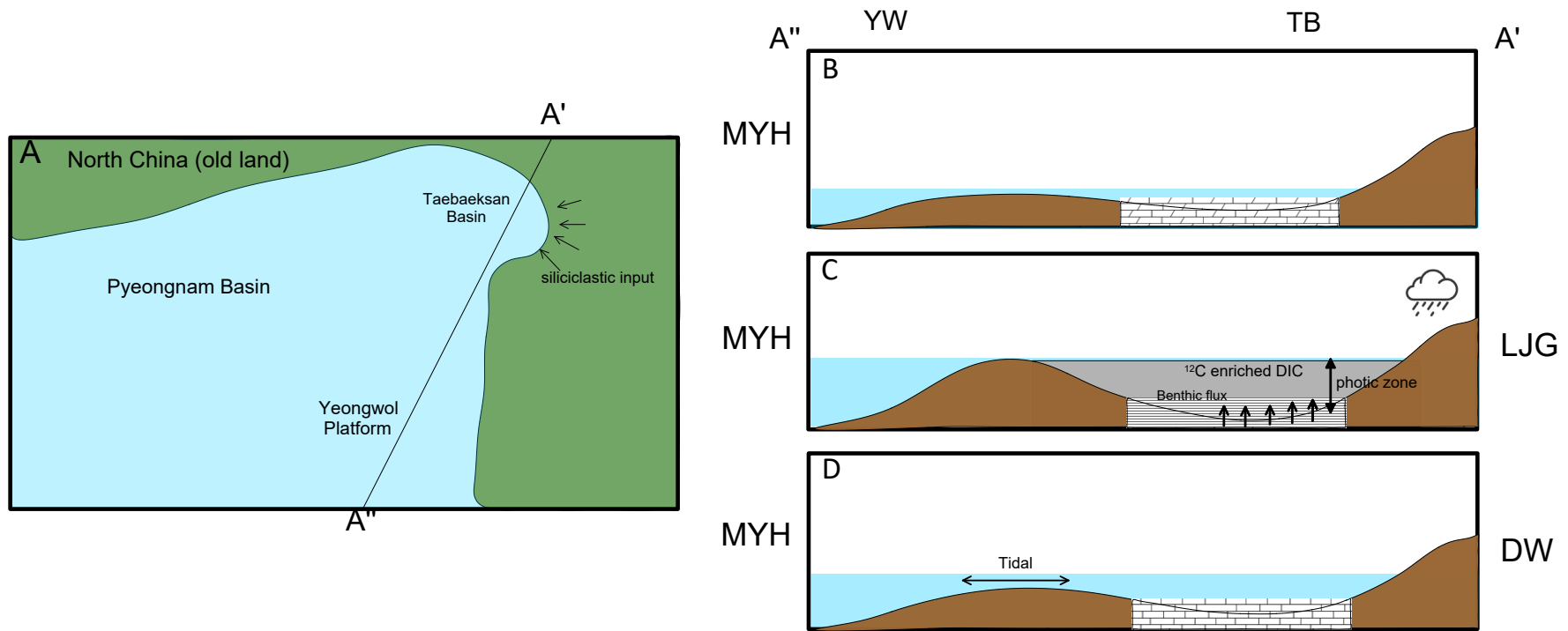
Figure 2.15 Basin evolution and schematic paleoceanography model for the epeiric sea setting (modified after Choi, 2011) in the Taebaeksan Basin during the middle Darriwilian. (A) Basin geometry of the Taebaeksan Basin in the early Paleozoic (modified after Woo et al., 2023). (B) Shallow subtidal to peritidal depositional environment in the upper part of the Makgol Formation composed of dolomitic limestone. (C) Rapid deepening led to decrease of sedimentation rate in the Taebaek, triggering enhanced organic matter degradation by anaerobic bacteria and benthic flux input. (D) Shallowing of water depth decreases benthic flux input to the water column and resumes carbonate deposition in the Taebaek. Abbreviation: TB=Taebaek; YW=Yeongwol; UMG=Upper Makgol; LJG=Lower Jigunsan; DW=Duwibong; MYH; Middle Yeongheung.

2.5.5 Effect of depositional environments on the pyrite sulfur isotopic record

In the upper Joseon Supergroup, pyrite isotope values show different trends in the Taebaek and Yeongwol areas. The $\delta^{34}S_{Py}$ data from the Taebaek area represent a stratigraphic trend (Figure 2.9), while the data from the Yeongwol area do not exhibit a distinct stratigraphic pattern (Figure 2.11) In addition, the $\delta^{34}S_{Py}$ values are less scattered than those in the Yeongwol Group, and the average pyrite sulfur isotopic composition in the Yeongwol Group is heavier than that in the Taebaek Group. These different $\delta^{34}S_{Py}$ trends and values reflect the change in the depositional environment of the two areas.

In the oxic water column, $\delta^{34}S_{Py}$ values in carbonate rocks are mainly determined by sea level change and sedimentation rate. For example, shallowing and increased sedimentation rates generally increase $\delta^{34}S_{Py}$ values due to increased availability of organic matter to sulfate reducers and progressive sulfate reduction in more closed pore water systems (Pasquier et al., 2017, 2021). Therefore, the $\delta^{34}S_{Py}$ trend in the Seokgaejae section can be interpreted as a change in water depth and sedimentation rate during deposition.

The pyrite isotope data of the Joseon Supergroup show similar trends to the changes in water depth, except for the middle part of the Jigunsan Formation (Figure 2.9; Kwon et al., 2006; Woo & Chough, 2007). Above the hiatus layer in the lower member of the Makgol Formation, the depositional environment changes from peritidal to subtidal (Cho et al., 2021; Lee et al., 2022) with subaerial exposure. In this interval, the pyrite isotope value decreases from 15 to 5‰, supporting transition from peritidal to subtidal environment. The middle and upper members of the Makgol Formation are shallow subtidal to peritidal environments, and the sedimentation rate is relatively high. Heavy sulfur isotopic compositions of pyrite between 5 - 15‰ reflects shallow environmental setting. Above the sequence boundary, $\delta^{34}S_{Py}$ decreases in the uppermost Makgol and the lowermost Jigunsan formations indicate rapid sea-level rise of the platform (Woo & Chough, 2007).

However, although the water depth of the middle Jigunsan Formation is relatively deep (Woo & Chough, 2007; Byun et al., 2018), pyrite isotope values show a positive excursion of +10‰, indicating

enhanced availability of labile organic matter to sulfate reducers (Figure 2.14). In this interval, decrease of oxygen concentration in water column and uplift of redox boundary could increase the lability of organic matter for sulfate reducers and decrease the fractionation size. In the upper part of the Jigunsan Formation, oxygenation of the water column decreases pyrite isotope values (Figure 2.14). In the Duwibong Formation, an upward increase in $\delta^{34}S_{Py}$ values reflects a decrease in sea level and an increase in sedimentation rate.

The depositional environment in the Yeongwol Group was shallower than that in the Taebaek Group, and the water depth curve is relatively invariant (Figure 2.11; Yoo & Lee, 1997; Kwon, 2012; Kwon & Kwon, 2020). Therefore, the relatively heavier pyrite-sulfur isotopic composition in the Yeongwol Group can be explained by the better availability of labile organic matter than that in the Taebaek Group. The lack of stratigraphic pattern in $\delta^{34}S_{Py}$ values is due to the invariant water depth (Figure 2.11; Yoo & Lee, 1997; Kwon, 2012; Kwon & Kwon, 2020). In addition, the shallow environment promoted sediment reworking by storm forcing and bioturbation, leading to relatively high point-to-point variability in $\delta^{34}S_{Py}$ values in the Yeongwol Group.

2.6 Conclusion

This study attempt to interpret the differences of the Middle Ordovician carbon isotope curves between the Taebaek and Yeongwol areas based on various sedimentological and geochemical observations. In the Taebaek, the paired carbon isotope values in the middle Jigunsan Formation show a prominent negative excursion but no corresponding negative excursion is observed in any other regions including Yeongwol, indicating that this carbon isotope pattern reflects local environmental changes. indicating that carbon isotope pattern reflects local environmental changes. Based on the sedimentological and geochemical observations, this carbon isotope trend can be explained by an increase in organic carbon degradation and benthic flux due to low sedimentation rate. The pyrite sulfur isotope trends observed in the Taebaek Group reflect availability of organic matter for sulfate reducers, influenced by fluctuations of water depth and sedimentation rate during the deposition. However, positive excursion of $\delta^{34}S_{Py}$ in the middle Jigunsan Formation indicate an increase in availability due to changes in redox conditions rather than water depth. In contrast, the sulfur isotope compositions in the Yeongwol Group exhibit relatively heavier values without a clear stratigraphic trend, reflecting relatively shallow and invariant water depths. This study indicate that effect of depositional environment can be significant to isotopic record, especially restricted environment.

.

Chapter 3. Responses of the biogeochemical sulfur cycle to Early Permian tectonic and climatic event

3.1 Introduction

The late Paleozoic was a period of dynamic environmental and biological changes. The evolution of land plants and the extensive development of rainforests enhanced organic matter burial (Cleal et al., 2005, Montañez & Poulsen, 2013; Montañez et al., 2016; Wilson et al., 2017) and the accretion of continental blocks accelerated the rates of silicate weathering and CO_2 consumption (Nelsen et al., 2016; Goddéris et al., 2017). Such perturbations of the global carbon cycle, evidenced by the well-established increase in the carbonate and organic carbon $\delta^{13}C$ values (Korte et al., 2005; Grossman et al., 2008; Koch & Frank, 2011; Chen et al., 2018), drove multiple episodes of glaciation (Isbell et al., 2003; Scheffler et al., 2003, 2006; Fielding et al., 2008a, b; Frank et al., 2008; Grader et al., 2008). The causes and consequences of the late Paleozoic ice age might be also intimately linked to the biogeochemical cycle of sulfur, which plays a pivotal role in regulating redox processes and the availability of essential elements in marine environments. For example, the enhanced burial of organic matter promotes microbial sulfate reduction and concomitant pyrite formation (Berner & Raiswell, 1983), and both tectonics and eustasy are key determinants of the pyrite burial rate and the magnitude of sulfur isotope fractionation on a global scale (Halevy et al., 2012; Leavitt et al., 2013). However, the response of the sulfur cycle to late Paleozoic environmental changes remains largely unexplored.

Secular variations in the Phanerozoic sulfur cycle suggest that the Carboniferous to Permian is characterized by relatively high seawater sulfate levels (~9 mM; Algeo et al.; 2015), a minimum in the seawater sulfate $^{34}S/^{32}S$ ratio (~13‰; Kampschulte et al., 2001; Kampschulte & Strauss, 2004; Wu, 2013; Johnson et al., 2020; Present et al., 2020), and an increase in sulfur isotope fractionation between pyrite and coeval sulfate (Wu, 2013; Leavitt et al., 2013), but most previous studies did not had

stratigraphic resolutions high enough to capture the dynamic nature of the sulfur cycle. Due to the absence of notable sulfur isotope excursions, except for a few scattered sulfur isotope values, a stable sulfur cycle has often been presumed for the late Paleozoic, in particular between the Middle Carboniferous and the end-Permian extinction (Kampschulte & Strauss, 2004). However, using high-resolution brachiopod $\delta^{34}S$ records, Johnson et al. (2020) recently proposed a positive sulfur isotope excursion of seawater sulfate as high as 5‰ in the Late Carboniferous. Similarly, the insufficient resolution may obscure the major perturbations in the geochemical sulfur cycle during the Early Permian, a period marked by the major episodes of the Gondwana glaciation and the closure of the Ural Seaway (Davydov, 2018).

Carbonate-associated sulfate (CAS) and pyrite have been recognized as valuable sulfur isotopic archives of the past sulfur cycles at global and regional scales, respectively (Hurtgen et al., 2002; Sim et al., 2015; Pasquier et al., 2017), but recent studies have also highlighted the potential impact of depositional environments on the CAS sulfur isotope values (Rennie & Turchyn, 2014; Richardson et al., 2019a; Ma et al., 2021). Here, this study examined the high-resolution CAS and pyrite sulfur isotope data from the late Paleozoic carbonate sequence in Svalbard that was deposited near the western end of the Ural Seaway (Figure 3.1), and the Early Permian $\delta^{34}S_{CAS}$ increase superimposed by rapid oscillations reflects both global- and regional-scale changes over the course of the closure of the Seaway. A better understanding of the interconnected nature of the geography, climate, and the sulfur cycle during the late Paleozoic could provide a basis for interpreting sedimentary sulfur isotope records spanning other tectonic and climatic events throughout Earth's history.
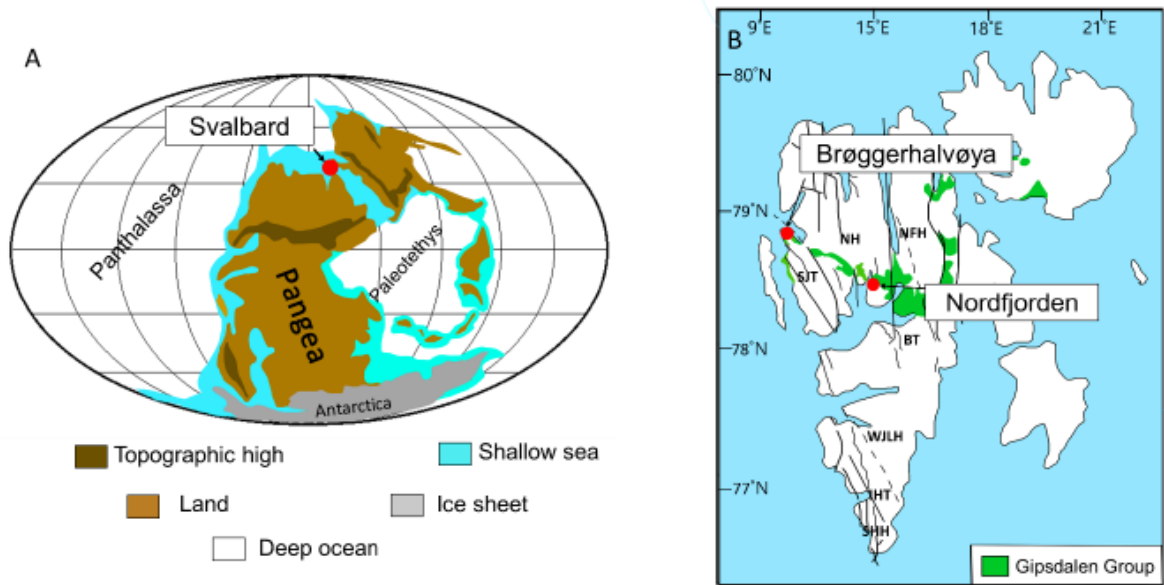
Figure 3.1. (A) Early Permian paleogeographic map showing the location of Svalbard (modified after Blakey, 2008). (B) The position of Brøggerhalvøya and Nordfjorden sections on the present-day Spitsbergen, the main island of the Svalbard archipelago (modified after Dallmann, 1999). BT, Billefjorden Trough; IHT, Inner Hornsund High; NFH, Ny Friesland High; NH, Nordfjorden High; SHH, Sørkapp Hornsund High; SJT, St. Jonsfjorden Trough; WJLH, Wedel Jarlsberg Land High.

3.2 Geological setting

The Late Carboniferous to Early Permian strata in Svalbard, the Gipsdalen Group, were deposited in shallow marine basins located between Euramerica and Siberia (Figure 3.1A). The Gipsdalen Group lies on an erosion surface cutting across basement grabens and syn-rift continental deposits and comprises three half-graben restricted subgroups and the overlying Dickson Land Subgroup (Dallmann, 1999). This study presents data from the Gipsdalen Group exposed at Brøggerhalvøya and Nordfjorden sections, deposited on the St. Jonsfjorden Trough and the Nordfjorden High, respectively (Figure 3.1B).

3.2.1. Brøggerhalvøya section

In the Brøggerhalvøya section of western Spitsbergen (Figure 3.1B), the Gipsdalen Group consists of the Brøggertinden, Scheteligfjellet, Wordiekammen, and Gipshuken formations in ascending order. Since coarse siliciclastic sediments dominate the lowermost Brøggertinden Formation, our study concentrates on the upper three formations. The Scheteligfjellet Formation is predominantly calcareous and composed of grey micrite, yellow-weathered dolomite, and coral boundstone, marking the onset of the stable, shallow marine platform conditions (Saalmann & Thiedig, 2002). The overlying Wordiekammen Formation is subdivided into the Mørebreen and Tyrrellfjellet Members. The lower part of the Wordiekammen Formation, the Mørebreen Member, mostly comprises wackestone, packstone, grainstone, and limestone breccia (Figure 3.4A), deposited under stable shelf conditions (Chwieduk, 2013; Ahlborn & Stemmerik, 2015). Towards the upper end of Mørebreen Member some calcified root remains appears (microcodium; Figures 3.4B and 3.5A). The Tyrrellfjellet Member is largely composed of lime mudstone and dolomite, containing fusulinids representative of late Gzhelian to early Sakmarian age (Figure 3.3; Nilsson & Davydov, 1997). Blomeier et al. (2011) interpreted that it was deposited in shallow subtidal to intertidal and lagoonal environments. The uppermost part of the Gipsdalen Group at the Brøggerhalvøya section comprises the Gipshuken Formation, consisting of dolomite, limestone, anhydrite, and carbonate breccia. This unit is known to have been deposited in warm, shallow marine and sabkha environments (Harland & Geddes, 1997; Sorento et al., 2020). Brachiopods, bryozoans,

conodonts, foraminifers, and palynomorphs indicate its age to be late Sakmarian to early Artinskian (Figure 3.3; Nilsson & Davydov, 1997; Harland & Geddes, 1997; Buggisch et al., 2001; Lee, 2013).

3.2.2 Nordfjorden section

  The Nordfjorden section in central Spitsbergen (Figure 3.1B) represents deposition on the topographic high between St. Jonsfjorden and Billefjorden troughs (Dallmann, 1999; Ahlborn & Stemmerik, 2015), where Brøggertinden and Scheteligfjellet equivalents are absent and the Wordiekammen Formation rests unconformably on basement rocks. This study investigated two members of the Wordiekammen Formation at the Nordfjorden section. The lower part of the section, the Kapitol Member, is mainly composed of limestone and subordinate dolomite with a few beds containing calcified root remains (Figure 3.5B). The Kapitol Member was deposited in a shallow, open marine, and high-energy platform (Dons, 1983), and the previously examined fusulinid assemblages range in age from the Moscovian to middle Gzhelian (Figure 3.3; Nilsson & Davydov, 1997). The overlying the Kapitol Member is called the Tyrrellfjellet Member, and its biostratigraphy and lithology are broadly consistent with those at the Brøggerhalvøya section (Dallmann, 1999).

3.2.3 Age model

  To place our sulfur isotope data into a global context, the correct age needs to be estimated for each of the analyzed samples. A relatively robust chronostratigraphic framework has been developed for the late Paleozoic succession of Spitsbergen by analyzing various fossil groups, including foraminifera, conodont, polymorph, and bryozoan (Cutbill & Challinor, 1965; Sosipatrova, 1967; Nakrem et al., 1992; Mangerud & Konieczny, 1993; Nilsson, 1994; Nilsson & Davydov, 1997; Harland & Geddes, 1997; Buggisch et al., 2001; Lee, 2013), and a few fusulinids specimens was identified to genus level in thin sections of the Mørebreen Member are consistent with those previously described (Cutbill & Challinor, 1965; Figure 3.2). The absolute age of each lithostratigraphic boundary was calibrated primarily based on the comparison between the published foraminiferal assemblage data (Cutbill & Challinor, 1965;

70

Sosipatrova, 1967; Nilsson, 1994; Nilsson & Davydov, 1997) and the Geologic Time Scale 2020 (Gradstein et al., 2020; Figure 3.3), and sample ages were then assigned by linearly interpolating between lithostratigraphic boundary ages according to their relative positions within the section (Tables 3.1-3.2).

Established by foraminifera (Cutbill & Challinor, 1965) and conodont biostratigraphy (Buggisch et al., 2001), age of Scheteligfjellet Formation is early to middle Moscovian. Age of the overlying Mørebreen Member is the Myachovian substage to middle Gzhelian (Cutbill & Challinor, 1965; Harland & Geddes, 1997). The Tyrrellfjellet Member contains late Gzhelian to early Sakmarian fusulinids (Figure 3.3; Nilsson & Davydov, 1997).

Nilsson (1994) considered the base of the Gipshuken Formation to be younger than the *Eoparafusulina* fusulinid biozone, representing a late Sakmarian (Sterlitamakian) age, although other index fossils might indicate a slightly younger age (Harland & Geddes, 1997). The upper part of the Gipshuken Formation contains the foraminifera assemblage of an Artinskian age (Sosipatrova, 1967), but no *Parafusulina* Dunbar & Skinner, 1931 is known from this locality (Cutbill & Challinor, 1965). Thus, this study placed the upper boundary of this unit at the base of the *Parafusulina* biozone (Figure 3.3), which is about 2 Myr younger than the proposed age of the lower part of the Kapp Starostin Formation that unconformably overlies the Gipshuken Formation (Nakrem et al., 1992; Buggisch et al., 2001).

In the Nordfjorden section, Cutbill & Challinor (1965) recognized the early Moscovian *Profusulinella* biozone in the lowermost part of the Kapitol Member at the Nordfjorden Block. Therefore, the age of the Kapitol Member basement is correlated with the boundary of the Vereian to Kashirian in the Russian Platform substage (Harland & Geddes, 1997). Also, Nilsson & Davydov (1997) placed the Kapitol-Tyrrellfjellet boundary across the transition between the *J. jigulensis* and the *D. sokensis* biozones (Figure 3.3).
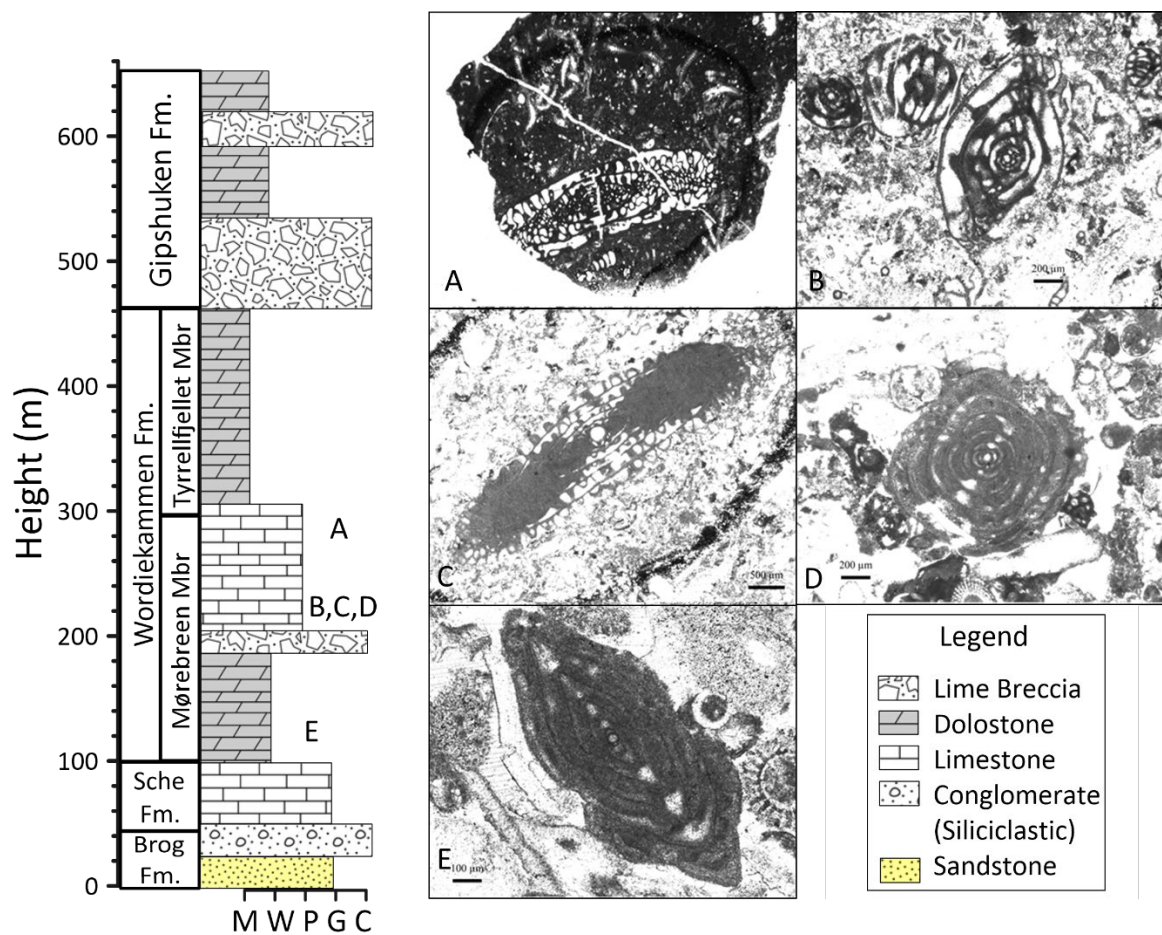
Figure 3.2. Occurrence of fusulinids in the Mørebreen Member. A-*Triticite* Rozovskaya, 1948; B-*Quasifusulina* Chen, 1934; C-*fusulinella* Lee, 1927; D-*pseudostafella* Thompson, 1947; E-*Ozawainella* Thompson, 1935; M, mudstone; W, wackestone; P, packstone; G, grainstone; C, conglomerate; Sche., Scheteligfjellet; Brog., Brøggertinden; Fm., Formation.; Mbr., Member.
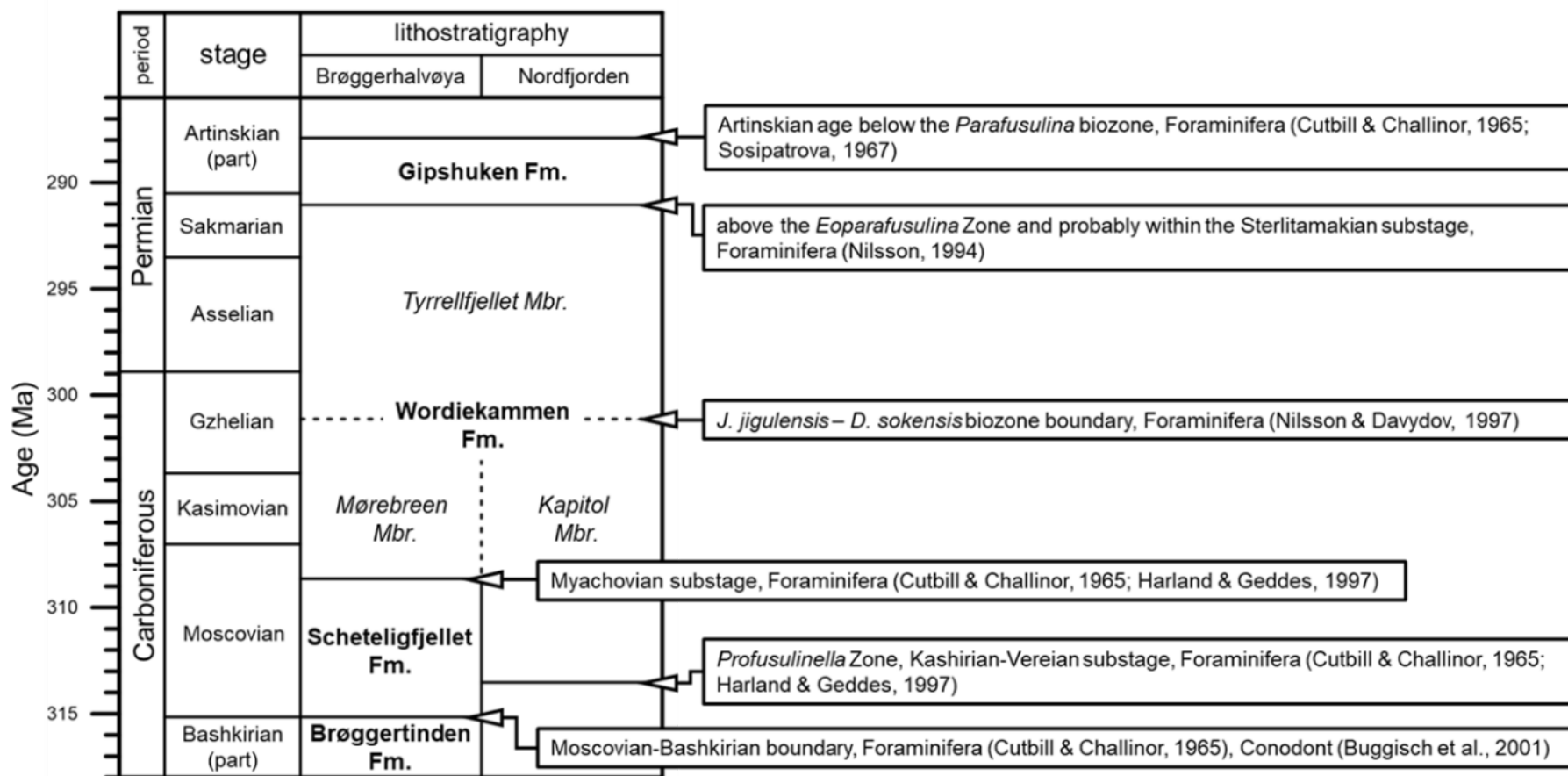
Figure 3.3. Lithostratigraphic boundary ages estimated based on the Geologic Time Scale 2020 (Gradstein et al., 2020) and published paleontological data.

73
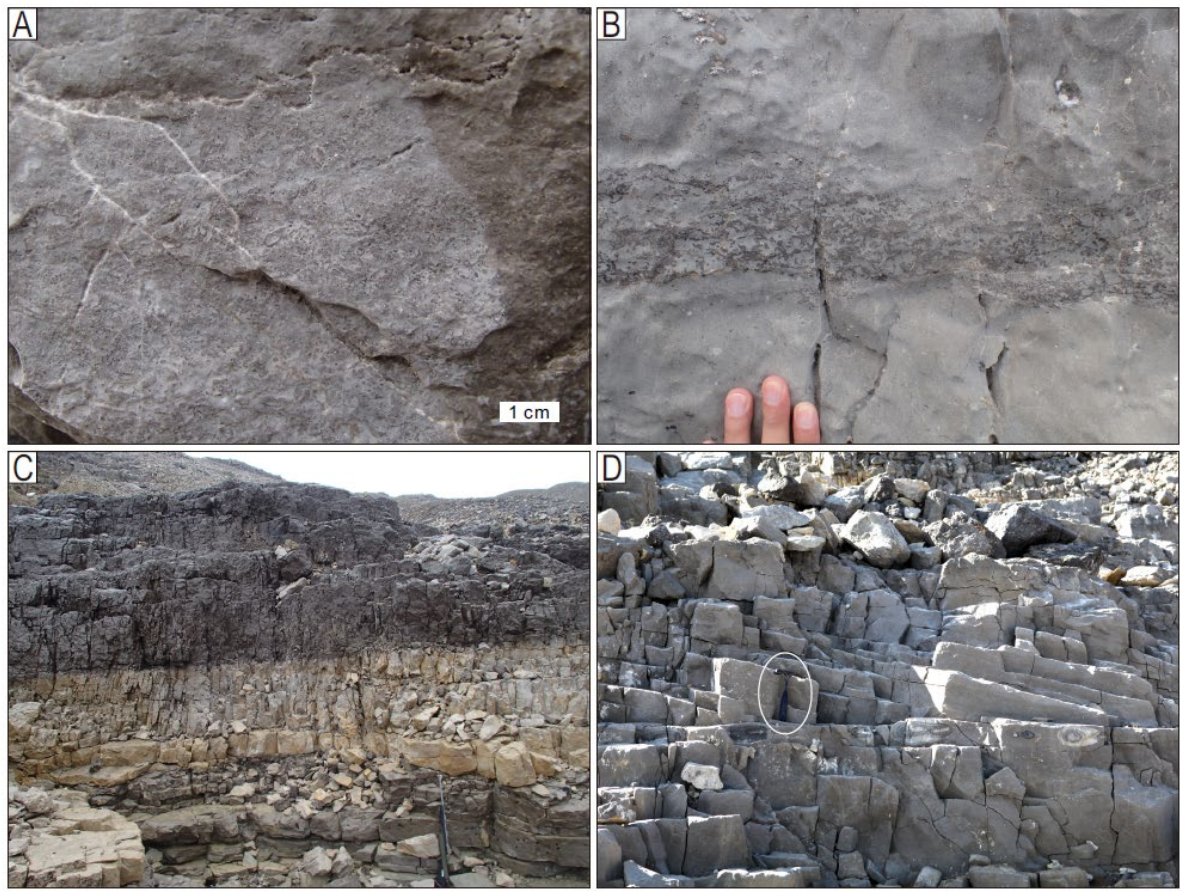
Figure 3.4. Selected facies of the Wordiekammen Formation in the Brøggerhalvøya section. (A) Skeletal pack-grainstone in the Mørebreen Member. (B) Lime mudstone with a horizon of calcified root remains (microcodium). (C) Dolo-mudstone (light gray) and lime mudstone (dark gray) in the upper part of the Mørebreen Member. Rifle is ca. 110 cm long. (D) Cross-stratified and massive grainstone occurring in association with dolo-mudstone and lime mudstone of the Mørebreen Member. Hammer for scale is 27 cm long. The stratigraphic position of each photograph is presented in Figure 3.5.

3.3 Methods

3.3.1 Sample preparation

  A total of 108 samples were collected from the outcrops of the Brøggerhalvøya section during a field campaign in July 2018. For the Nordfjorden section, 42 samples from the paleontological collection of the Natural History Museum, University of Oslo were used in this study, which are identified with PMO (Paleontological Museum Oslo) prefix. Rock samples were cut into cubes of 3 cm side length, crushed to smaller size by a jaw crusher, and grounded with an agate mortar. Throughout this process, any weathering rinds, sample markings, and veins were removed.

3.3.2 CAS extraction

  CAS was extracted using a method slightly modified after Wotte et al. (2012). First, water-soluble sulfate on powdered samples was eliminated to prevent possible contamination. The 100g of powdered sample was soaked in 500ml 10% NaCl solution for 5 hours and suspended matter was removed by decant. Samples were soaked 10% 500ml NaCl water again and agitate it 24 hours. The rinsed samples were filtered by CHMLAB® Ashless Qualitative filter paper and rinsed with 1L deionized water. The absence of sulfate in the solution was tested with a 20% $BaCl_2$ solution, and these leaching steps were repeated until no $BaSO_4$ was precipitated from the solution.

  Rinsed samples were dissolved by 400 ml of 6 N HCl for 2 hours to liberate sulfate from the carbonate matrix. The solution was filtered sequentially through paper and 0.45 μm cellulose nitrate membrane filters, and the insoluble residue was reserved for pyrite extraction. 25 ml of 20% $BaCl_2$ solution was added to the filtrate for the precipitation of sulfate ions as $BaSO_4$, which was then rinsed, filtered via a membrane filter of 0.45 μm, and dried overnight at 60 °C.

3.3.3 Pyrite extraction

Pyrite sulfur was extracted from the dried insoluble residue according to a procedure modified after Canfield et al. (1986). Pyrite extraction experiment required three solutions including chromium solution to release the pyrite, zinc acetate to trap the sulfide as a form of ZnS, and silver nitrate to covert ZnS to Ag_2S. Chromium reduction solution was made by reduce the $CrCl_3$ solution (266.45g $CrCl_3$, 1 L of DW and 41.25 ml of 12 N hydrochloric acid) to zinc shot. Zinc acetate solution was made by 1L of DW, 40 g of zinc acetate dihydrate and 30 ml acetic acid. Silver nitrate solution was made by 17 g of silver nitrate powder and 1L of DW.

100 ml of Zn acetate solution was filled in the bottle for H_2S trap. Nitrogen gas was circulated in the in the extraction line and the chromium reduction solution was put into bowl flask by a syringe. Samples were heated up to 130°C for 2 hours. H_2S reduced by the chromium solution was collected into Zn trap as a form of zinc sulfide. The aggregated ZnS was precipitated as silver sulfide by dropping 5 ml of $AgNO_3$ solution. Ag_2S was harvested by either filtration or centrifugation. Precipitated samples and solutions were centrifuged for 10 minutes at 2000 rpm to settling the silver sulfide. The supernatant liquid was decanted and diluted with deionized water. This process was repeated three times and samples were dried at 60 °C for one day. Dried samples were weighed and placed in a vial.

3.3.4 Isotope analysis

Sulfur isotope analysis of the obtained $BaSO_4$ and Ag_2S was conducted using a Thermo Delta V continuous flow isotope ratio mass spectrometer (IRMS) at the Department of Earth and Planetary Sciences, Northwestern University, Evanston, USA. Sulfur isotope ratios are reported as $\delta^{34}S$ relative to the Vienna Canyon Diablo Troilite (VCDT). When the entire extraction process was replicated, the $\delta^{34}S$ reproducibility was ±0.2‰ and ±0.8‰ for CAS and pyrite, respectively.

For the measurement of carbon and oxygen isotope ratios, carbonate samples (~0.5 mg) were reacted with 100% H_3PO_4, and the released carbon dioxide was analyzed by a Thermo Delta V IRMS coupled to a Gas Bench device at the Department of Earth and Planetary Sciences, Northwestern University. Carbon and oxygen isotope ratios are reported as standard delta notation relative to the Vienna Pee Dee Belemnite (VPDB), and the analytical precision was ±0.1‰ and ±0.2‰, respectively.

3.3.5 Box model

To quantitatively assess the possible cause of the observed changes in sulfur isotope values during the Early Permian, this study constructs a box model of the global sulfur cycle. Our model consists of one reservoir with a single riverine input and two outputs related to pyrite and evaporite burial. This study first describes the sulfur cycle model and then show detailed results of model runs. The model parameters are listed in Table 3.3.

The basic framework of the sulfur cycle model is as follows (Kurtz et al., 2003):

$$d/dt \, M_s = F_w - (F_{py} + F_{evap}) \quad (1)$$

$$d/dt \, \delta^{34}S_{SO4} = (F_w(\delta^{34}S_{in} - \delta^{34}S_{SO4}) - F_{py}\varepsilon_{avg}) / M_s \quad (2)$$

where M_s is the mass of sulfate in the ocean reservoir, F_w is the weathering flux from the river to the ocean, F_{py} is the pyrite burial flux, F_{evap} is the evaporate burial flux, $\delta^{34}S_{SO4}$ is the isotope composition of seawater sulfate, $\delta^{34}S_{in}$ is the sulfur isotope composition of riverine input, and ε_{avg} is the average isotope fractionation associated with pyrite burial.

Applying the parameters shown in Table 3.3 to the model, f_{py} (the ratio of the buried pyrite to riverine sulfate) of 0.24 and the pyrite burial flux of 3.65×10^{11} mol/yr are calculated for the initial steady state. The initial evaporite burial flux of 11.35×10^{11} mol/yr, which is estimated as the difference between riverine input and pyrite burial fluxes, remains constant throughout the model experiments.

With the initial steady state, this study perform model runs to reconstruct the $\delta^{34}S_{SO4}$ increase by applying forcings - changing relevant parameters. The model calculates the $\delta^{34}S_{SO4}$ and seawater sulfate concentration at the end of each 50,000-year period, and the modeled duration is 11 Myr (299–288 Ma).

The size of sulfate reservoir is an important factor in reproducing the sulfate isotope trend. The larger the sulfate reservoir is, the greater perturbation in the sulfur cycle required to reproduce the data. In our model experiments, three different initial sulfate reservoir sizes were examined, 4.5 mM (-1σ), 9 mM (mean), and 18 mM (+1σ), adopted from the estimates of the global sulfate reservoir size in the Early Permian (Algeo et al., 2015).

3.4 Results

3.4.1 Brøggerhalvøya section

The results of geochemical analyses of the Brøggerhalvøya section are presented in Figures 3.5-3.6A and Table 2.1. In the Brøggerhalvøya section, CAS and pyrite contents range up to 2330 ppm and 1159 ppm, respectively. The average CAS content is 461 ppm, and that of pyrite is 83 ppm. The sulfur isotope compositions of CAS range from 12.6 to 40.1‰. From the basal Scheteligfjellet Formation through the lower part of the Mørebreen Member, $\delta^{34}S_{CAS}$ values become progressively lighter from 18 to 14‰, which is followed by a rapid increase in the uppermost part of the Mørebreen Member. Moving upward stratigraphically, $\delta^{34}S_{CAS}$ values remain stable at approximately 15‰ in the middle Tyrrellfjellet Member. From the upper Tyrrellfjellet Member to the Gipshuken Formation, $\delta^{34}S_{CAS}$ values show a steady increasing trend superimposed by brief negative and positive excursions (Figure 3.5). In the Brøggerhalvøya section, pyrite sulfur isotope ratios ($\delta^{34}S_{py}$) vary over a wide range between -30 and 22‰. From the Scheteligfjellet Formation to the lower Mørebreen Member, the majority of $\delta^{34}S_{py}$ values are scattered from -10 to 10‰ and show a modest increase in the upper part of the Mørebreen Member, where sulfate is anomalously enriched in ^{34}S. Sulfur isotope compositions of pyrite decrease

78

upward across the boundary between the Mørebreen and Tyrrellfjellet members and remain relatively low with increased variability throughout the Gipshuken Formation (Figure 3.5). The carbon isotope compositions of carbonate ($\delta^{13}C_{carb}$) range from -1.4 to 5.6‰ with an average of 3.4‰. In the lowermost part of the Scheteligfjellet Formation, carbon isotope values are lower than 0‰ and increase to 2-4‰ in the Mørebreen Member. $\delta^{13}C_{carb}$ values increase further to 6‰ in the Tyrrellfjellet Member, followed by a decrease to 2-4‰ in the Gipshuken Formation. The uppermost part of the Gipshuken Formation shows carbon isotope values of 0-2‰. The oxygen isotope compositions of carbonate ($\delta^{18}O_{carb}$) ranges from -17 to -1.8‰ with an average of -6.7‰ (Figure 3.6). In the Scheteligfjellet and Wordiekammen formations, $\delta^{18}O_{carb}$ scatters from -12 to -4‰, but a few more negative values are observed in the Gipshuken Formation.

3.4.2 Nordfjorden section

Geochemical data of the Nordfjorden section are presented in Figures 3.5-3.6B and Table 3.2. In the Nordfjorden section, CAS contents range from 39 to 6241 ppm with an average of 1011 ppm, while the range of pyrite contents is from 6 to 976 ppm with an average of 189 ppm. The sulfur isotope ratios of CAS and pyrite generally decrease upsection through the Kapitol and Tyrrellfjellet members, from 15 to 12‰ and -10 to -30‰, respectively (Figure 3.5B). However, the Kapitol Member does not show the $\delta^{34}S_{CAS}$ increase observed in the upper Mørebreen Member, although the Kapitol Member is considered stratigraphic equivalent to the Mørebreen Member of the Brøggerhalvøya section. The $\delta^{13}C_{carb}$ values vary from -0.5 to 4.8‰, and the average is 2.8‰ in the Nordfjorden section. As in the Brøggerhalvøya section, $\delta^{13}C_{carb}$ shows light compositions from 0 to 2‰ in the lower part of the Kapitol Member and increases to 2-4‰ from the middle Kapitol to the Tyrrellfjellet members. Overall, the carbon isotope compositions in the Nordfjorden section are relatively lighter than those in the Brøggerhalvøya section. The oxygen isotope compositions of carbonate range from -10.7 to -0.7‰, with an average of -4.7‰ in the Nordfjorden section (Figure 3.6B).

3.5 Discussions

3.5.1 Screening of geochemical data

Because $\delta^{34}S_{CAS}$ values can be influenced by diagenesis and the incorporation of contaminant sulfate, previous studies have used cross-plots of geochemical data to confirm that CAS isotope data preserve the signal of the overlying water column (Given & Lohmann, 1986; Marenco et al., 2008). Depletion of $\delta^{18}O_{carb}$ and/or the covariance between carbon and oxygen isotope ratios indicate extensive meteoric or deep-burial diagenesis (Given & Lohmann, 1986; Darry, 2010) or methane-derived authigenic carbonate formation (Cui et al., 2017), potentially influencing the $\delta^{34}S_{CAS}$ values. However, cross-plots of $\delta^{13}C_{carb}$, CAS content, and $\delta^{34}S_{CAS}$ versus $\delta^{18}O_{carb}$ show little correlation although some samples have a $\delta^{18}O_{carb}$ below -10‰ (Figures 3.7A-C). Pyrite oxidation either during diagenesis or sample preparation could also contaminate the recovered CAS, lowering the $\delta^{34}S_{CAS}$ values (Marenco et al., 2008), but again, neither CAS contents nor $\delta^{34}S_{CAS}$ values show a significant correlation with pyrite contents (Figures 3.7D-E). Finally, while a positive correlation between $\delta^{34}S_{CAS}$ and 1/CAS could imply the mixing of carbonate minerals with different origins (Present et al., 2015; Richardson et al., 2019a; Ma et al., 2021), the cross-plot of our data does not show such a trend (Figure 3.7F). Overall, alteration of $\delta^{34}S_{CAS}$ during diagenesis or sample preparation is not apparent from simple correlation analysis of geochemical data. Following sections further evaluate the preservation of global seawater signatures in the context of the sedimentology of the Gipsdalen Group, i.e. the changes in relative sea-level and depositional environment.
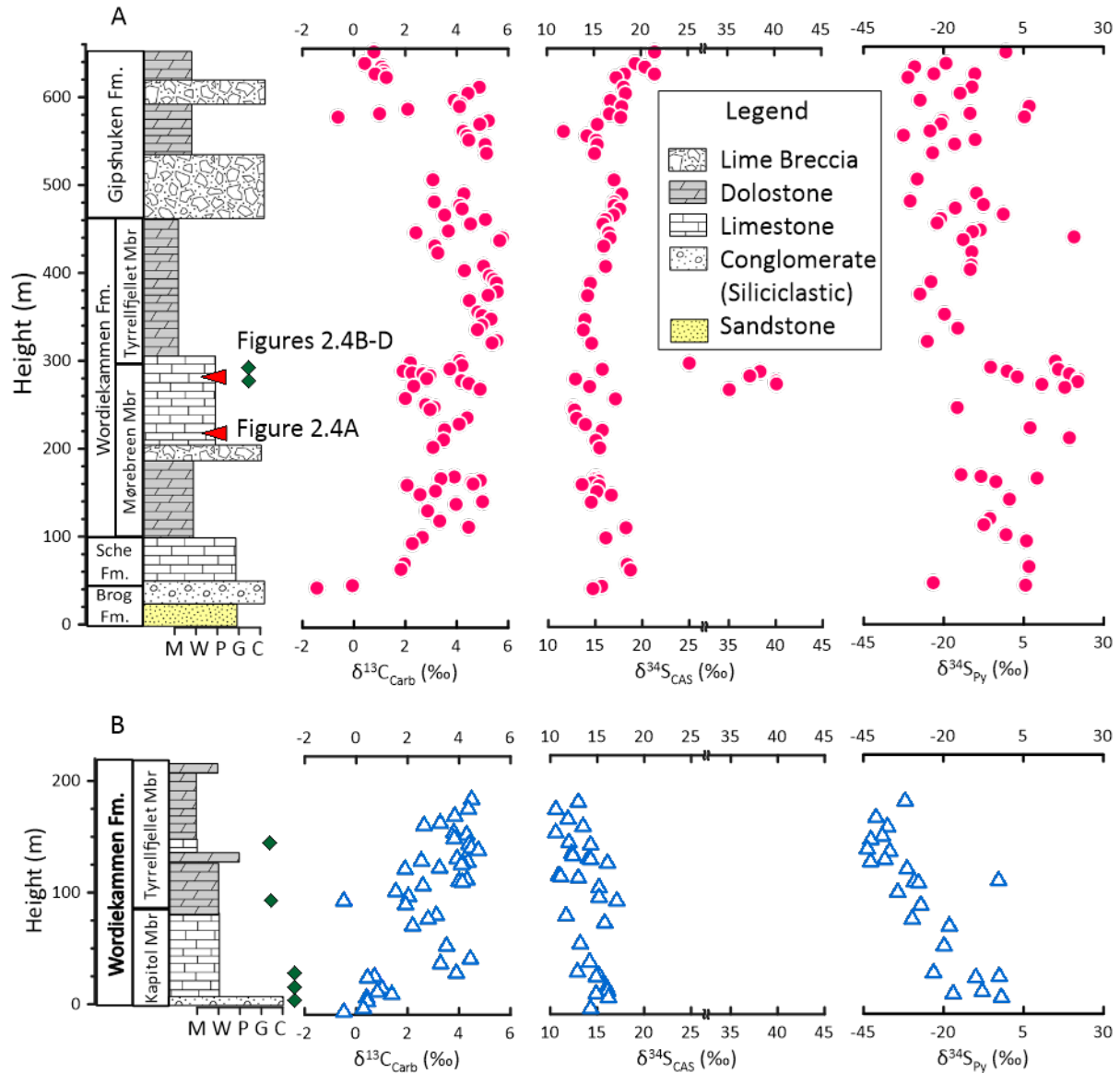
Figure 3.5. Isotopic compositions of carbonate carbon, CAS, and pyrite sulfur from the Brøggerhalvøya (A; red circle) and Nordfjorden (B; blue triangle) sections, plotted along the lithologic column. M, mudstone; W, wackestone; P, packstone; G, grainstone; C, conglomerate. Sche., Scheteligfjellet; Brog., Brøggertinden; Fm., Formation. Mbr., Member. The green diamonds indicate the locations of microcodium occurrences. The red wedges show the location of the outcrop photos in Figure 3.4.
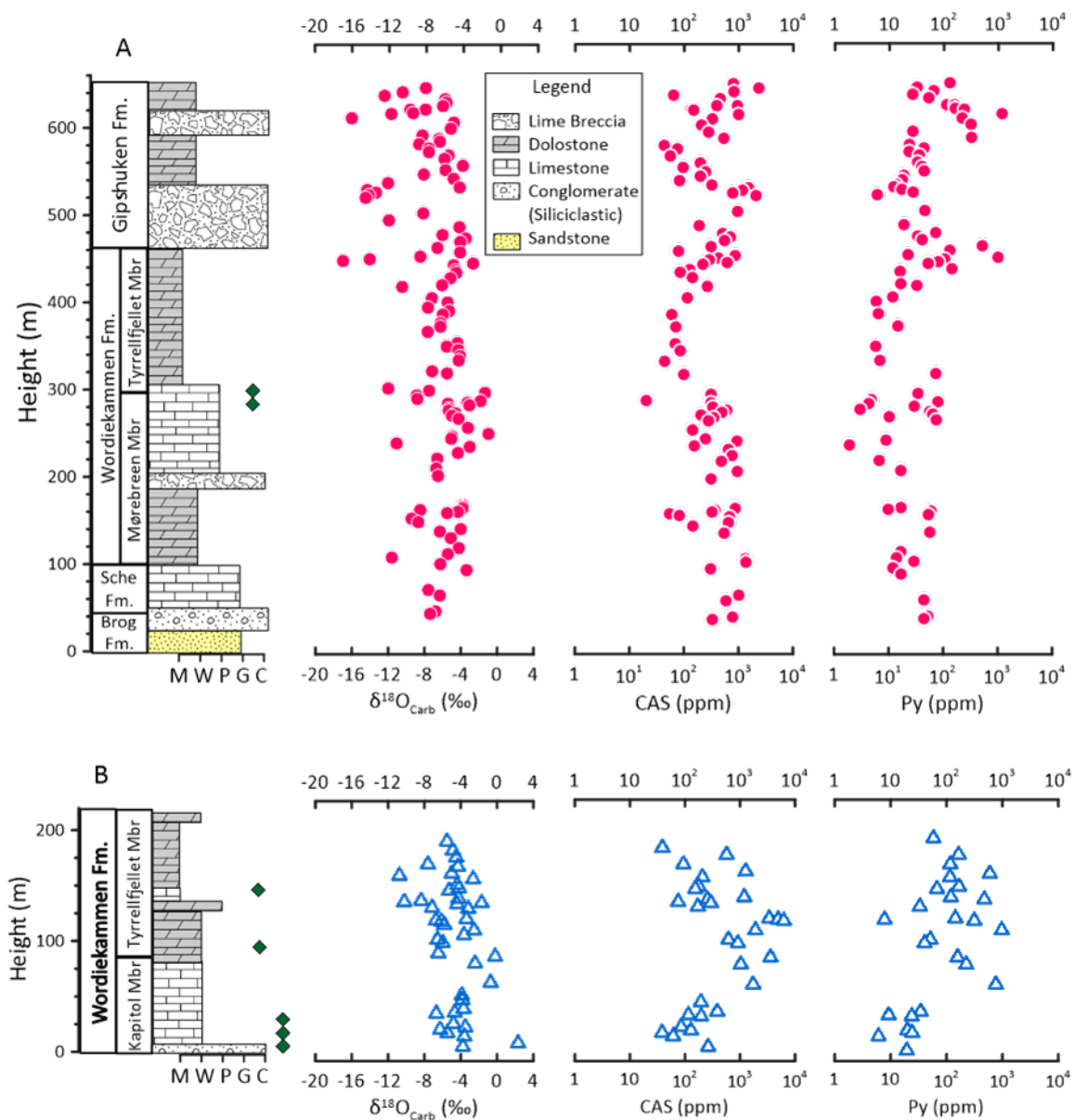
Figure 3.6. Oxygen isotope values and contents of CAS and pyrite in the Brøggerhalvøya (A; red circle) and Nordfjorden (B; blue triangle) sections. Green diamonds indicate the locations of microcodium. The difference between duplicate of the CAS and pyrite contents does not exceed 25% and 20%, respectively.
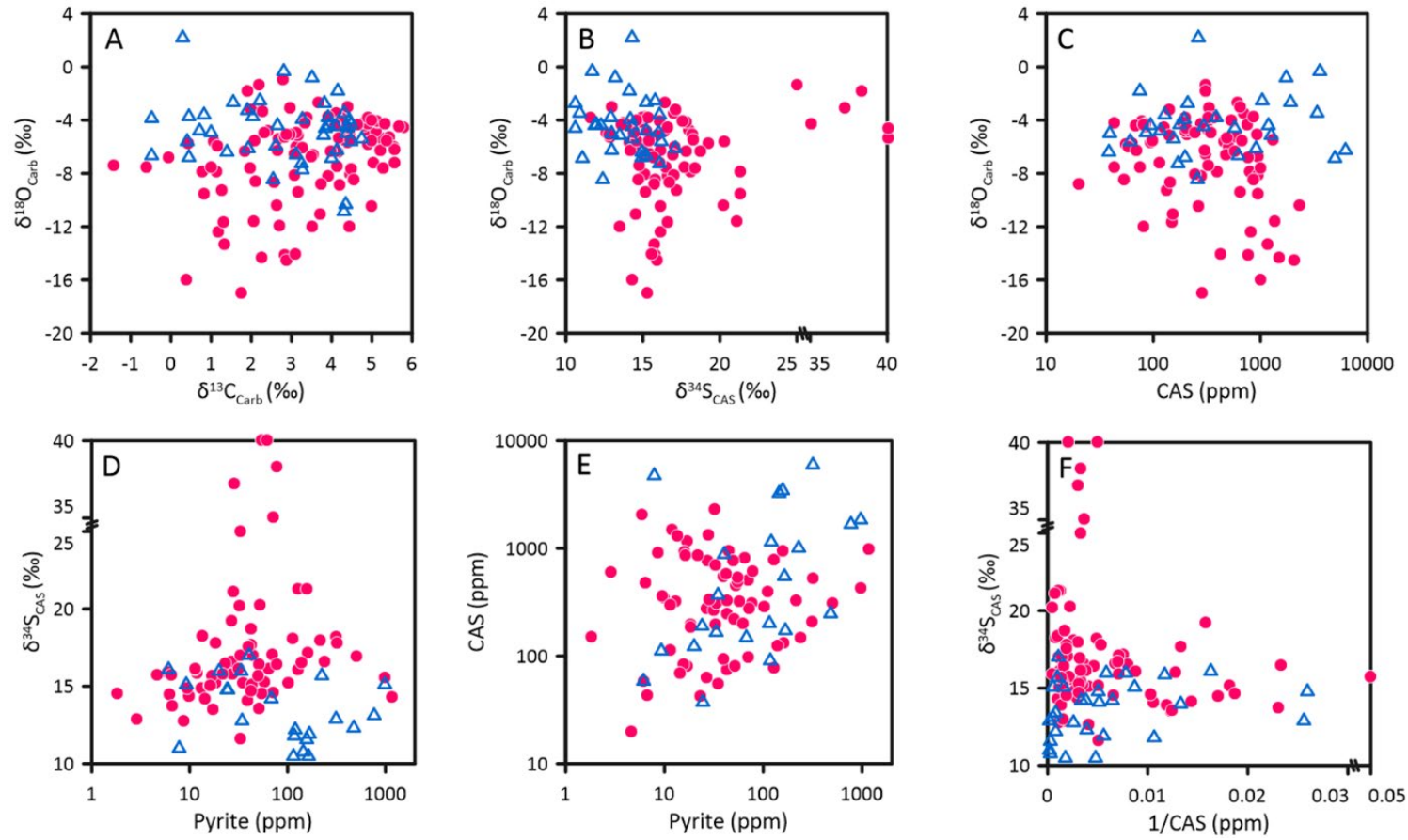
Figure 3.7. Cross plots of (A) $\delta^{13}C_{Carb}$ vs $\delta^{18}O_{carb}$, (B) $\delta^{34}S_{CAS}$ vs $\delta^{18}O_{carb}$, (C) CAS vs $\delta^{18}O_{carb}$, (D) pyrite content vs $\delta^{34}S_{CAS}$, (E) Pyrite content vs CAS content (F) reciprocal CAS content vs $\delta^{34}S_{CAS}$ to evaluate the potential diagenetic alteration and post-depositional contamination of $\delta^{34}S_{CAS}$ values. The red circles show data of the Brøggerhalvøya section, and the blue triangles indicate the Nordfjorden section data.
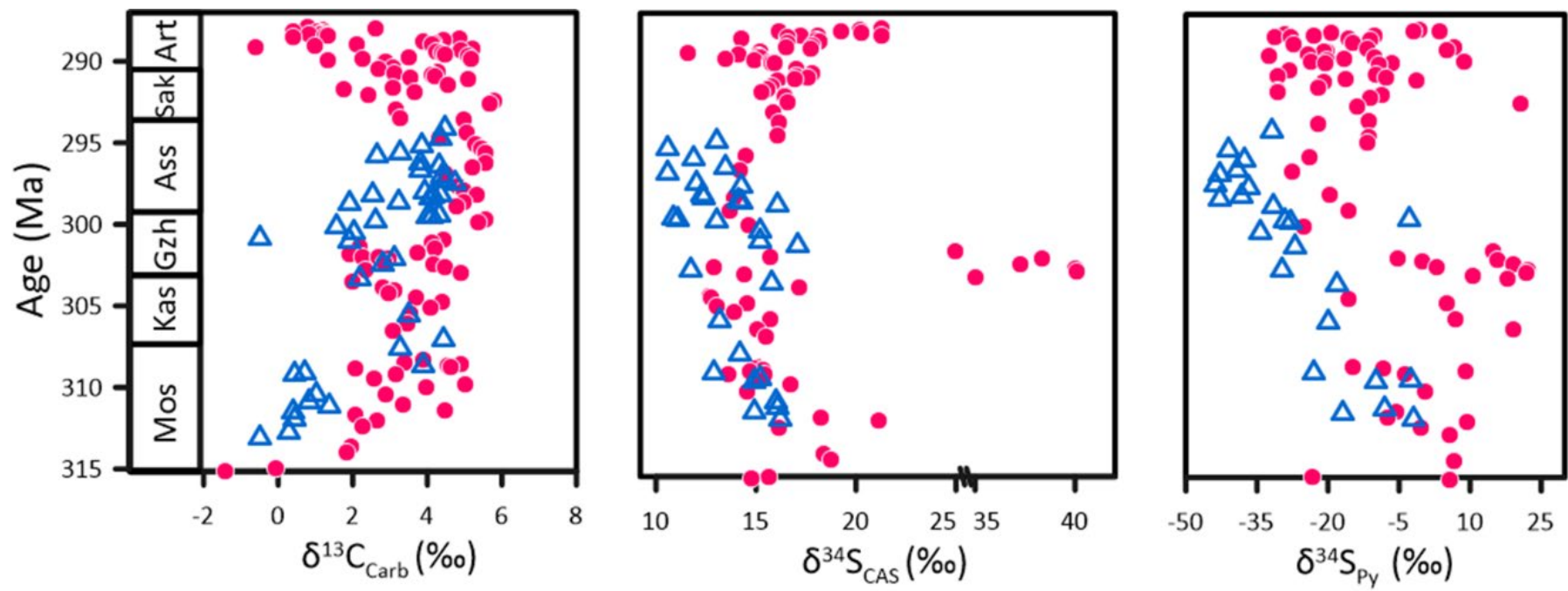
Figure 3.8. Composite carbon and sulfur isotope records from the Brøggerhalvøya (red circle) and Nordfjorden (blue triangle) sections.

Table 3.1. Geochemical and isotopic data from the Brøggerhalvøya section

Sample	Height (m)	Calibrated age (Ma)	$\delta^{13}C$ (‰)	$\delta^{18}O$ (‰)	CAS (ppm)	$\delta^{34}S_{CAS}$ (‰)	Pyrite (ppm)	$\delta^{34}S_{Py}$ (‰)	$\Delta^{34}S$ (‰)
R1-5	650	287.90	0.8	-7.8	793	21.3	128	-0.6	21.9
R1-4	645	287.98	2.6	-10.4	2330	20.2	32	3.5	16.7
R1-3	641	288.05	1.2	-12.4	814	16.2	65	-2	18.2
R1-2	637	288.12	0.4	-5.7	63	19.2	27	-19.3	38.5
R1-1	633	288.19	1.1	-5.6	455	20.3	52	-29.1	49.4
R2-6	629	288.25	1.2	-6.0					
R2-5	625	288.32	1.1	-7.9	394	18.1	112	-23.1	41.2
R2-3	625	288.32	0.8	-9.6	943	21.3	157	-10.3	31.6
R2-4	621	288.39	1.3	-9.2	133	17.2	160	-31.2	48.4
R2-2	620	288.41	1.3	-11.6	149	16.6	236	-27.9	44.5
R2-1	615	288.49	0.4	-16.0	991	14.3	1159	-15.8	30.1
R3-8	610	288.57	4.9	-4.8	327	18	215	-11.2	29.2
R3-7	603	288.69	4.4	-5.1	207	18.2	312	-14.9	33.1
R3-6	595	288.83	3.9	-8.2	279	16.6	27	-27.4	44
R3-5	591	288.89	4.2	-6.4					
R3-4	588	288.94	4.1	-6.3	530	17.8	319	6.7	11.1
R3-3	585	288.99	2.1	-8.6					
R3-2	580	289.08	1.0	-7.5	43	16.5	23	-11.8	28.3
R3-1	576	289.15	-0.6	-7.5	75	17.7	43	5.2	12.5
R4-5	572	289.21	5.2	-5.3			23	-20.4	
R4-4	568	289.28	4.9	-5.8	55	15.2	35	-20.9	36.1

Sample	Height (m)	Calibrated age (Ma)	$\delta^{13}C$ (‰)	$\delta^{18}O$ (‰)	CAS (ppm)	$\delta^{34}S_{CAS}$ (‰)	Pyrite (ppm)	$\delta^{34}S_{Py}$ (‰)	$\Delta^{34}S$ (‰)
R4-2	555	289.50	4.4	-5.7	95	14.1	39	-32.6	46.7
R4-1	550	289.58	4.5	-8.1	245	15.1	43	-10.2	25.3
R5-1	545	289.67	5.1	-4.8	197	15.2	18	-16.6	31.8
R5-2	540	289.75	3.5	-12.0	81	13.5	17	-20.1	33.6
BBS-16	535	289.84	5.2	-4.1	320	14.9	13	-23.5	38.4
BBS-15	532	289.89	2.2	-14.3	1490	15.9	12	8.6	7.3
BBS-14	529	289.94	1.3	-13.3	1161	15.7	17	-6.4	22.1
BBS-13	526	289.99	2.8	-14.1	771	15.8	27	-20.6	36.4
BBS-12	523	290.04	2.9	-14.5	2073	15.9	6	-9.4	25.3
BBS-11	505	290.34	3.1	-8.1	949	17.0	44	-28.3	45.3
BBS-10	497	290.48	2.7	-11.9					
BBS-09	489	290.61	4.3	-4.1	188	17.8	18	-9.8	27.6
BBS-08	480	290.76	3.1	-6.0	504	17.0	70	-30.5	47.5
BBS-07	476	290.83	4.1	-3.4	697	17.0	33	-7.6	24.6
BBS-06	472	290.90	4.2	-4.1	545	17.6	40	-16.4	34.0
BBS-05	465	291.02	3.5	-6.6	309	16.9	502	-1.4	18.3
BBS-04	460	291.10	5.1	-4.1	78	16.1	127	-21	37.1
SFL-149	455	291.41	4.5	-8.4	857	15.8	22	-22.1	37.9
BBS-03	452	291.60	3.1	-14.0	426	15.6	976	-30.5	46.1
BBS-02	450	291.73	1.7	-17.0	287	15.3	102	-30.5	45.8

Sample	Height (m)	Calibrated age (Ma)	$\delta^{13}C$ (‰)	$\delta^{18}O$ (‰)	CAS (ppm)	$\delta^{34}S_{CAS}$ (‰)	Pyrite (ppm)	$\delta^{34}S_{Py}$ (‰)	$\Delta^{34}S$ (‰)
SFL-143	445	292.04	2.4	-4.8	219	16.4	51	-11.0	27.5
SFL-141	439	292.41	5.8	-4.6	126	16.6	139	20.7	-4.1
SFL-139	436	292.60	5.7	-4.5	84		16	-14.0	
SFL-136	430	292.98	3.1	-5.2	141	15.9			
SFL-133	422	293.48	3.3	-6.1			16	-11.3	
SFL-132	420	293.60	5.0	-10.4	265	16.2	32	-22.2	38.4
SFL-124	407	294.41	5.0	-7.2	114	16.1	11	-11.4	27.5
SFL-122	402	294.73	4.3	-5.5			6	-11.7	
SFL-119	396	295.10	5.3	-7.6					
SFL-116	392	295.35	5.4	-5.3					
SFL-114	388	295.60	5.5	-6.0	59	14.5	6	-24.0	38.5
SFL-113	378	296.23	5.6	-6.2					
SFL-111	374	296.48	5.2	-6.2	70	14.2	14	-27.5	41.6
SFL-110	368	296.85	4.5	-7.6					
SFL-108d5	355	297.66	4.8	-4.4	68				
SFL-106d5	351	297.91	5.0	-5.5			6	-19.8	
SFL-104	347	298.16	5.3	-4.3	84	13.9			
SFL-102	340	298.60	5.0	-4.1					
SFL-101	335	298.91	4.8	-4.2	43	13.7	7	-15.6	29.3
SYB77	322.5	299.69	5.6	-7.2					
SFL80	320	299.85	5.4	-5.5	97	14.6	70	-25.2	39.8
SYB62	302.5	300.94	4.4	-12.0					

Sample	Height (m)	Calibrated age (Ma)	$\delta^{13}C$ (‰)	$\delta^{18}O$ (‰)	CAS (ppm)	$\delta^{34}S_{CAS}$ (‰)	Pyrite (ppm)	$\delta^{34}S_{Py}$ (‰)	$\Delta^{34}S$ (‰)
SFL71	297.5	301.34	2.2	-1.3	309	25.1	33	14.9	10.2
SYB56	294.5	301.51	4.2	-8.9					
SYB51	290.5	301.72	3.7	-8.8	20	15.7	5	-5.4	21.1
SFL66	288	301.86	1.9	-1.8	309	38.3	77	15.8	22.5
SFL65	286	301.96	2.3	-3.3			4	-0.2	
SYB49	285	302.02	2.7	-5.4					
SFL64	283	302.13	3.0	-3.1	333	37.2	28	19.3	18.0
SYB47	279.5	302.32	2.8	-5.3	597	12.9	3	3.0	9.9
SYB44	277	302.45	4.2	-5.3	488	40.0	54	22.2	17.9
SYB42	274	302.61	4.5	-4.6	202	40.1	62	21.8	18.3
SYB40	271	302.78	2.3	-5.0	345	14.4	10	10.6	3.8
SYB36	267.5	302.96	4.9	-4.2	277	35.0	72	17.8	17.2
SYB27	257	303.53	2.0	-3.2	141	17.1			
SFL49	250	303.91	2.8	-1.0					
SFL47.5	247	304.07	3.1	-5.0	244	12.6			
SYB19	244.5	304.21	3.0	-5.1	923	12.8	9	-15.8	28.6
SYB15	239	304.50	3.7	-11.1	152	14.5	2	5.2	9.4
SFL48.5	235	304.72	4.4	-3.0	645	13.0			
SYB11	228	305.10	4.1	-4.3	751	13.9			
SYB10	221.5	305.45	3.5	-6.6	477	15.7	6	7.0	8.8
SYB5	210	306.07	3.5	-6.7	937	15.1	16	19.3	-4.2

Sample	Height (m)	Calibrated age (Ma)	$\delta^{13}C$ (‰)	$\delta^{18}O$ (‰)	CAS (ppm)	$\delta^{34}S_{CAS}$ (‰)	Pyrite (ppm)	$\delta^{34}S_{Py}$ (‰)	$\Delta^{34}S$ (‰)
SYA38	168	308.34	3.9	-3.8	857	15.1	16	-14.6	29.7
SFL30	166	308.45	3.4	-3.8	365	14.9	9	-8.4	23.3
SFL28	164	308.56	4.9	-3.8	322	15.3	58	9.2	6.2
SFL27	162	308.67	4.6	-8.5	53	14.7			
SFL26	160	308.77	4.6	-4.3	81	13.6	51	-3.7	17.3
SYA28	158.5	308.85	2.1	-5.5	675	15.4			
SYA19	152	309.21	3.2	-9.4	643	15.2			
SYA18	148	309.42	2.6	-8.7	143	16.7			
SFL6	140	309.85	5.0	-4.0	536	14.6	55	0.5	14.1
SYA15	137	310.02	4.0	-6.3					
SYA12	129.5	310.42	2.9	-5.1					
SYA6	118	311.04	3.3	-4.2			16	-5.6	
SFL4	111	311.42	4.5	-5.4	1315	18.3	13	-7.5	25.7
SYC49	107	311.64	2.1	-11.6	1346	21.1	28	9.3	11.8
SYC41	99.5	312.04	2.7	-6.3	302	16.1	11	-0.6	16.7
SYC37	92.5	312.42	2.3	-3.4			16	5.8	
SYC34	69.6	313.66	2.0	-7.6	997	18.4			
SYC25	63.2	314.00	1.8	-6.3	579	18.7	42	6.6	12.1
SYC7	44.8	315.00	-0.1	-6.8	767	15.7	50	-23.3	39.0
SYC1	42	315.15	-1.4	-7.4	326	14.7	42	5.6	9.2

Table 3.2. Geochemical and isotopic data from the Nordfjorden section.

Sample	Height (m)	Calibrated Age(Ma)	$\delta^{13}C$ (‰)	$\delta^{18}O$ (‰)	CAS (ppm)	$\delta^{34}S_{CAS}$ (‰)	Pyrite (ppm)	$\delta^{34}S_{Py}$ (‰)	$\Delta^{34}S$ (‰)
PMO 222.209	184	293.91	4.5	-5.5			59	-32.0	
PMO 222.208	176	294.54	4.4	-4.9	39	13.0			
PMO 222.207	170	295.01	3.8	-4.5	570	10.6	165	-41.1	51.7
PMO 222.206	164	295.48	3.3	-7.6					
PMO 222.205	162	295.63	2.6	-4.3	94	11.9	117	-37.5	
PMO 222.204	156	296.10	3.8	-5.0	1264	13.5			
PMO 222.203	154	296.26	4.3	-10.7			595	-39.1	
PMO 222.202	151	296.49	3.8	-2.6	208	10.6	116	-42.7	53.3
PMO 222.201	146	296.88	4.4	-4.4					
PMO 222.200	143	297.12	4.5	-4.2	178	12.0	168	-43.8	55.8
PMO 222.199	141	297.27	4.8	-5.3	154	14.3	68	-36.8	51.1
PMO 222.198	134	297.82	3.9	-4.2	1195	12.3	120	-38.3	50.6
PMO 222.197	132	297.98	2.5	-8.3	257	12.4	476	-42.8	
PMO 222.196	131	298.05	4.4	-10.2					
PMO 222.195	130	298.13	4.1	-1.7	75	14.1			
PMO 222.194	129	298.21	4.1	-4.4	297	14.3			
PMO 222.193	126	298.44							
PMO 222.192	125	298.52	3.2	-7.1	171	16.1	33	-31.4	47.5
PMO 222.191	116	299.23	1.9	-3.2					
PMO 222.190	115	299.30	4.3	-3.4	3411	10.9	144	-2.8	13.7
PMO 222.189	114	299.38	4.0	-6.7	4919	11.1	8	-29.1	

Sample	Height (m)	Calibrated Age(Ma)	$\delta^{13}C$ (‰)	$\delta^{18}O$ (‰)	CAS (ppm)	$\delta^{34}S_{CAS}$ (‰)	Pyrite (ppm)	$\delta^{34}S_{Py}$ (‰)	$\Delta^{34}S$ (‰)
PMO 222.188	111	299.62	4.1	-6.1	6241	13.0	315	-27.8	40.8
PMO 222.187	106	300.01	2.6	-5.8					
PMO 222.186	102	300.32	1.5	-2.5	1908	15.2	976	-34.3	49.5
PMO 222.185	98	300.63	2.0	-3.6					
PMO 222.184	95	300.87	-0.5	-6.5	616	15.2			
PMO 222.183	92	301.10	1.9	-6.0	916	17.1	41	-27.1	44.2
PMO 222.182	86	301.91	3.1	-6.5					
PMO 222.181	83	302.31	2.8	-0.2	3583	11.7	158	-29.8	41.5
PMO 222.180	77	303.12	2.2	-2.4	1035	15.8	226	-18.2	34.0
PMO 222.179	60	305.41	3.5	-0.7	1729	13.2	766	-19.8	33.0
PMO 222.178	49	306.90	4.4	-3.9					
PMO 222.177	45	307.43	3.3	-3.8	195	14.2			14.2
PMO 222.176	37	308.51	3.9	-3.7	386	12.9	35	-23.1	36.0
PMO 222.175	34	308.92	0.7	-4.7	116	15.2	9	-2.6	17.8
PMO 222.174	33	309.05	0.4	-6.7	197	14.9	24	-9.9	24.8
PMO 222.173	24	310.27	1.0	-4.8	86	16.0			
PMO 222.172	21	310.67	0.8	-3.5	129	16.1	20	-7.9	24.0
PMO 222.171	19	310.94	1.4	-6.3	39	14.9	24	-17.0	31.9
PMO 222.170	16	311.34	0.4	-5.5	61	16.2	6	-1.9	18.1
PMO 222.169	13	311.75	0.4	-3.6					
PMO 222.168	7	312.56	0.3	2.3	264	14.3			14.3
PMO 222.167	4	312.96	-0.5	-3.8					
Base	0	310.30							

Table 3.3. Parameters used in the steady state box model.

Parameter	Value	References
Volume of ocean	1.5×10^9 km^3	Wallmann (2001)
Seawater sulfate concentration	9 mM	Algeo et al. (2015) (295 Ma)
Riverine input flux	1.5×10^{12} mol/yr	Gill et al. (2011)
Fraction of pyrite sulfur burial	0.24	This study
Pyrite burial flux	3.65×10^{11} mol/yr	This study
Evaporate burial flux	11.35×10^{11} mol/yr	This study
Sulfur isotope composition of riverine input	4.5 ‰	Burke et al. (2018) (present)
Initial sulfate isotope composition	13 ‰	This study
Sulfur isotope fractionation during sulfate reduction	-35 ‰	Algeo et al. (2015)

3.5.2 Interpretation of $\delta^{34}S_{CAS}$ records during the Carboniferous

The most prominent feature of the Carboniferous $\delta^{34}S_{CAS}$ data from Spitsbergen is the rapid fluctuation by ca. 20‰ in the uppermost part of the Mørebreen Member (Figure 3.5), but no such anomaly has been identified in the stratigraphic equivalent Kapitol Member (Figures 3.5 and 3.8) as well as in the published Carboniferous sulfur isotope records (Kampschulte & Strauss, 2004; Wu, 2013; Johnson et al., 2020). Thus, the short-lived, high amplitude $\delta^{34}S_{CAS}$ variations in the upper Mørebreen Member do not likely indicate the global seawater signal, but instead, could be related to the changes in local depositional environments. These horizons contain calcified root remains, thin conglomerate beds, and a minor unconformity surface (Figure 3.4; Chwieduk, 2013), implying relative sea-level fall and subaerial exposure. In addition, micrite dominant-lithofacies bounded by sandy barrier deposits (Figures 3.4C-D) suggest the development of restricted environments, such as lagoons, across the region. The isolation of a regional sulfate reservoir from the exchange with the open ocean results in rapid sulfur isotope shifts in response to regional sulfur isotope changes. For example, coastal lakes of marine origin often show a strong ^{34}S enrichment by more than 30‰ compared with contemporary seawater, where a large portion of the original sulfate has been microbially reduced to sulfide (e.g., Burton & Barker, 1979). Sedimentary facies also indicate the potential influence of terrestrial environments on the $\delta^{34}S_{CAS}$ values in the basal parts of the Scheteligfjellet Formation and the Kapitol Member, both of which are characterized by a transition from terrestrial environments to shallow carbonate platforms (Harland & Geddes, 1997; Dallmann, 1999).

Excluding those with signs of local $\delta^{34}S_{CAS}$ shifts, sulfur isotope data from the Brøggerhalvøya and Nordfjorden sections indicate a Moscovian $\delta^{34}S_{CAS}$ decline followed by stable values throughout the remaining Carboniferous (Figure 3.8). Recently, Johnson et al. (2020) described a positive $\delta^{34}S_{CAS}$ excursion that started near the Serpukhovian-Bashkirian boundary, peaked around the middle of the Bashkirian, and dropped back to its initial value throughout the Moscovian. Afterwards, the $\delta^{34}S_{CAS}$ values remained more stable with less variability until the Permian (Figure 3.8). A positive $\delta^{34}S_{CAS}$

excursion identified by Johnson et al. (2020) is thus in good agreement with our $\delta^{34}S_{CAS}$ data, confirming a perturbation of the global sulfur cycle during the Middle Carboniferous.

3.5.3 Fluctuation in $\delta^{34}S_{CAS}$ values during the Early Permian

In Svalbard, $\delta^{34}S_{CAS}$ values record a steady increasing trend superimposed by short-term oscillations from the late Asselian through the Artinskian (Figures 3.8-3.9). Wu (2013) also reported the two Artinskian $\delta^{34}S_{CAS}$ values significantly higher than the Asselian baseline, but their significance in the global sulfur cycle could not be examined due to a scarcity of published sulfur isotope data from the late Sakmarian to the early Artinskian (Figure 3.9). Our new, high-resolution sulfur isotope data bridge this gap in the $\delta^{34}S_{CAS}$ record, suggesting that the sulfur isotope composition of global seawater sulfate might increase from the late Asselian to the early Artinskian (Figure 3.9). Given the potential influence of depositional environment on the bulk-rock $\delta^{34}S_{CAS}$ record (Rennie & Turchyn, 2014; Richardson et al., 2019b; Ma et al., 2021), however, this study consider both regional and global controls on the sulfur isotope records of the Early Permian succession in Svalbard.
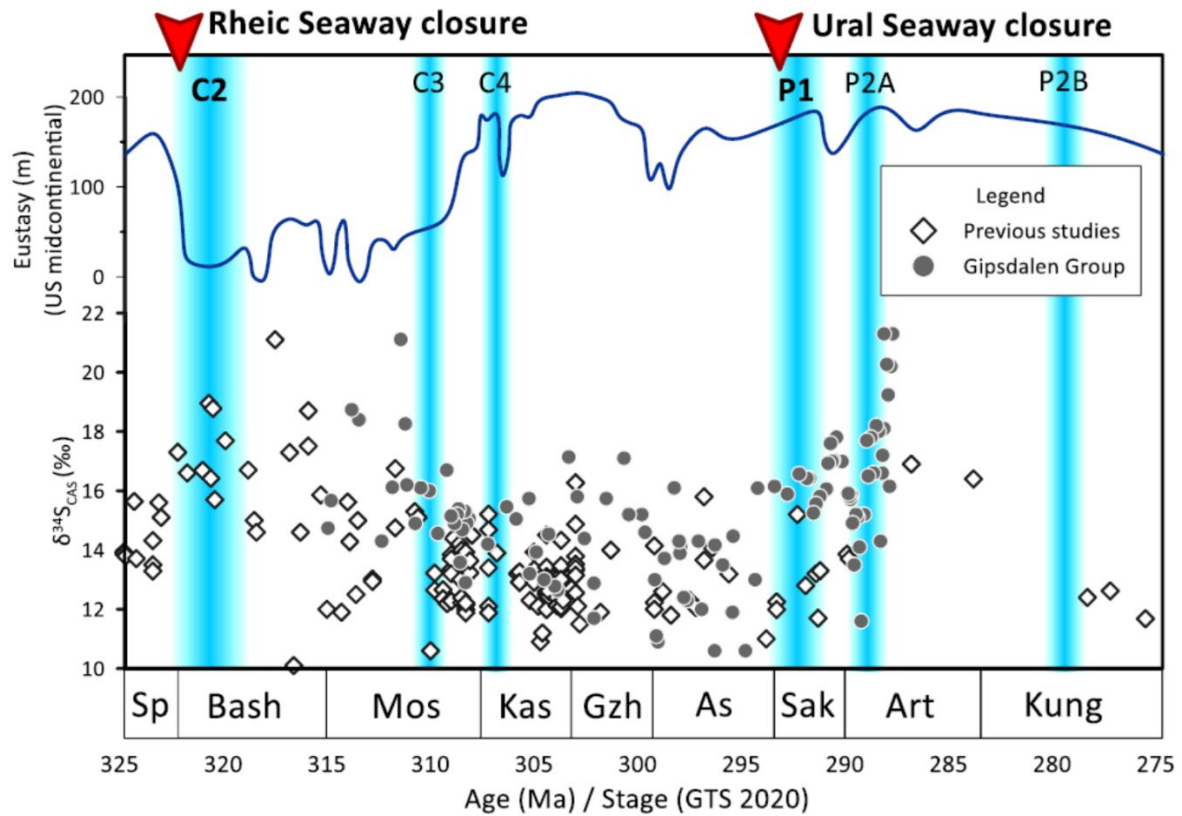
Figure 3.9. Comparison of Permo-Carboniferous $\delta^{34}S_{CAS}$ data (Kampschulte and Strauss, 2004; Wu, 2013; Johnson et al., 2020) with other geological records. A thin blue line in the top frame shows the eustatic sea-level variation (Ross and Ross, 1987). Red wedges mark the closure of major seaways, and vertical-colored bars represent the distribution of glaciation and cooling intervals (Fielding et al., 2008; Davydov, 2018; Davydov and Cózar, 2019). $\delta^{34}S_{CAS}$ values heavier than 22‰ in the upper Mørebreen Member are not presented in this figure.

3.5.3.1 Considerations for regional controls

Unlike the $\delta^{34}S_{CAS}$ anomaly in the upper Mørebreen Member, no $\delta^{34}S_{CAS}$ values in the Early Permian change abruptly in response to short-lived variations in depositional environment, but CAS $\delta^{34}S$ values and their point-to-point variability increase steadily during the Sakmarian to Artinskian sea-level fall in this area (Scheibner et al., 2015; Figure 3.9). In the Brøggerhalvøya section, the average sedimentation rate also increases from the Tyrrellfjellet Member (15 m/Myr) to the Gipshuken Formation (42 m/Myr) according to our age model (Figure 3.3). Recent studies suggest that changes in both relative sea-level and sedimentation rate largely governs the pattern of diagenetic carbonate formation and sulfur transformation, potentially altering the bulk-rock sulfur isotope data and increasing their stratigraphic variability (Rennie & Turchyn, 2014; Richardson et al., 2019a; Richardson et al., 2019b). Rapid sedimentation promotes microbial reduction of porewater sulfate under more closed-system conditions, resulting in porewater sulfate enriched in ^{34}S relative to seawater sulfate, and oxidation of ^{34}S-depleted sulfide to sulfate may also occur during bioturbation or sediment reworking in shallow-water environments. Since the incorporation of those isotopically evolved sulfate into authigenic carbonates affects the bulk-rock $\delta^{34}S_{CAS}$ values, especially those from shallow-water facies, a sharp negative excursion of $\delta^{34}S_{CAS}$ values in the Gipshuken Formation, followed by an equally rapid positive shift, could reflect the alteration of original seawater sulfate signals during early diagenesis. A higher point-to-point $\delta^{34}S_{Py}$ variability in the Sakmarian to Artinskian than in the Asselian further supports the diagenetic alteration in the shallow-water facies at the top of the Gipsdalen Group.

However, it is highly unlikely that changes in local depositional environments play an exclusive role in the Early Permian $\delta^{34}S_{CAS}$ increase identified in the Gipsdalen Group. First, Wu (2013) analyzed two brachiopod samples of the middle to late Artinskian age from North America and reported the $\delta^{34}S_{CAS}$ values as high as 17‰ (Figure 3.9). A good consistency between our results and those by Wu (2013) implies that the elevated Artinskian $\delta^{34}S_{CAS}$ values might be a global phenomenon. Next, Rennie & Turchyn (2014) examined the impact of early diagenesis on the sulfur isotope composition of CAS using both field data and numerical model and showed that $\delta^{34}S_{CAS}$ deviates by no more than 4‰ from

that of overlying seawater sulfate. The full amplitude of the observed sulfur isotopic change clearly exceeds those expected from regional forcing, suggesting that additional factors beyond the local environmental changes must have been involved in an increasing trend of $\delta^{34}S_{CAS}$ during the Early Permian.

3.5.3.2 Early Permian global sulfur cycle

Given that local environmental changes cannot fully account for observed sulfur isotope variations, this study consider the Early Permian $\delta^{34}S_{CAS}$ record to represent a long-term, global increasing trend punctuated by short-term, regional fluctuations. Throughout the Phanerozoic, sedimentary carbon and sulfur isotope records often show a correlation due to the coupled burial of reduced carbon and sulfur on a global scale (e.g. Gill et al., 2011; Johnson et al., 2020). Despite a rapid increase in $\delta^{34}S_{CAS}$ values, however, the Sakmarian to Artinskian period lacks evidence of significant variation in the carbon isotope composition of marine carbonates (Figure 3.5; Grossman et al., 2008; Montañez & Poulsen, 2013; Johnson et al., 2020). Instead, the onset of the Early Permian $\delta^{34}S_{CAS}$ shift coincides with the closure of the Ural Seaway, followed by the expansion of ice sheets over the southern supercontinent Gondwana (Figure 3.9; Davydov, 2018). These tectonic and climatic events could impact the global sulfur cycle, in particular with respect to the sulfur isotope composition of seawater sulfate, by changing the average sulfur isotope fractionation associated with pyrite burial (ε_{avg}), the $^{34}S/^{32}S$ ratios of riverine sulfate ($\delta^{34}S_{in}$), the rate of pyrite burial or a combination of all of these variables.

Average sulfur isotope fractionation associated with pyrite burial

A greater depletion of heavy sulfur isotopes in pyrite relative to seawater sulfate could lead to the rise of $\delta^{34}S_{CAS}$ values. On a global basis, because pyrite burial in shelf environments exhibits a smaller sulfur isotope offset from overlying seawater than that in deep-sea settings (Leavitt et al., 2013; Pasquier et al., 2017), the distribution of shelf environments has been suggested as one of the essential determinants of the sulfur isotope composition of pyrite burial flux (Halevy et al., 2012; Leavitt et al., 2013), and

indeed, the closure of the Ural Seaway diminished shelf area, influencing the average sulfur isotope fractionation associated with pyrite burial. However, box model simulations suggest that diminish of shelf area cannot explain the sulfur isotope excursion. In this scenario, ε_{avg} and the riverine input flux (F_w) were changed in the model, while $\delta^{34}S_{in}$ and F_{py} remain constant. To reproduce the data, the ε_{avg} increase from 35‰ to 75‰ and a 1.2-fold increase in F_w are required, where the initial seawater sulfate concentration is 9 mM.(Figure 3.10). A sensitivity test with the smaller reservoir (4.5 mM) demands a 30‰ increase in ε_{avg} and a 1.1-fold increase in F_w. A model run with the larger reservoir (18 mM) requires a 70‰ increase in ε_{avg} and a 1.4-fold increase in F_w to reproduce the $\delta^{34}S_{SO4}$ trend. As a 1‰ increase in fractionation necessitates the decrease of the shelf area as large as 6×10^6 km^2 (Leavitt et al., 2013), 30‰ increase of the ε_{avg} indicates the decrease of the global shelf area equivalent to one third of the Earth surface area. Such an unrealistic change suggests that a variation in isotope fractionation does not explain the Early Permian $\delta^{34}S_{CAS}$ shift.

The $^{34}S/^{32}S$ ratios of riverine sulfate

An increase in the $\delta^{34}S$ of riverine sulfate is another potential mechanism for the positive $\delta^{34}S_{CAS}$ shift. Since riverine sulfate is sourced primarily from the weathering of ^{34}S-depleted pyrite and ^{34}S-enriched sulfate evaporite (Burke et al., 2018; Kemeny et al., 2021), an increasing ratio of evaporite to pyrite weathering could shift the $\delta^{34}S$ of riverine sulfate to more positive values. The closure of Ural Seaway and continental collision, evidenced by the termination of marine sedimentation in the southern part of the Ural Basin, must have exposed former shelf areas where evaporite were the predominant rocks (Chwieduk, 2013; Davydov, 2018). Therefore, evaporite dissolution may provide a possible explanation for the rapid rise of $\delta^{34}S_{CAS}$.

Our box model analysis assuming a modest increase in seawater sulfate levels during the Early Permian (Algeo et al., 2015) suggests that a $\delta^{34}S_{in}$ increase from 4.5‰ to 13.5‰ to reproduce the observed $\delta^{34}S_{CAS}$ increase with 9 mM of initial seawater sulfate concentration (Figure 3.11). When the initial seawater sulfate levels are 4.5 mM and 18 mM, $\delta^{34}S_{in}$ values need to be raised to 10.5‰, and

17.8‰, respectively, while the magnitude of F_w increase is same with those in the first scenario. Although little is known about the secular variation in $\delta^{34}S$ of riverine sulfate over geologic time, such high values lie more than one standard deviation away from the flux-weighted average of the modern rivers (Burke et al., 2018) and even close to the $\delta^{34}S$ values of seawater sulfate prior to the Sakmarian anomaly. Given the rapid recycling of recently deposited sulfur (Halevy et al., 2012), the global riverine $\delta^{34}S$ hardly approximates the $\delta^{34}S$ of contemporaneous seawater sulfate unless almost all riverine sulfate comes from evaporite dissolution. Therefore, changes in the continental sulfate input likely contributed to but might not solely trigger the Early Permian rise of $\delta^{34}S_{CAS}$.

Pyrite burial flux

For the parameters influence to the global sulfur cycle, the remaining alternative is the high rate of pyrite burial in the Early Permian oceans. Pyrite burial is coupled with that of organic carbon via dissimilatory sulfate reduction, and the apparent lack of positive $\delta^{13}C$ shift in the studied sections and literature (Figures 3.5 and 3.8; Grossman et al., 2008) suggests that global organic carbon burial did not increase significantly during the Early Permian. However, it is noteworthy that the relationship between organic carbon and pyrite burial can change depending on the locus of carbon burial. Compared with marine realm, pyrite formation may be less favored in terrestrial settings due to the limited availability of sulfate (Berner & Raiswell, 1983). Therefore, if the primary locus of organic carbon burial shifts from terrestrial to marine environments, more sulfur could be removed from the ocean as pyrite without increasing the rates of global organic carbon burial. This scenario is plausible for two reasons. First, the closure of Ural Seaway, followed by an ice-age period, could decrease the terrestrial organic carbon burial due to the increased aridity and the presence of large ice sheets. More importantly, the greater iron transport by eolian dust from arid and glacial regions (Sur et al., 2015; Oordt et al., 2020) could increase the marine productivity and thereby the amount of organic carbon buried in marine sediments. Enhanced preservation of organic carbon in deep-sea sediments has been also reported for the Cenozoic ice ages (Hoogakker et al., 2018; Anderson et al., 2019). To evaluate the influence of pyrite burial rate

increase, pyrite burial flux (F_{py}) and F_w in the model were changed, with constant $\delta^{34}S_{in}$ and ε_{avg} (Figure 3.12). In this scenario, a 2.6-fold increase in F_{py} and a 1.6-fold increase in F_w are required. Sensitivity tests for the initial sulfate concentrations of 4.5 and 18 mM require ×2.0 and ×3.7 increases in F_{py} and ×1.4 and ×2.0 increases in F_w, respectively. The resulting rate of pyrite burial is not exceptionally high relative to most of the Phanerozoic, since our model assumes the steady-state rate of Permo-Carboniferous pyrite burial to be about half of the Phanerozoic average (Table 3.3; Berner & Raiswell, 1983). Thus, enhanced pyrite burial alone could explain the Early Permian $\delta^{34}S_{CAS}$ shift within a plausible quantitative framework. By taking the highest estimate instead of the mean trend of seawater sulfate (Algeo et al., 2015), however, the model requires a rather high, 3.7-fold increase in pyrite burial to reproduce the data (Figures 3.12-13); changes of similar magnitude have been proposed before for the Phanerozoic sulfur isotope excursions (e.g., Kurtz et al., 2003).

Combined model of pyrite burial and $\delta^{34}S$ of riverine sulfate

To examine the combined effect of two potential causal factors, the pyrite burial rate and the $\delta^{34}S$ of riverine sulfate were changed in the model. In principle, the more [34]S-enriched the riverine sulfate becomes, the less amount of pyrite is required to be buried to generate the observed isotopic shift (Figure 3.13D). For example, if the $\delta^{34}S$ of riverine sulfate increases by 3‰ from its steady-state value, which is within the range of uncertainty of the reference data (Burke et al., 2018), only a moderate increase in pyrite burial (< 3 times) would be required for the model to reproduce the trend observed in the data even at seawater sulfate concentrations as high as 18 mM, the maximum estimate for the Early Permian (Figure 3.14; Algeo et al., 2015). As discussed earlier, geological evidence suggests that continental collision and subsequent environmental changes (Davydov, 2018; Davydov & Cózar, 2019) could accelerate the rate of pyrite burial while potentially increasing the $\delta^{34}S$ values of riverine sulfate, and here, the results of model simulation confirm that this hypothesis provides a good quantitative fit to our current understanding of the Early Permian sulfur cycle.

Evaluation for age uncertainty

Uncertainties in the calibrated ages may arise from diachronous lithostratigraphic boundaries or low temporal resolution of foraminiferal biostratigraphy (Hüneke et al., 2001) and it can potentially change the model results. The lithologic boundary between the Kapitol and the Tyrrellfjellet members can be diachronous (Hüneke et al., 2001), and the degree of diachronism appears to be about half a million years considering the duration of the *D. sokensis* zone (Nilsson & Davydov, 1997; GTS 2020). However, as these two members span nearly 23 million years (Figure 3.3), the probable errors due to such diachronism is not significant in this study. While the probable errors in the boundary ages are commonly much smaller than the time spanned by each lithostratigraphic unit, a notable exception is the Gipshuken Formation. Age uncertainty of the Gipshuken Formation is 2Ma in our age model. Since the age of the Gipshuken Formation is the largest source of uncertainty, how this uncertainty could alter the Permian sulfur isotope record was examined (Figure 3.15). In addition to the age model presented in Figure 3.3, the sulfur isotope data using an alternative model were plotted that assumes (1) the middle Sakmarian Tyrrellfjellet-Gipshuken transition, (2) the age of the uppermost Gipshuken Formation closes to that of the basal Kapp Starostin Formation, or (3) both. As can been seen in Figure 3.15, different age models estimate the rates of $\delta^{34}S$ change ranging from 0.55‰ to 0.66‰ per million years, which can be translated into the increase in pyrite burial by a factor of 2.6 to 2.8 without altering $\delta^{34}S$ of riverine input (e.g. Figure 3.13). This age uncertainty, therefore, would not influence by more than 10% of the quantitative interpretation of the Early Permian $\delta^{34}S_{CAS}$ anomaly.

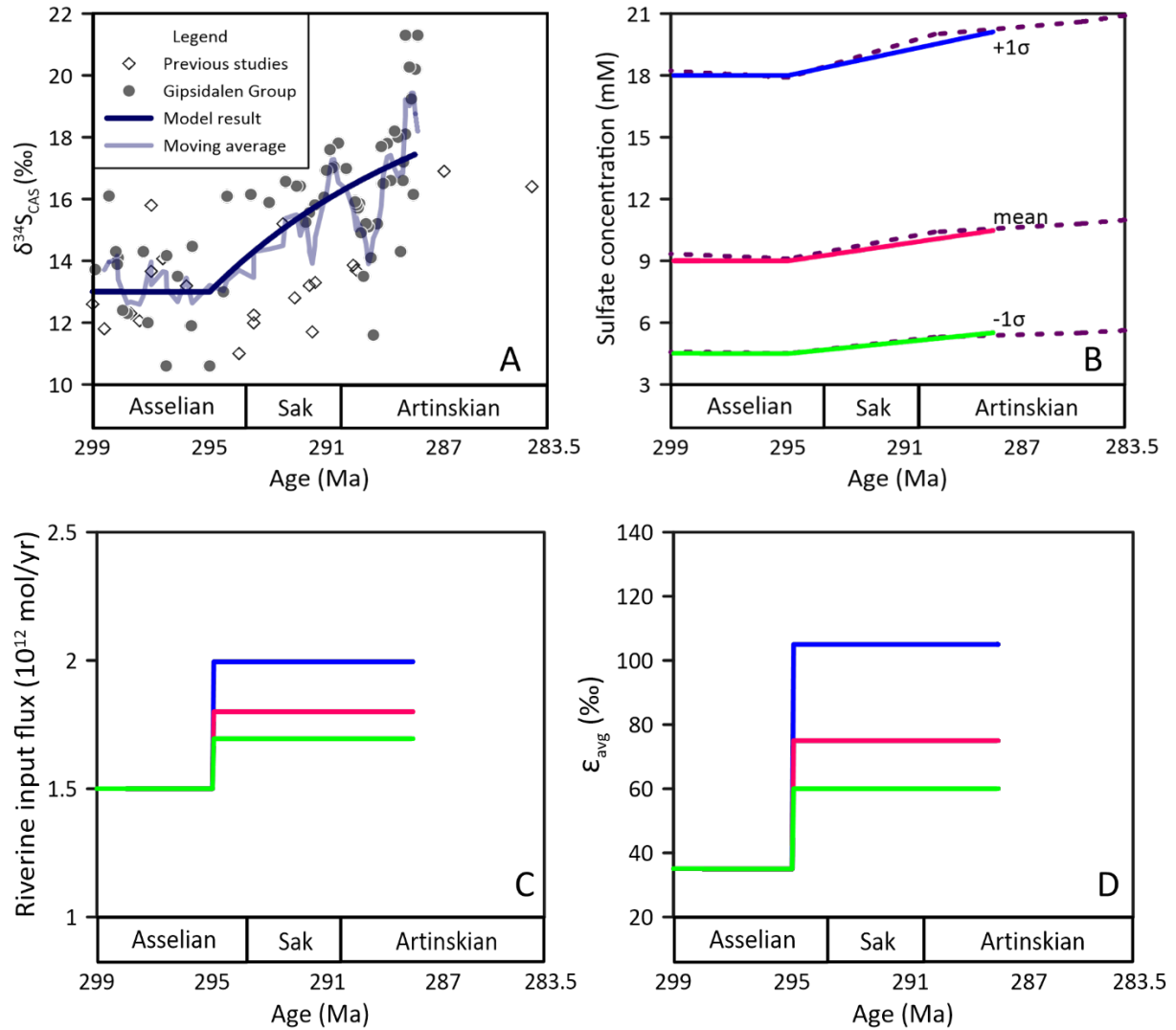**Figure 3.10.** Model of dynamic $\delta^{34}S_{SO4}$ and seawater sulfate concentration in response to the changes in ε_{avg} and riverine sulfate flux. (A, B) Model runs with increased ε_{avg} and F_w reproduce the variations in $\delta^{34}S_{CAS}$ (this study) and seawater sulfate concentrations (dashed lines; Algeo et al., 2015). (C, D) As the initial sulfate concentration increases from 4.5, 9, to 18 mM, model needs a greater increase in both ε_{avg} and F_w values. Green line – 4.5 mM; Red line – 9 mM; Blue line – 18 mM.
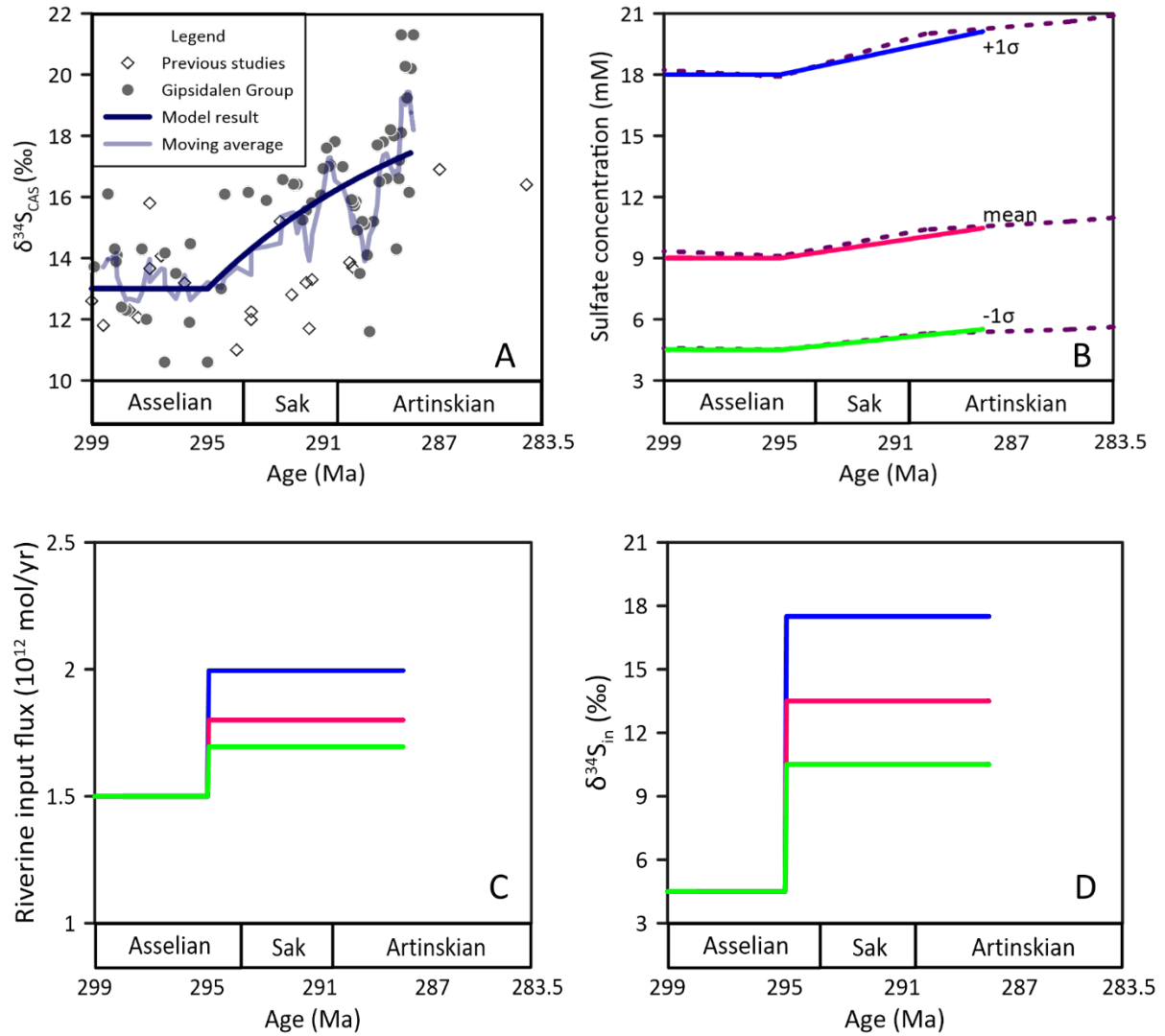
Figure 3.11. Model of dynamic $\delta^{34}S_{SO4}$ and variation of sulfate concentration in response to the changes in $\delta^{34}S_{in}$ and riverine input flux. (A, B) Model runs with increased $\delta^{34}S_{in}$ and F_w replicate the variations in $\delta^{34}S_{CAS}$ (this study) and seawater sulfate concentrations (dashed lines; Algeo et al., 2015). (C, D) As the initial sulfate concentration increases from 4.5, 9, to 18 mM, model needs a greater increase in both $\delta^{34}S_{in}$ values and riverine input flux. Green line – 4.5 mM; Red line – 9 mM; Blue line – 18 mM.

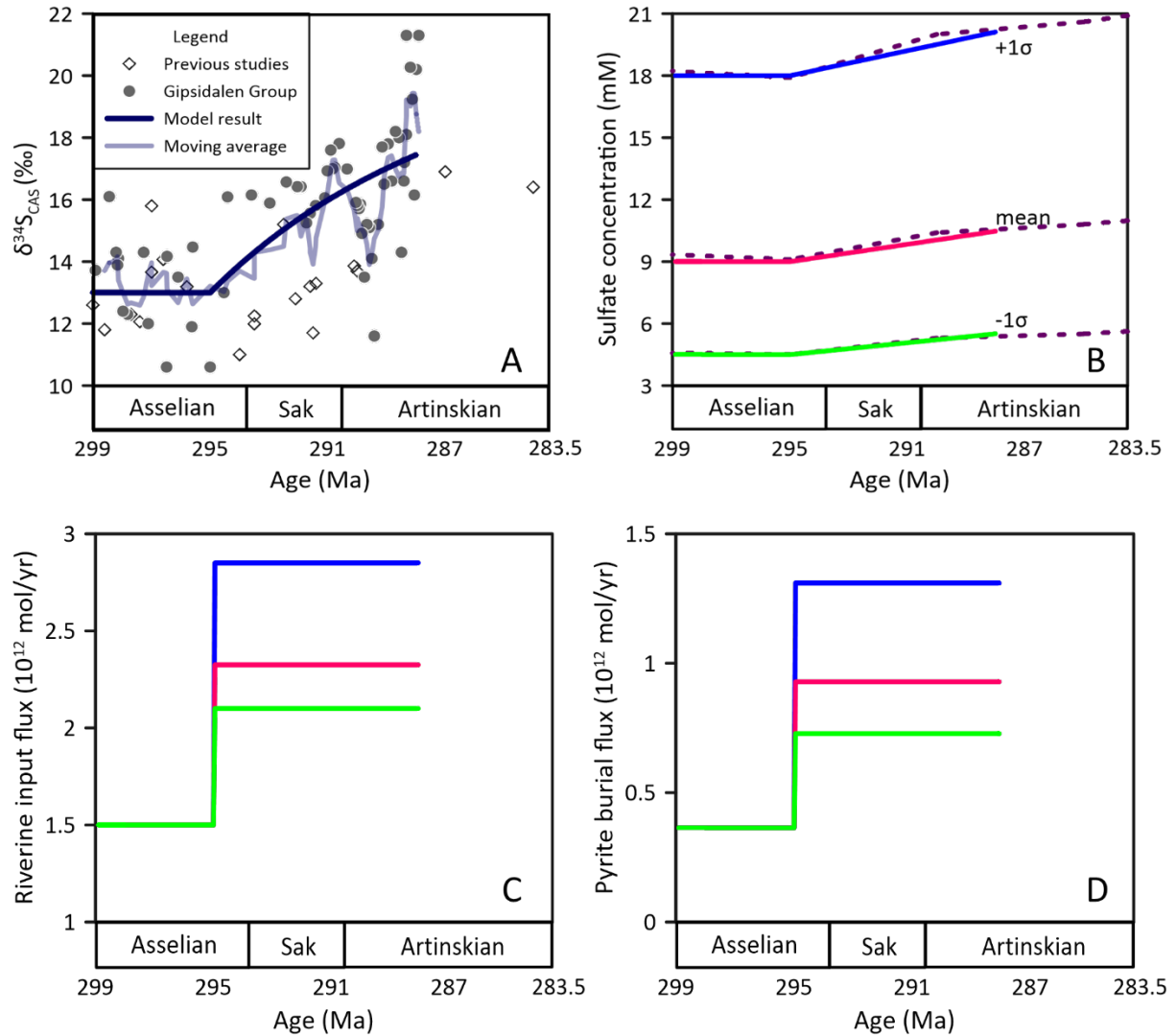**Figure 3.12**. Model of dynamic $\delta^{34}S_{SO4}$ and variation of sulfate concentration in response to the changes in pyrite burial flux and riverine input flux. (A, B) Model runs with increased pyrite burial flux and F_w replicate the variations in $\delta^{34}S_{CAS}$ (dashed lines; this study) and seawater sulfate concentrations (Algeo et al., 2015). (C, D) As the initial sulfate concentration increases from 4.5, 9, to 18 mM, model needs a greater increase in both pyrite burial and riverine input flux. Green line – 4.5 mM; Red line – 9 mM; Blue line – 18 mM.
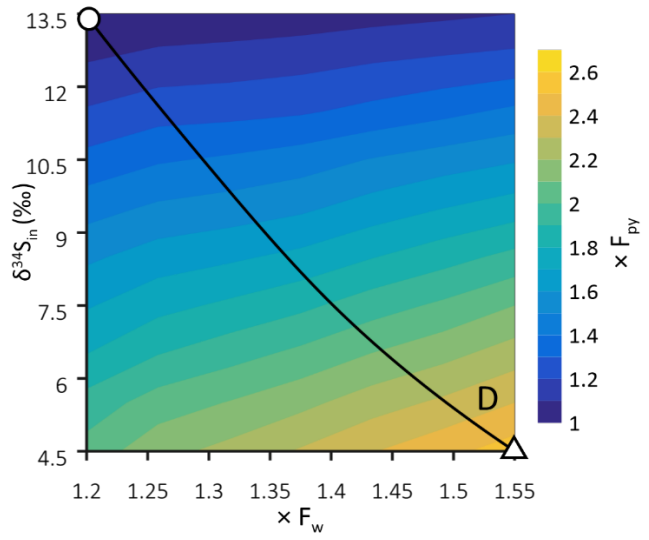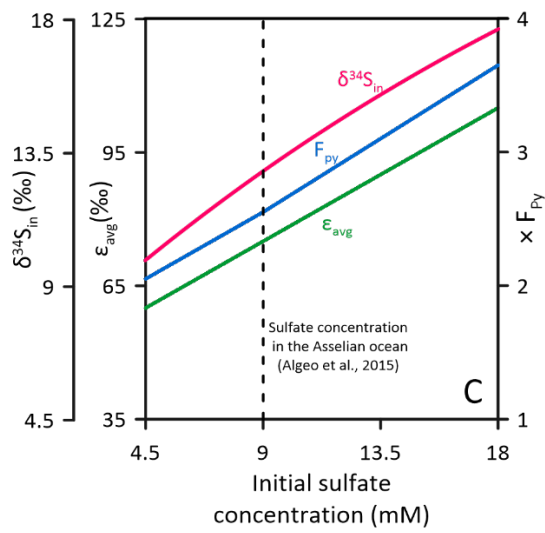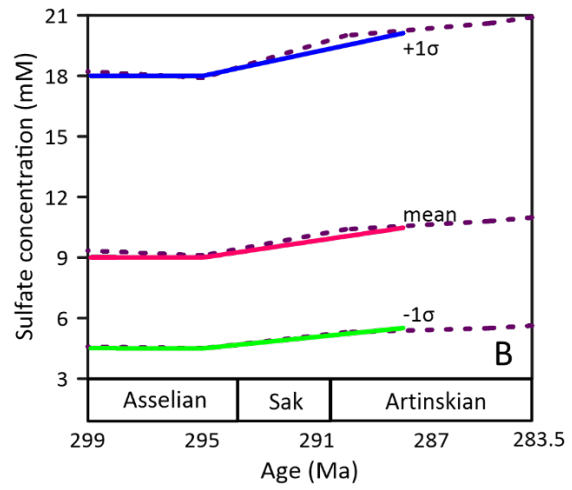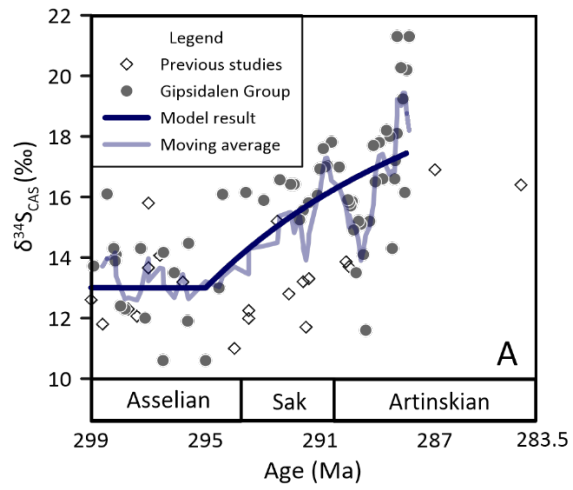
Figure 3.13. Results from box model simulations for the Early Permian sulfur cycle. (A) Modeled curve compared to the moving average of $\delta^{34}S_{CAS}$ data, including that from the literature (Wu, 2013; Johnson et al., 2020) and this study. (B) Model results of seawater sulfate concentration. Purple dashed lines show the minimum, mean, and maximum estimates of the seawater sulfate concentration during the Early Permian from Algeo et al. (2015), and solid lines are the model results of each case. (C) Influence of marine sulfate reservoir size on the model parameters to reproduce the Early Permian $\delta^{34}S_{CAS}$ record. Note that the initial steady-state values of ε_{avg} and $\delta^{34}S_{in}$ are 35 and 4.5‰, respectively. (D) The contour plot illustrates the relationship between pyrite burial, riverine input, and $\delta^{34}S$ of riverine sulfate to reproduce the Early Permian perturbation of global sulfur cycle at the steady-state seawater sulfate concentration of 9 mM. The solid black line denotes a series of model runs to reproduce variations in not only the $\delta^{34}S$ values but also the reservoir size of seawater sulfate. Empty triangles and circles represent the end-member solutions that could reproduce the entire trend without altering the $\delta^{34}S$ of riverine input and pyrite burial, respectively.
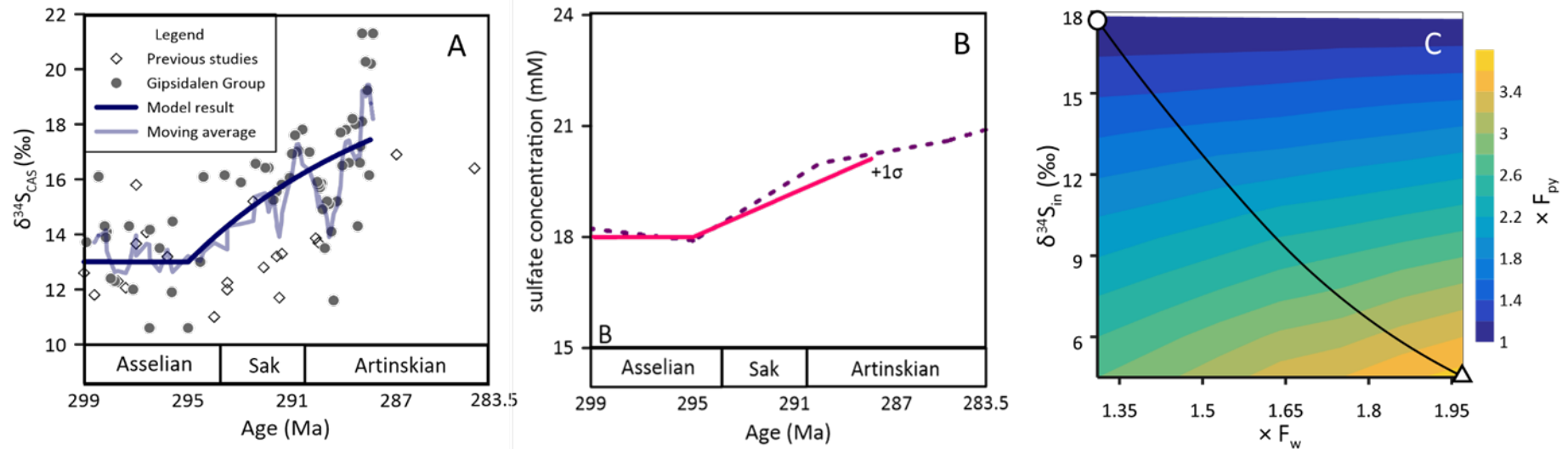
Figure 3.14. Sensitivity of the model simulation with three tunable parameters (F_{py}, F_w, and $\delta^{34}S_{in}$) for the Early Permian seawater sulfate concentration. (A, B) Both a positive $\delta^{34}S_{SO4}$ shift and a maximum estimate of the seawater sulfate concentration (dashed line; Algeo et al., 2015) can be reproduced when the pyrite burial increases by 185%, the riverine sulfate input increases by 75%, and the $\delta^{34}S$ of riverine sulfate increases from 4.5‰ to 7.5‰ (red lines) at 295 Ma. Note that this example does not represent all possible solutions. (C) The contour plot illustrates the relationship between pyrite burial, riverine input, and $\delta^{34}S$ of riverine sulfate for reconstructing the Sakmarian $\delta^{34}S_{SO4}$ anomaly. The solid black line denotes a series of model runs to reproduce variations in not only the $\delta^{34}S$ value but also the reservoir size of seawater sulfate. Empty triangle and circle stand for the end-member solutions that could reproduce the entire trend without altering $\delta^{34}S$ of riverine input and pyrite burial, respectively.
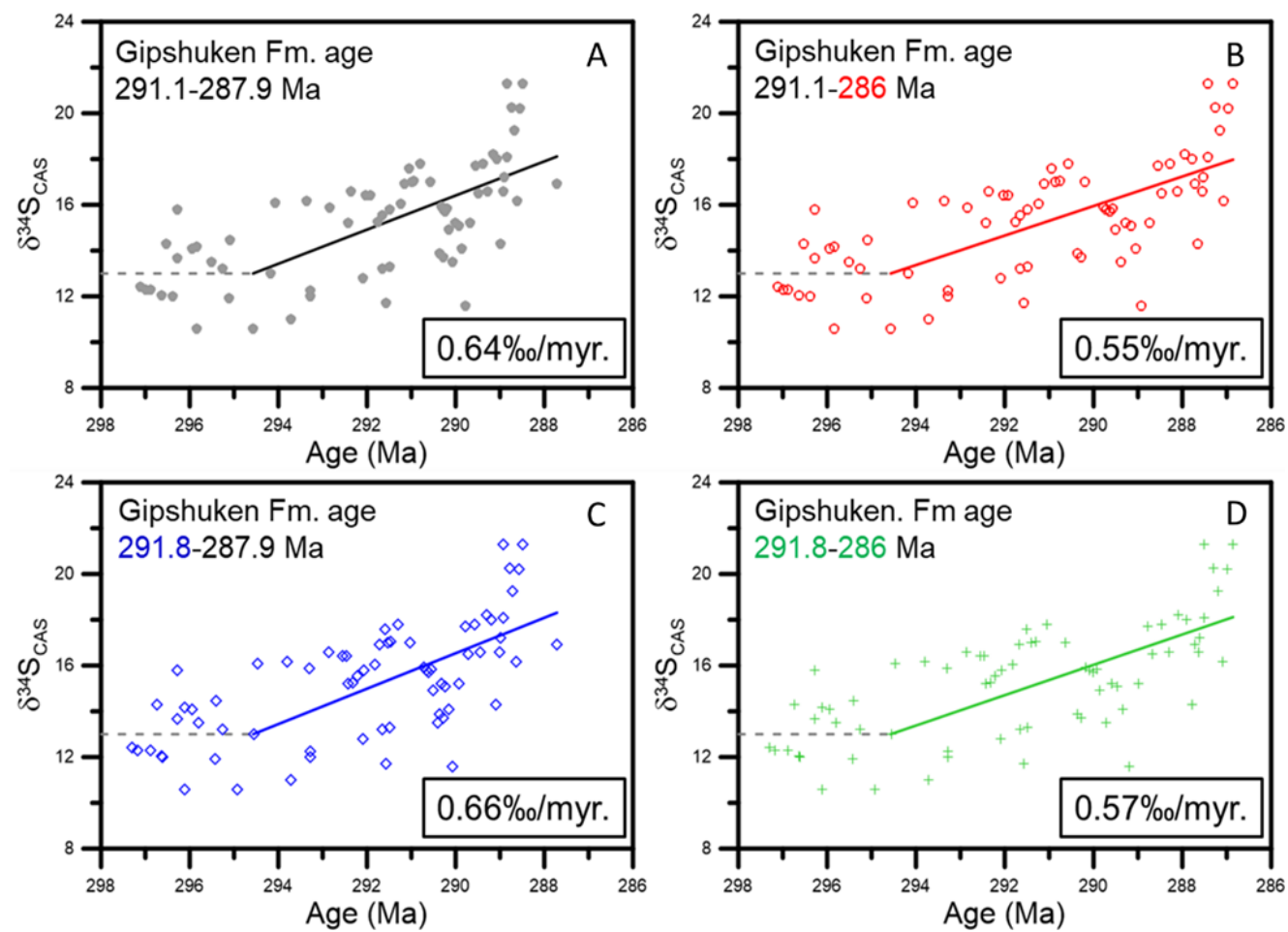
107

Figure 3.15. Influence of the age model on the calculated rates of the Early Permian $\delta^{34}S_{CAS}$ increase.

3.5.4 Comparison of the Sakmarian $\delta^{34}S_{CAS}$ anomaly with the Bashkirian Event

The Sakmarian positive sulfur isotope anomaly, along with that of the Bashkirian (Johnson et al., 2020), highlights that the Carboniferous to Early Permian is not a period of quiescence as far as the sulfur cycle is concerned. Both events share notable common features, but also show some distinct differences. They have comparable amplitude (Figure 3.9), and rates of $\delta^{34}S_{CAS}$ increase have been estimated to be 0.83 and 0.64 ‰/Myr for the Bashkirian and the Sakmarian events, respectively. The onset of those events corresponds to the expansion of Gondwana ice sheets (Figure 3.9), triggered by the closing of the major seaways between the Paleotethys and Panthalassa oceans (Davydov, 2018; Davydov & Cózar, 2019). These two events, however, contrast with each other in terms of eustatic sea-level change. While the Bashkirian event accompanies a drastic fall in eustatic sea-level (Johnson et al., 2020), no significant change in eustatic sea-level is associated with the closure of the Ural Seaway (Figure 3.9). As such, the proposed mechanisms behind these two similar sulfur isotope anomalies reveal some intriguing contrasts. Erosion of sulfate evaporite has been recognized as one of the underlying causes of both Sakmarian and Bashkirian events (this study; Johnson et al., 2020), but instead of the high rates of pyrite burial, Johnson et al. (2020) proposed a larger sulfur isotope fractionation associated with pyrite formation, driven by a shrinkage of shallow shelf environments, as a major driver for the Bashkirian sulfur isotope anomaly. This interpretation assumes that marine organic burial did not change significantly, while the formation of coal forests on the exposed shelf areas increased the global burial of organic carbon (Johnson et al., 2020). However, although perhaps not as dramatically as the increase in terrestrial organic sedimentation, the rates of marine organic and pyrite burial might also increase upon the closure of the Rheic Seaway and the ice sheet expansion at that time, as discussed earlier for the Sakmarian sulfur cycle. Previously, a relatively large increase in the sulfur isotope fractionation up to 50‰ was suggested to explain the Bashkirian $\delta^{34}S_{CAS}$ excursion (Johnson et al., 2020), but the necessary changes would become more reasonable if additional pyrite were sequestrated in marine sediments. The assembly of the supercontinent Pangea might impact the

Middle Carboniferous sulfur cycle by increasing not only the sulfur isotope fractionation but also, probably, the rate of pyrite burial.

3.6 Conclusion

This study presents a high-resolution sulfur isotope record from carbonate successions in Svalbard spanning the Moscovian to Artinskian time interval. While Svalbard $\delta^{34}S_{CAS}$ data are compatible with the existing Late Carboniferous record, they reveal a steady increase in $\delta^{34}S_{CAS}$ values superimposed by rapid oscillations during the Early Permian. Changes in relative sea-level and sedimentary facies are well correlated with short-term $\delta^{34}S_{CAS}$ fluctuations but cannot account for a long-term $\delta^{34}S_{CAS}$ increase from the latest Asselian to the middle Artinskian. Instead, this sulfur cycle perturbation initiated contemporaneously with the closure of the Ural Seaway and the ice sheet expansion in Gondwana. A global expansion of arid and glacial regions might limit terrestrial organic burial but support more organic carbon burial in marine sediments via increased iron transport to the ocean. Thus, more sulfates could be removed from the ocean as pyrite, increasing the $\delta^{34}S_{CAS}$ values of seawater sulfate. Across the closure of the Ural Seaway, the erosion of sulfate evaporite likely influenced the amount and sulfur isotope composition of riverine input, providing an additional forcing for the Early Permian sulfur isotope event. In contrast, no major sea level drop during the Early Permian implies that greater ^{34}S depletion in pyrite relative to seawater sulfate, resulting from a reduction in shallow shelf environments, unlikely played a quantitatively relevant role in the observed $\delta^{34}S$ record. The overall conclusions about the dynamic interactions among geography, glaciation, and the sulfur cycle improve our understanding of the sulfur isotope signatures not only throughout the Early Permian but also during other tectonic or climatic events.

Chapter 4. Bulk-rock CAS extraction method for MC-ICP-MS analysis

4.1 Introduction

The isotope composition of carbonate associated sulfate (CAS) has been widely used to reconstruct the ancient sulfur cycle due to its continuity and accessibility (Kampschulte & Strauss, 2004; Hurtgen et al., 2002; Wotte et al., 2012; Present et al., 2020). However, the content of CAS is generally low in carbonate samples, requiring CAS extraction experiment for isotope measurement. Previous studies have proposed two methods of CAS extraction: a traditional bulk rock CAS extraction protocol (Hurtgen et al., 2002; Wotte et al., 2012) and microscale CAS extraction from microfossils (Das et al., 2012; Paris et al., 2013; Paris et al., 2014b; Present et al., 2015). In the traditional extraction method (Wotte et al., 2012), 50-80 g of samples were rinsed by 10% NaCl solution three times to remove external sulfate. Rinsed samples were dissolved by 6 M HCl for 2 hours and barium sulfate was precipitated by barium chloride. The $BaSO_4$ precipitate was analyzed by Isotope Ratio Mass Spectrometry (IR-MS). Microscale CAS extraction method use 10-50 mg of samples from fossils or carbonate texture (Paris et al., 2013; Paris et al., 2014b; Present et al., 2015; Rennie et al., 2018; Johnson et al., 2020). Samples are rinsed in NaCl solution to eliminate external sulfate and dissolved in HCl for 4-12 hr. Samples are centrifuged and the supernatant was extracted and purified for sulfur isotope analysis in multi-collector inductively coupled plasma mass spectrometer (MC-ICP-MS).

While both methods have provided several $\delta^{34}S_{CAS}$ data for reconstructing ancient sulfur cycles from various regions (Present et al., 2020), they also have several challenges. The traditional method devised by Wotte et al. (2012) cannot be used if CAS contents in carbonate samples are too low. Furthermore, the presence of pyrite in the carbonate can lead to pyrite oxidation during dissolution, potentially altering CAS isotope values (Marenco et al., 2008). For example, this thesis conducted CAS extraction experiment for Joseon Supergroup samples in Chapter 2, but the CAS isotope value can only be

measured for 33 samples among the 125 samples experimented with. In addition, for the samples in the Taebaek area, the isotopic value of CAS is much lower than the Ordovician record in other regions (Figure 4.l), indicating possible experimental pyrite oxidation.

Because the minimum concentration of sulfate required to isotopic analysis for MC-ICP-MS is lower than IR-MS, the microscale CAS extraction allows for the analysis of the sample that have low sulfate contents (Das et al., 2012; Paris et al., 2013; Paris et al., 2014b; Present et al., 2015; Moon et al., 2021). Also, this method can prevent pyrite oxidation since microfossils do not contain pyrite. However, achieving the same level of resolution as in bulk rock samples is challenging for microfossil CAS analysis. Insufficient resolution possibly obscures the records of seawater sulfate isotopes (Section 3.1 in Chapter 3). Therefore, an improvement in CAS extraction method is necessary to obtain high-resolution seawater sulfate signal.

To reconstruct the biogeochemical sulfur cycle of the Earth, it is crucial to have high-resolution data that are free from contamination, indicating that improving the CAS extraction method is important issue. Therefore, this study introduces a new protocol for mesoscale CAS extraction experiments, which involve extracting CAS from bulk rock samples and analyzing sulfate ions using MC-ICP-MS. Combining advantages of traditional method and microscale methods, the mesoscale extraction method is expected to enable CAS extraction from bulk carbonate samples with low sulfate contents. Since experimental pyrite oxidation is caused by the acid used during the experiment, reducing the exposure time to acid may be effective in preventing pyrite oxidation. Therefore, this chapter also try to prevent pyrite oxidation by controlling the dissolution time in mesoscale experiment. The ultimate aim of this chapter is to analyze CAS isotope data from the Joseon Supergroup samples, which is not reported in Chapter 2, using the mesoscale extraction method.

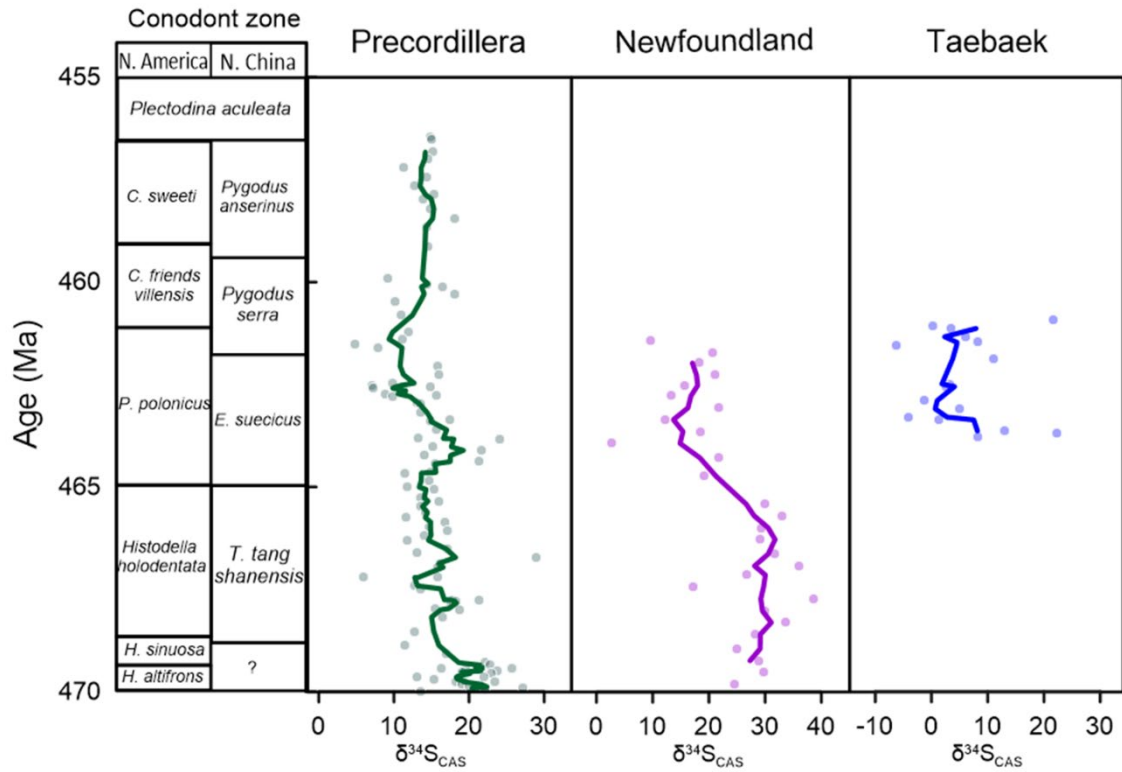**Figure 4.1**. Comparison of CAS isotope curve between Precordillera (Thompson & Kah, 2012), Newfoundland (Kah et al., 2016), and Taebaek (Chapter 2 in this study). Green, purple, and blue lines indicate five-point moving average curve of the Precordillera, Newfoundland, and Taebaek, respectively. It is important to note that $\delta^{34}S_{CAS}$ in the Taebaek represent more than 10% lower isotopic values compare to other regions.

4.2 Methods

4.2.1 Mesoscale CAS extraction protocol and its evaluation

Flow chart of the mesoscale CAS extraction protocol is Figure 4.2. The mesoscale CAS extraction protocol utilized 1 gram of bulk carbonate powder. The samples were subjected to a rinsing process using 50 ml of 10% NaCl solution three times, followed by rinsing with deionized water to remove water-soluble external sulfate (Wotte et al., 2012). The rinsed samples were dissolved using 25 ml of 1 M HCl. To prevent pyrite oxidation, the carbonate dissolution time was less than 10 minutes in this method because shorter dissolution time reduces the exposure of pyrite to the acid. It would be tested that if the carbonate dissolves enough in 10 minutes. After dissolution of carbonate, the supernatant was extracted using a syringe, and any insoluble residue was filtered using a PES syringe filter. Sulfate concentration in the filtered supernatant was measured using ion chromatography equipped with an AS-19 column and a KOH eluent. The mesoscale protocol is based on the microscale extraction method (Present et al., 2015) but using a larger amount of bulk carbonate sample rather than fossils. Compared to the traditional method (Wotte et al., 2012), the mesoscale method uses less amount of powder, and the dissolution time of carbonate is shorter. In addition, the sulfate isotopes are analyzed in MC-ICP-MS in the form of an aqueous solution for the mesoscale experiment, whereas they are analyzed in IR-MS as the form of barium sulfate precipitate in the traditional method.

For isotopic analysis, the sulfate ions in the samples were recovered using AG1-X8 anion exchange resin. 1.4 ml of resin was filled in the column, and the resin was rinsed with 28 ml of hydrochloric acid, nitric acid, and deionized water. The resin was then rinsed once again with 0.2 M HCl. The samples were loaded into the column, and any cations present in the sample were eliminated using 28 ml of deionized water. The sulfate ions in the samples were recovered by eluting with 8 ml of nitric acid, which was collected in a Teflon vial. The samples in the Teflon vial were dried on a hot plate set to 105°C for 12 hours. The Teflon vial used for sulfate ion recovery was rinsed with deionized water five times and subsequently heated in 6 M HCl for 24 hours. The Teflon vials were washed five times with

deionized water, and the same process was repeated using 8 M nitric acid. Additionally, the Teflon vials containing 50 μl of 0.8 M high-purity nitric acid were heated on a hot plate at 160°C for 12 hours. They were then washed five times with ultra-pure distilled water and reused to prevent contamination between samples.

Based on the ion chromatography measurement, the samples were diluted in auto sampler vials to achieve a sulfate concentration equivalent to a 20 μM Na_2SO_4 bracketing standard. The sulfur isotope ratios in the samples were analyzed using a Nu Plasma 3 multi-collector inductively coupled plasma mass spectrometer (MC-ICP-MS), which was installed at the National Center for Inter-University Research Facilities (NCIRF) in Seoul National University. For the MC-ICP-MS analysis, the samples were injected using an ESI PFAF-100 nebulizer and a Cetac Aridus II desolvator. The sulfur isotope ratios were measured at a mass resolution of 8000 (M/ΔM*) using three Faraday detectors (L4, H1, H6). The accuracy of $\delta^{34}S$ analysis, as confirmed by the IAEA-SO-5 standard, was found to be less than 0.44‰ (2σ). A detailed information of the analysis technique using MC-ICP-MS is described in Moon et al. (2021).

To assess the precision and reproducibility of the mesoscale bulk-rock CAS extraction method, a lime mudstone and a dolo mudstone samples from Svalbard were selected. These samples are from the Wordiekammen Formation, the Late Carboniferous strata in the Svalbard. Detailed description of Wordiekammen Formation is in Chapter 3 geological setting section. They have low pyrite content and high CAS content (Table 4.1), suggesting that CAS isotope value of these samples show little alteration by experimental pyrite oxidation. CAS isotope value of Svalbard samples with traditional method were measured 3 times, and contents of precipitated sulfate are 477-583 ppm for limestone sample. Measured once, pyrite concentration of the Svalbard limestone sample is 6 ppm. CAS contents of the dolostone sample is 751-921 ppm and pyrite content cannot be measured due to low contents.

To evaluate precision, a comparison was made between CAS isotope data analyzed using the traditional method ($\delta^{34}S_{trd}$) and the mesoscale method ($\delta^{34}S_{ms}$). This comparison allowed for assessing

the consistency of CAS isotope measurements between the two methods. For the reproducibility test, the entire mesoscale CAS extraction protocol and isotope analysis were repeated five times for limestone and dolostone samples. The dissolution time test was performed to investigate the potential impact of different carbonate dissolution times in hydrochloric acid on isotopic data. The traditional method (Wotte et al., 2012) involves dissolving carbonate samples for over 2 hours to ensure complete dissolution. In contrast, the mesoscale method has a shorter dissolution time of 5-10 minutes. This study compared CAS concentration and isotopic values in samples with different dissolution times (15 minutes, 30 minutes, 1 hour, 2 hours) to examine any potential effects on the results.

Another important reason for developing this method is to prevent pyrite oxidation. To verify the mesoscale CAS extraction method can prevent pyrite oxidation, mixed carbonate-pyrite samples were treated three times. By comparing the CAS isotope value of the carbonate-pyrite composite samples with that of the original samples, it can be determined whether pyrite oxidation occurred during CAS extraction. For this test, the isotope value of the pyrite used was measured to be 3.5‰ (±0.8). In addition, CAS isotope data of carbonate rocks from the Joseon Supergroup in the Korean Peninsula were analyzed using this protocol to confirm the reliability of the extraction method in low CAS and high pyrite contents sample. Six samples were selected from the Duwibong formation in Taebaek and eight from the Yeongheung formation in Yeongwol. The geological setting and sampling location of these samples are described in Section 2.2 of Chapter 2. For all these samples, the contents and isotopic values of precipitated sulfate and pyrite contents were reported using the traditional method (Table 4.2).

Sample preparation
1 g of bulk carbonate powder

Sample cleaning
10% NaCl, 50 ml, X3
DW, 50 ml, X1

Dissolution
1 M HCl, 25 ml, 5-10 min

Filtering
PES syringe filter

Quantification
ion chromatography
AS-19 column

Purification
AG1-X8 resin, 1.4 ml

Drying
105°C , 12 hours

Dilute in HNO$_3$
0.8 M, ultra-pure grade

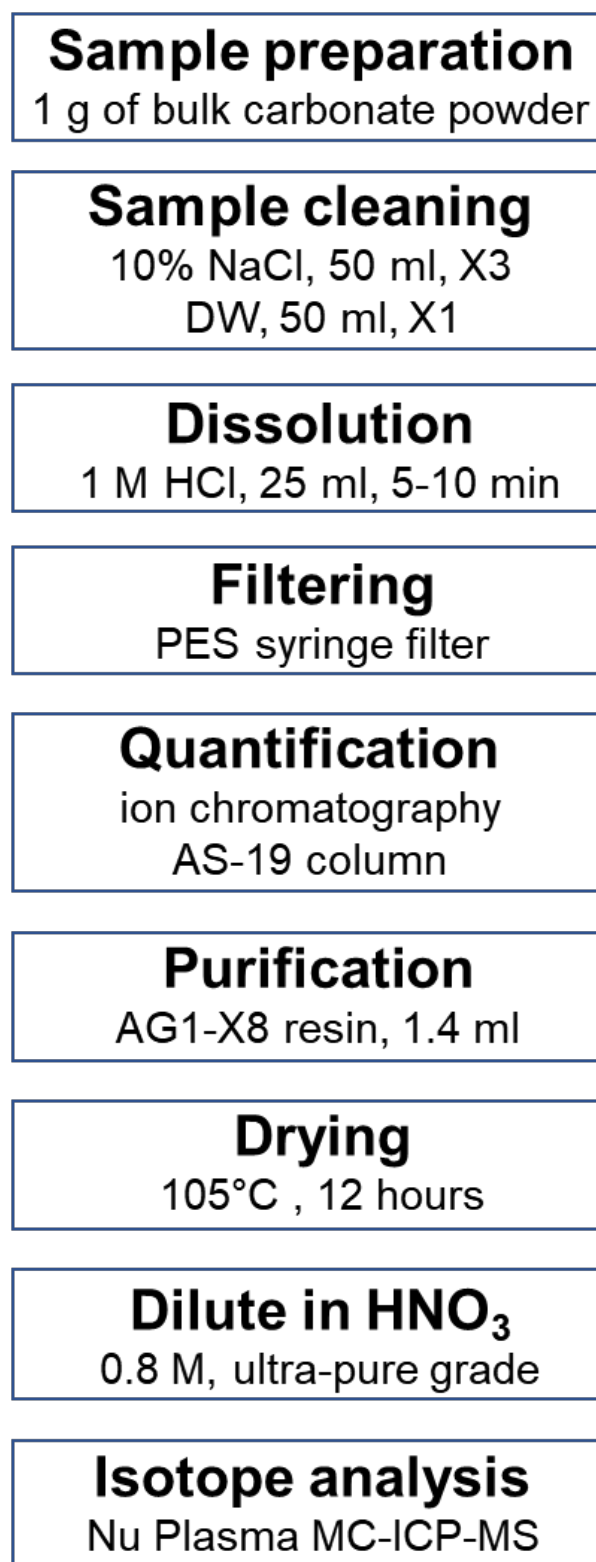**Isotope analysis**
Nu Plasma MC-ICP-MS

Figure 4.2. Flow chart of mesoscale CAS extraction protocol described in this Chapter.

4.2.2 Microscale CAS extraction method

To confirm the reliability and test for pyrite oxidation, the isotopic analysis result from the mesoscale method was compared with the data from the traditional method. However. traditional method cannot completely exclude the influence of pyrite oxidation, and it needs a comparison group that can completely rule out pyrite oxidation to examine effect of pyrite oxidation. As microscale experiments can reliably exclude pyrite oxidation, the comparison of microscale and mesoscale experiments can provide further insights for experimental pyrite oxidation and CAS extraction method. However, it is also challenging for a microscale CAS experiment to obtain a primary seawater signal because sulfate isotope values can also be altered by early diagenesis and there is significant heterogeneity in CAS isotope values within the same slab (Present et al., 2015; 2019). Nevertheless, microscale experiment can verify that the isotopic values are within the expected range when pyrite oxidation is excluded and helps to focus on other factors that may affect the isotopic composition of CAS. The microscale experiment was performed on four grainstone samples from the Duwibong Formation (D41, D36, D21, D9). Of these, one sample was specifically selected to further investigate the effects of pyrite oxidation (D9). This sample include the extraction of the pyrite grain along with the surrounding textures. For the other three samples, pyrite free area of the slab was selected for drilling.

The microscale experiment method is from Present et al. (2015). From the four carbonate slabs in the Duwibong Formation, approximately 10 mg of powder was drilled for each sample. For the extraction of the carbonate texture, a carving drill with a 0.3 mm tip drill bit was used. The extracted powder was then washed three times with 10% NaCl solution to eliminate external sulfate and dissolved in 1 ml of 0.5 M hydrochloric acid. Concentration of sulfate in the sample was measured by IC. Samples were purified and sulfate isotope compositions were analyzed by MC-ICP-MS. The quantification, purification and isotope analysis process are identical to mesoscale extraction method. The photographs of the thin sections and slabs used in the microscale extraction are shown in Figure 4.5. The results of the microscale experiment are presented in Table 4.2.

4.3 Results and discussions

4.3.1 Mesoscale experimental results for Svalbard samples

The CAS contents of limestone samples are presented in Table 4.1. In the limestone samples, the CAS contents ranged from 571 to 670 ppm, with an average content of 647 ppm for the 5 times repeated mesoscale experiment, with a standard deviation of 43 ppm. The CAS concentration obtained with the traditional extraction method was lower than that achieved with mesoscale protocol. The experiment result with different dissolution times, the CAS contents ranged from 550 to 670 ppm, and no discernible trend was observed between dissolution time and CAS contents. This suggests that a 5-minute dissolution time is sufficient for complete carbonate dissolution. CAS contents in pyrite-mixed samples range from 607 to 742 ppm, representing a slightly higher concentration.

The CAS contents in dolostone samples are presented in Table 4.1. In the dolostone samples, the CAS contents ranged from 1188 to 1544 ppm, with an average content of 1318 ppm. The standard deviation of CAS contents was 43 ppm. Compared to the traditional method, the mesoscale extraction method shows much higher CAS concentration. For both limestone and dolostone samples, CAS contents measured in mesoscale method is higher than traditional method. Possible hypothesis for the difference in CAS contents between these two methods are losses of barium sulfate during recovery and weighing, heterogeneity of the carbonate samples, and precipitation of only a fraction of the sulfate ions as barium sulfate. However, it is hard to conclude which of these three is the main cause. For the samples with different dissolution times, the CAS contents ranged from 1225 to 1352 ppm, and no discernible trend was observed between dissolution time and CAS contents. Pyrite mixed samples show CAS contents between 1498 to 1628 ppm, a slightly higher concentration than results of carbonate samples.

The CAS isotope values of limestone samples for different protocols and conditions are presented in Table 4.1 and Figure 4.3. Average value of CAS isotope with traditional method ($\delta^{34}S_{trd}$) for Svalbard limestone samples is 15.4‰, with a standard deviation of 0.3‰. Analyzing the samples 5 times, the average value of CAS isotope with meso-scale method ($\delta^{34}S_{ms}$) is determined to be 15.5‰, with a

standard deviation of 0.3‰, indicating similar analytic results between two extraction methods. The $\delta^{34}S_{ms}$ values for limestone samples ranged from 15.0 to 15.9‰, indicating that the reproducibility of this method is within 0.9‰. For the samples with different dissolution times, the CAS isotope values ranged from 14.9 to 15.6‰, and no specific trend was observed based on the dissolution time. For $\delta^{34}S_{ms}$ values in pyrite mixed samples, two of them show lower value than $\delta^{34}S_{ms}$ values in limestone, indicating experimental pyrite oxidation.

The CAS isotope values of dolostone samples are shown in Figure 4.4 and Table 4.1. $\delta^{34}S_{trd}$ for Svalbard dolostone samples is 14.4‰, with a standard deviation of 0.5‰. Analyzing the samples 5 times, the average value of $\delta^{34}S_{ms}$ for dolostone samples was determined to be 14.2‰, with a standard deviation of 0.3‰. The $\delta^{34}S_{ms}$ values for dolostone samples ranged from 13.7 to 14.6‰, indicating the reproducibility $\delta^{34}S_{ms}$ was within 0.9‰. For $\delta^{34}S_{ms}$ in pyrite mixed samples, one of the results shows light isotope composition, representing experimental pyrite oxidation. Including the limestone experiment, three out of six experiment showed relatively light values.

The mesoscale experiment results from the Svalbard samples indicate that reducing the experimental volume, lowering the concentration of the acid, and reducing the dissolution time did not lead to significant differences in CAS isotope values compare to the traditional method, and the reproducibility was also similar. Therefore, it seems that mesoscale method can measure $\delta^{34}S_{CAS}$ in the carbonate with low CAS and pyrite contents. However, if pyrite was added to sample, heterogeneous pyrite oxidation is observed in mesoscale method, which possibly alter the CAS isotope values.

Table 4.1. Experimental results of samples after different extraction methods. Pyrite contents of limestone and dolostone samples were measured by weighing Ag_2S precipitation after the pyrite extraction experiment, but the amount of Ag_2S precipitation in dolostone samples is too low to measure pyrite contents. Pyrite contents for pyrite mixed samples are (weight of pyrite in carbonate samples + added pyrite) / (weight of carbonate + added pyrite).

sample	experimental method	sulfate (ppm)	$\delta^{34}S_{CAS}$	pyrite (ppm)
sb-lime-1	protocol	697	15.9	6
sb-lime-2	protocol	679	15.2	6
sb-lime-3	protocol	616	15.5	6
sb-lime-4	protocol	661	15.8	6
sb-lime-5	protocol	670	15.0	6
sb-lime-15min	dissolve for 15 min	670	15.4	6
sb-lime-30min	dissolve for 30 min	580	15.6	6
sb-lime-1h	dissolve for 1 hour	552	14.9	6
sb-lime-2h	dissolve for 2 hour	571	15.2	6
sb-lime-py1	mixed with 1% pyrite	607	15.0	10226
sb-lime-py2	mixed with 1% pyrite	687	10.5	9916
sb-lime-py3	mixed with 1% pyrite	742	13.0	10102
sb-lime-bu1	Wotte et al. (2012)	477	15.7	6
sb-lime-bu2	Wotte et al. (2012)	576	15.6	6
sb-lime-bu3	Wotte et al. (2012)	583	14.9	6
sb-dolo-1	protocol	1544	14.6	
sb-dolo-2	protocol	1188	14.1	
sb-dolo-3	protocol	1354	14.4	
sb-dolo-4	protocol	1453	13.7	
sb-dolo-5	protocol	1436	14.4	
sb-dolo-15min	dissolve for 15 min	1352	14.9	
sb-dolo-30min	dissolve for 30 min	1263	14.3	
sb-dolo-1h	dissolve for 1 hour	1348	14.7	
sb-dolo-2h	dissolve for 2 hour	1225	14.5	
sb-dolo-py1	mixed with 1% pyrite	1498	15.1	10198
sb-dolo-py2	mixed with 1% pyrite	1628	13.0	10023
sb-dolo-py3	mixed with 1% pyrite	1527	14.2	10311
sb-dolo-bu1	Wotte et al. (2012)	751	13.9	
sb-dolo-bu2	Wotte et al. (2012)	921	14.1	
sb-dolo-bu3	Wotte et al. (2012)	883	15.1	

Figure 4.3. Isotopic analysis results of Svalbard limestone samples for different extraction conditions and methods. Green dots indicate replicate results of the mesoscale protocol. Blue shaded area indicates within $\pm 1\sigma$ range of $\delta^{34}S_{ms}$. Orange dots represent result of different dissolution time in mesoscale experiment. Blue dots indicate result from the pyrite mixed samples. Yellow dots show isotope data of traditional method. Green shaded area shows within $\pm 1\sigma$ range of $\delta^{34}S_{trd}$.
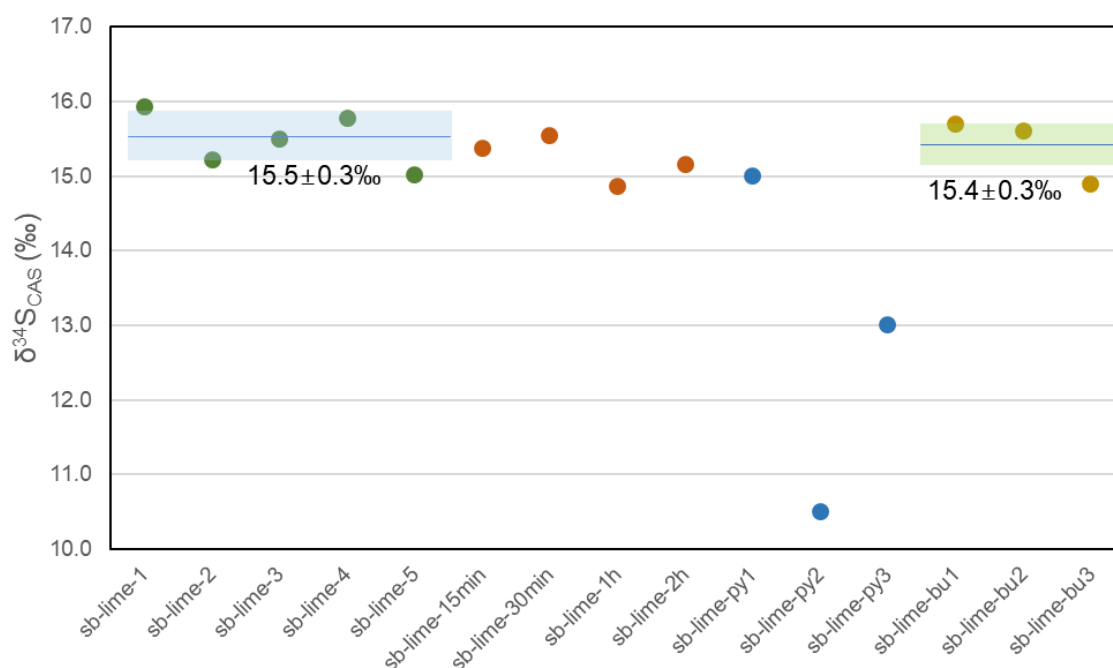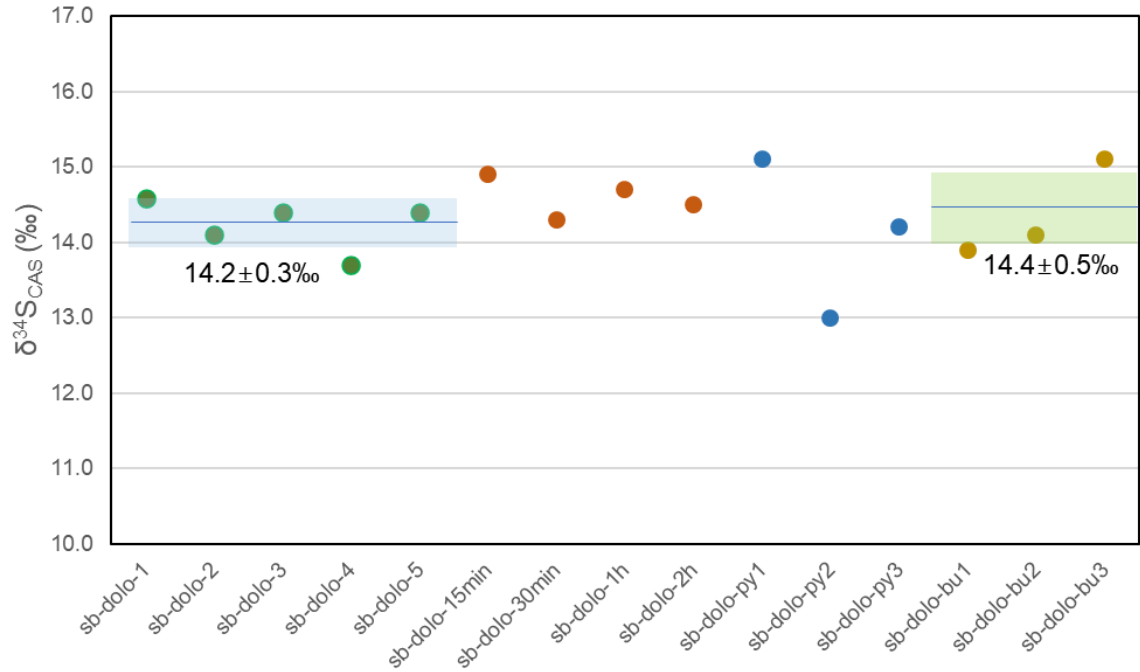
Figure 4.4. Isotopic analysis results of Svalbard dolostone samples for different extraction conditions and methods. Green dots indicate replicate results of the mesoscale protocol. Blue shaded area indicates within ±1σ range of $\delta^{34}S_{ms}$. Orange dots represent the result of different dissolution time in mesoscale experiment. Blue dots indicate result from the pyrite mixed samples. Yellow dots show isotope data of traditional method and green shaded area show ±1σ range of $\delta^{34}S_{trd}$.

4.4.2 Mesoscale experiment result for Joseon Supergroup samples

To evaluate the reliability of the protocol in samples with high pyrite contents, it is necessary to perform the mesoscale CAS extraction method on the Joseon Supergroup samples. Given the lower CAS and higher pyrite contents in these samples, pyrite oxidation could have significantly affected the results using the traditional extraction protocol for Joseon Supergroup samples (Marenco et al., 2008; Wotte et al., 2012). If the resulting $\delta^{34}S_{ms}$ for the Joseon Supergroup shows a heavier isotopic signature compared to the $\delta^{34}S_{trd}$, it would indicate that less pyrite oxidation occurred during the mesoscale extraction process. This comparison would provide insights into the reliability of the mesoscale extraction method in preserving the original CAS isotopic values in samples with higher pyrite content.

The CAS isotope values obtained by the mesoscale method and the traditional method for the Joseon Supergroup samples show the significant difference (Table 4.2). For Yeongheung Formation samples, $\delta^{34}S_{ms}$ values show the expected isotopic values during the Middle Ordovician, but some samples show different results depending on the experimental method. For Taebaek samples, $\delta^{34}S_{ms}$ values range from -8 to 4‰, which are much lighter than the Ordovician $\delta^{34}S_{CAS}$ from other regions (Figure 4.1), suggesting the possible influence of experimental pyrite oxidation. It is important to note that the $\delta^{34}S_{ms}$ did not consistently show higher values compared to $\delta^{34}S_{trd}$. It appears that random pyrite oxidation may occur during the experimental process, resulting in significant scattering and the light isotopic compositions of CAS.

In conclusion, based on the experimental results obtained from Joseon Supergroup samples, preventing experimental pyrite oxidation using the mesoscale CAS extraction method proves to be challenging. The findings also suggest that avoiding oxidation by chemical methods when experimenting with bulk rock samples containing high pyrite content is difficult. Therefore, prior to conducting mesoscale experiments on bulk rock, careful consideration of the pyrite content is necessary. In cases where the pyrite content is high, it is advisable to employ microscale experiments, extracting CAS from pyrite-free areas on the carbonate slab to prevent pyrite oxidation.

Table 4.2. The analytical result of CAS isotope data with traditional method (Wotte et al., 2012), $\delta^{34}S_{CAS}$ with mesoscale method (this study), $\delta^{34}S_{CAS}$ for the microscale method (Present et al., 2015), concentration of precipitated sulfate, pyrite, and ratio of pyrite sulfur to sulfate sulfur in the Joseon Supergroup samples.

Sample	$\delta^{34}S_{CAS}$ (‰)			contents (ppm)		pyrite sulfur / sulfate sulfur	sample location
	traditional method	mesoscale method	microscale method	Precipitated sulfate	pyrite		
NG80	30.2	27.6		191	1004	8.4	
NG76	32.8	33.2		86	91	1.7	
NG64	33.3	32		3	11	5.9	
NG59	27.8	27.2		112	271	3.9	Yeongheung
NG50	27.7	31.1		56	112	3.2	
NG43	28.9	28.1		27	155	9.2	
NG40	23.7	27.5		20	234	18.7	
NG34	40.3	33.2		18	113	10.0	
D41	3.5	4.4	-5.4	15	158	16.9	
D36	8.2	-4.7	14.2	34	1512	71.2	
D21	3.2	-8.7	-10.9	31	270	13.9	Duwibong
D15	-1.3	7.4		45	921	32.7	
D9	-4.2	3.7	-7.8	48	1105	36.8	
D3	22.4	0.7		21	264	20.1	
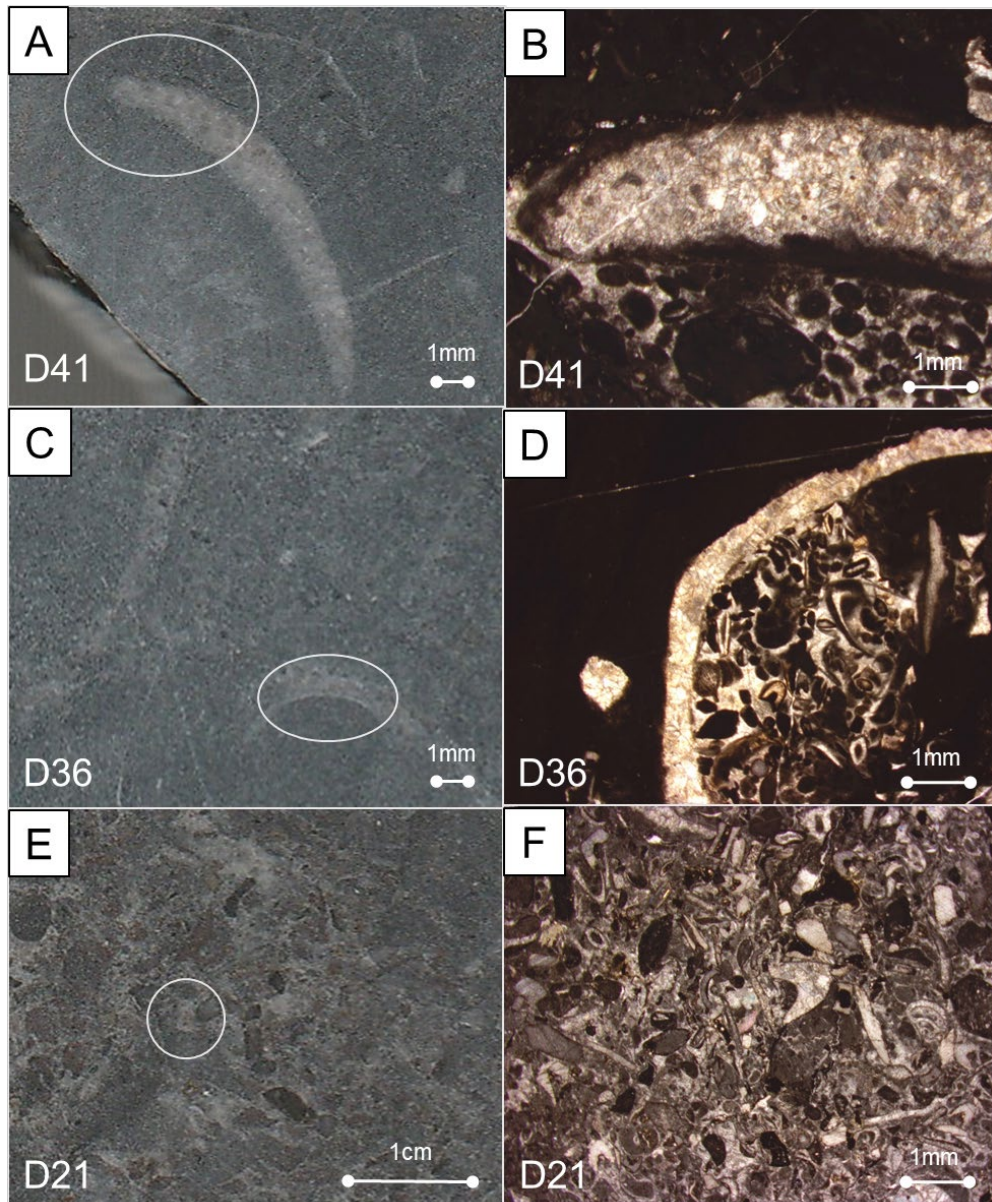
Figure 4.5. Photograph of polished slabs and this sections for microscale CAS extraction in the Duwibong Formation. White circles indicate drilled area for CAS analysis. The thin section photographs (figures B, D, and F) were taken near the drilled area. No pyrite grains are seen in the slabs and thin sections around extracted area, indicating extracted powder cannot be influenced by pyrite oxidation. In order to obtain sufficient powder to experiment, sample drilling was also conducted in areas other than those shown.

126

4.4.3 Microscale experiment result and its implication for CAS extraction

It is confirmed that the mesoscale protocol cannot prevent pyrite oxidation in samples with high pyrite contents. Consequently, conducting microscale experiments directly on the carbonate texture, specifically in pyrite-free areas on the slab, becomes necessary to verify experimental results without pyrite oxidation. The primary goal of these microscale experiments is to obtain CAS isotope data from the pyrite free area and compare them with mesoscale and traditional method data in the same samples.

The results of the microscale experiment are presented in Table 4.2. The experimental results in some samples (D41, D21, D9) showed that a lighter isotopic composition of CAS than $\delta^{34}S_{ms}$ and $\delta^{34}S_{trd}$. These isotope compositions are too light to be expected in Ordovician seawater. D9 sample contain pyrite and might be influenced by pyrite oxidation but D21 and D41 samples did not contain pyrite, suggesting that the isotopic values may be influenced by another factor. Previous studies of CAS extraction suggest that the isotopic values of CAS can be influenced by early diagenetic processes, resulting in deviations up to 15‰ from seawater values (Present et al., 2015; 2019; Richardson et al., 2019; 2021). Isotope values of CAS can be heavier or lighter when affected by authigenic carbonate. Lighter sulfate isotopic compositions of authigenic carbonate than seawater was interpreted as the result of sulfide oxidation in pore water and heavier isotope compositions as progressive fractionation in the closed pore water system (Present et al., 2015; 2019; Richardson et al., 2019; Ma et al., 2021). Therefore, the light isotopic compositions in the microscale experiment are due to sulfide oxidation during early diagenesis. Thin sections from the Joseon Supergroup showing authigenic carbonate and recrystallized texture (Figure 4.5) supports this explanation. However, the D36 sample shows isotopic values expected for the Ordovician, indicating that the effect of authigenic carbonate on the CAS isotope values also occurs randomly.

The microscale CAS extraction results from the Taebaek samples show that considerable caution is required in CAS extraction experiments. Even if avoiding pyrite with microscale experiments, isotope values could be distinct from seawater signal due to influence of authigenic carbonate. In addition,

authigenic carbonate may be more challenging interference than pyrite in analyzing seawater sulfate signal because authigenic carbonate is harder to recognized than pyrite. In order to overcome these issues, microscale CAS extraction on well-preserved fossils is the best experimental method to obtain the primary seawater sulfate signal. However, well-preserved fossils are hard to find, thus it is difficult to create high-resolution timeseries. Also, vital effect between the fossil species should be considered to obtain marine signal. Another method is to dilute diagenetic effects with bulk rock experiment. In a bulk carbonate, different carbonate textures are mixed together, which allows for dilution of diagenetic influences, thereby preserving the signal of the original seawater to some extent (Strauss, 1999; Hurtgen et al., 2002; Kah et al., 2004). Indeed, a recent study of the early diagenesis effect on the sulfur isotopic composition of CAS, using both experimental data and numerical modeling, suggests that the $\delta^{34}S_{CAS}$ of bulk carbonate does not differ by more than 4‰ from that of the overlying seawater sulfate (Rennie & Turchyn, 2014). Therefore, the mesoscale method can analyze to samples with lower CAS content and contribute to the recovery of a high-resolution CAS sulfur isotope record, if pyrite contents in the carbonate is low enough.

4.4 Conclusion

This chapter introduces a mesoscale bulk rock CAS extraction method for MC-ICP-MS analysis and conduct several experiments to evaluate the reliability of the protocol. Measured 5 times with the Svalbard limestone and dolostone samples, the reproducibility of the method is as good as the traditional method. The average $\delta^{34}S_{CAS}$ values obtained from the two methods are similar for both limestone and dolostone samples. Therefore, mesoscale method can measure CAS isotope composition in low CAS carbonate. The experimental results obtained from samples containing 1% pyrite in high CAS carbonate suggest that it is difficult to exclude the experimental pyrite oxidation in mesoscale extraction. The evaluation of the mesoscale CAS extraction method using carbonate samples from the Joseon Supergroup, which have low CAS and high pyrite contents, reveals significantly different CAS isotope values compare to the traditional method, suggesting pyrite oxidation in high pyrite contents carbonate. Microscale CAS experiment in the Duwibong Formation samples also show light isotopic composition, indicating influence of authigenic carbonate. Nevertheless, as bulk carbonate can dilute effect of authigenic carbonate, mesoscale method can measure CAS isotope composition in carbonate with low CAS contents, if the pyrite content is low.

5. Summary of the thesis

This thesis discussed the methods for analyzing the CAS isotope value in bulk carbonate, the regional sulfur cycle and depositional environment during the Ordovician, and the global sulfur cycle during the late Paleozoic, contributing to the understanding of the biogeochemical carbon and sulfur cycle in ancient Earth. Here, this chapter summarize the conclusions described in Chapters 2, 3, and 4 and outline the future directions of biogeochemical studies.

The Chapter 2 focus on different patterns of carbon and sulfur isotope values observed in the Middle Ordovician strata of Yeongwol and Taebaek. Measuring additional carbon isotope data and updating conodont biozone, it is confirmed that a negative carbon isotope excursion in the Jigunsan Formation is not observed in any other region including Yeongwol. This distinct carbon isotope pattern is interpreted as enhanced organic matter decomposition by sulfate reducers and benthic flux input due to reduced sedimentation rates in the restricted environment. The pyrite sulfur isotope difference between Taebaek and Yeongwol is interpreted as a result of the depositional environment in these two areas. This study highlight that the interpretation of isotopic curve must consider the depositional environment change. This conclusion is also related to the interpretation of the Gzhelian CAS isotope curve of Svalbard in Chapter 3. The extremely heavy CAS isotope compositions in the Gzhelian interval provides important implications for the relationship between depositional environment and isotopic patterns. If more reliable age control can be achieved in the Yeongwol region, future research could describe the global carbon cycle using data from the Yeongwol, which maintains a relatively stable environment.

Chapter 3 interpreted changes in the global sulfur cycle during the period of continental collision and climate change. High-resolution analysis of Early Permian CAS isotope data revealed an increasing pattern of sulfate isotope values coinciding with the closure of the Ural Seaway and the glacial event.

This increasing pattern can be explained by increased burial of pyrite due to glaciation and increased dissolution of evaporite due to the P1 glaciation and Ural Seaway closure. This study highlights the relationship between geological events affecting the global environment and biogeochemical cycles and indicates that consideration of different geological events is important for studying the global biogeochemical cycle in the ancient Earth.

However, this study is conducted using bulk carbonate from a single region. Since bulk CAS data can be influenced by the depositional environment, it is necessary to obtain CAS data from different regions to verify whether the observed increasing trend in the Early Permian is a global signal. Furthermore, this study only reported the occurrence of excursions without the decay of the excursion, and future study would investigate the decay of the excursion during the Middle Permian.

In Chapter 4, various experiments were conducted to develop a mesoscale extraction method to obtain CAS isotopic values in samples with low CAS content without pyrite oxidation. It is concluded that mesoscale method shows similar isotopic value and reproducibility with the traditional method, suggesting that this method can measure sulfur isotope composition in low CAS carbonate. However, it is difficult to prevent pyrite oxidation with mesoscale method in high pyrite contents samples. Microscale experiment indicates that not only pyrite oxidation but also authigenic carbonate can alter the isotopic signal of CAS. However, in samples with low pyrite content, bulk carbonate is likely to provide a marine sulfate signal and the mesoscale method can be used for experiments in low CAS carbonate because influence of the authigenic carbonate is diluted in bulk rock. Although the mesoscale method cannot prevent pyrite oxidation, physical separation of pyrite to prevent oxidation could be considered and further research is needed in this area.

REFERENCES

Ahlborn, M., & Stemmerik, L. (2015). Depositional evolution of the Upper Carboniferous–Lower Permian Wordiekammen carbonate platform, Nordfjorden High, central Spitsbergen, Arctic Norway. Norwegian Journal of Geology, 95(1), 91-126.

Ainsaar, L., Kaljo, D., Martma, T., Meidla, T., Männik, P., Nõlvak, J., & Tinn, O. (2010). Middle and Upper Ordovician carbon isotope chemostratigraphy in Baltoscandia: a correlation standard and clues to environmental history. Palaeogeography, Palaeoclimatology, Palaeoecology, 294(3-4), 189-201.

Albanesi, G. L., Bergström, S. M., Schmitz, B., Serra, F., Feltes, N. A., Voldman, G. G., & Ortega, G. (2013). Darriwilian (Middle Ordovician) $\delta^{13}C_{carb}$ chemostratigraphy in the Precordillera of Argentina: Documentation of the middle Darriwilian Isotope Carbon Excursion (MDICE) and its use for intercontinental correlation. Palaeogeography, Palaeoclimatology, Palaeoecology, 389, 48-63.

Algeo, T. J., Luo, G. M., Song, H. Y., Lyons, T. W., & Canfield, D. E. (2015). Reconstruction of secular variation in seawater sulfate concentrations. Biogeosciences, 12(7), 2131-2151.

Aller, R. C., Madrid, V., Chistoserdov, A., Aller, J. Y., & Heilbrun, C. (2010). Unsteady diagenetic processes and sulfur biogeochemistry in tropical deltaic muds: implications for oceanic isotope cycles and the sedimentary record. Geochimica et Cosmochimica Acta, 74(16), 4671-4692.

Anderson, R. F., Sachs, J. P., Fleisher, M. Q., Allen, K. A., Yu, J., Koutavas, A., & Jaccard, S. L. (2019). Deep-sea oxygen depletion and ocean carbon sequestration during the last ice age. *Global biogeochemical cycles*, *33*(3), 301-317.

Bang, S., & Lee, Y. I. (2020). Darriwilian carbon isotope stratigraphy in the Taebaeksan Basin, Korea

and its implications for Middle Ordovician paleoceanography. Palaeogeography, Palaeoclimatology, Palaeoecology, 541, 109534.

Bang, S. H., (2023). Development and application of analytical methods for boron isotope proxy: paleoceanographic interpretation of the Paleozoic can Cenozoic carbonates. Ph.D dissertation, Seoul National University, Seoul, South Korea.

Ben-YaaKov, S. (1973). pH buffering of pore water of recent anoxic marine sediments. Limnol. Oceanogr. 18, 86–94

Bergström, S. M., Eriksson, M. E., & Ahlberg, P. (2020). Ordovician δ13C chemostratigraphy: A global review of major excursions and their ties to graptolite and conodont biostratigraphy. *Stratigraphy & Timescales*, *5*, 319-351.

Berner, R. A. (1980). Early Diagenesis: A Theoretical Approach, Princeton Univ.Press,

Berner, R. A. (1982). Burial of organic carbon and pyrite sulfur in the modern ocean: its geochemical and environmental significance. *Am. J. Sci.;(United States)*, *282*.

Berner, R. A. (1984). Sedimentary pyrite formation: an update. *Geochimica et cosmochimica Acta*, *48*(4), 605-615.

Berner, R. A. (1990). Atmospheric carbon dioxide levels over Phanerozoic time. *Science*, *249*(4975), 1382-1386.

Berner, R. A., & Raiswell, R. (1983). Burial of organic carbon and pyrite sulfur in sediments over Phanerozoic time: a new theory. Geochimica et Cosmochimica Acta, 47(5), 855-862.

Blakey, R. C., Fielding, C. R., Frank, T. D., & Isbell, J. L. (2008). Gondwana paleogeography from assembly to breakup—A 500 my odyssey. Geological Society of America Special Papers, 441, 1-28.

Blomeier, D., Dustira, A., Forke, H., & Scheibner, C. (2011). Environmental change in the Early Permian of NE Svalbard: from a warm-water carbonate platform (Gipshuken Formation) to a temperate,

mixed siliciclastic-carbonate ramp (Kapp Starostin Formation). Facies, 57(3), 493-523.

Bohacs, K. M., Grabowski, G. J., Carroll, A. R., Mankiewicz, P. J., Miskell-Gerhardt, K. J., Schwalbach, J. R., ... & Simo, J. T. (2005). Production, destruction, and dilution—the many paths to source-rock development.

Bottrell, S. H., & Newton, R. J. (2006). Reconstruction of changes in global sulfur cycling from marine sulfate isotopes. Earth-Science Reviews, 75(1-4), 59-83.

Bradley, A. S., Leavitt, W. D., Schmidt, M., Knoll, A. H., Girguis, P. R., & Johnston, D. T. (2016). Patterns of sulfur isotope fractionation during microbial sulfate reduction. *Geobiology*, *14*(1), 91-101.

Brimblecombe, P., Hammer, C., Rodhe, H., Ryaboshapko, A., & Boutron, C. F. (1989). Human influence on the sulphur cycle. *Evolution of the global biogeochemical sulphur cycle*, 77-121.

Buggisch, W., Joachimski, M., Lutzner, H., Thiedig, F., & Huneke, H. (2001). Conodont Stratigraphy of the Carboniferous and Permian Strata from Broggerhalvoya and the Billefjorden Trough. Geologisches Jahrbuch Reihe B, 637-692.

Buggisch, W., Keller, M., & Lehnert, O. (2003). Carbon isotope record of Late Cambrian to Early Ordovician carbonates of the Argentine Precordillera. Palaeogeography, Palaeoclimatology, Palaeoecology, 195(3-4), 357-373.

Burke, A., Present, T. M., Paris, G., Rae, E. C., Sandilands, B. H., Gaillardet, J., ... & Adkins, J. F. (2018). Sulfur isotopes in rivers: Insights into global weathering budgets, pyrite oxidation, and the modern sulfur cycle. *Earth and Planetary Science Letters*, *496*, 168-177.

Burton, H. R., & Barker, R. J. (1979). Sulfur chemistry and microbiological fractionation of sulfur isotopes in a saline Antarctic lake. Geomicrobiology Journal, 1(4), 329-340.

Byun, U. H., Lee, H. S., & Kwon, Y. K. (2018). Sequence stratigraphy in the middle Ordovician shale successions, mid-east Korea: Stratigraphic variations and preservation potential of organic matter

within a sequence stratigraphic framework. Journal of Asian Earth Sciences, 152, 116-131.

Canfield, D. E. (1989). Sulfate reduction and oxic respiration in marine sediments: implications for organic carbon preservation in euxinic environments. *Deep Sea Research Part A. Oceanographic Research Papers*, *36*(1), 121-138.

Canfield, D. E. (2001). Isotope fractionation by natural populations of sulfate-reducing bacteria. Geochimica et Cosmochimica Acta, 65(7), 1117-1124.

Canfield, D. E. (2004). The evolution of the Earth surface sulfur reservoir. *American Journal of Science*, *304*(10), 839-861.

Canfield, D. E., & Teske, A. (1996). Late Proterozoic rise in atmospheric oxygen concentration inferred from phylogenetic and sulphur-isotope studies. Nature, 382(6587), 127-132.

Canfield, D. E., & Thamdrup, B. (1996). Fate of elemental sulfur in an intertidal sediment. FEMS Microbiology Ecology, 19(2), 95-103.

Canfield, D. E., Raiswell, R., Westrich, J. T., Reaves, C. M., & Berner, R. A. (1986). The use of chromium reduction in the analysis of reduced inorganic sulfur in sediments and shales. Chemical geology, 54(1-2), 149-155.

Chang, C., Hu, W., Wang, X., Yu, H., Yang, A., Cao, J., & Yao, S. (2017). Carbon isotope stratigraphy of the lower to middle Cambrian on the eastern Yangtze Platform, South China. *Palaeogeography, Palaeoclimatology, Palaeoecology*, *479*, 90-101.

Chen, J., Montañez, I. P., Qi, Y., Shen, S., & Wang, X. (2018). Strontium and carbon isotopic evidence for decoupling of pCO2 from continental weathering at the apex of the late Paleozoic glaciation. Geology, 46(5), 395-398.

Chen, S. (1934). Fusulinidae of South China, Part 1. Palaeontologia Sinica, 4, 1-185.

Cherns, L., Wheeley, J. R., Popov, L. E., Ghobadi Pour, M., Owens, R. M., & Hemsley, A. R. (2013).

Long-period orbital climate forcing in the early Palaeozoic?. Journal of the Geological Society, 170(5), 707-710.

Cho, S. H., Lee, B. S., Lee, D. J., & Choh, S. J. (2021). The Ordovician succession of the Taebaek Group (Korea) revisited: old conodont data, new perspectives, and implications. Geosciences Journal, 25(4), 417-431.

Cho, S.H. and Choh, S.-J. (2021). Rejuvenation and establishment of a carbonate epeiric platform: Makgol Formation immediately overlying the regional unconformity. Paper presented at the 2021 Joint Conference of the Geological Science and Technology of Korea, 23–24 June, Gyeongju, South Korea.

Cho, Sehyun1, Lee, Byung-Su2, Choh, Suk-Joo (2022). As the waters cover the sea: characterization of the initial Middle Ordovician onlap onto eastern North China carbonate epeiric platform. [poster]. GCA 2022. 9-12 October, Denver, Colorado, USA.

Choh, S. J., Hong, J., Sun, N., Kwon, S. W., Park, T. Y., Woo, J., ... & Lee, D. J. (2013). Early Ordovician reefs from the Taebaek Group, Korea: constituents, types, and geological implications. Geosciences Journal, 17, 139-149.

Choi, D. K. (1998). The Yongwol Group (Cambrian-Ordovician) redefined: a proposal for the stratigraphic nomenclature of the Choson Supergroup. Geosciences Journal, 2(4), 220-234.

Choi, D. K., & Jeong, K. W. (1990). Discovery of conulariid from the Yeongheung Formation (Ordovician), Korea. J. Geol. Korea, 26(5), 497-499.

Choi, D. K., Chough, S. K., Kwon, Y. K., Lee, S. B., Woo, J., Kang, I., & Lee, D. J. (2004). Taebaek group (Cambrian-Ordovician) in the Seokgaejae section, Taebaeksan Basin: a refined lower Paleozoic stratigraphy in Korea. Geosciences Journal, 8(2), 125-151.

Choi, D. K., Kim, D. H., & Sohn, J. W. (2001). Ordovician trilobite faunas and depositional history of the Taebaeksan Basin, Korea: implications for palaeogeography. Alcheringa, 25(1), 53-68.

Choi, D. K., Kim, D. H., & Sohn, J. W. (2001). Ordovician trilobite faunas and depositional history of the Taebaeksan Basin, Korea: implications for palaeogeography. *Alcheringa*, *25*(1), 53-68.

Choi, D. K., Lee, J. G., LEE, S. B., PARK, T. Y. S., & Hong, P. S. (2016). Trilobite biostratigraphy of the lower Paleozoic (Cambrian–Ordovician) Joseon Supergroup, Taebaeksan Basin, Korea. *Acta Geologica Sinica-English Edition*, *90*(6), 1976-1999.

Choi, D.K. (2011). A new view on the Early Paleozoic paleogeography and paleoenvironments of the Taebaeksan basin, Korea. 고생물학회지, 27(1), 1-11.

Choi, S. J., & Woo, K. S. (1993). Depositional environment of the Ordovician Yeongheung Formation near Machari area, Yeongweol, Kangweondo, Korea. 지질학회지, 29(4), 375-386.

Chwieduk, E. (2013). Palaeogeografical and palaeoecological significance of the Uppermost Carboniferous and Permian rugose corals of Spitsbergen. Wydawnictwo Naukowe UAM, Poznań.

Claypool, G. E., Holser, W. T., Kaplan, I. R., Sakai, H., & Zak, I. (1980). The age curves of sulfur and oxygen isotopes in marine sulfate and their mutual interpretation. Chemical geology, 28, 199-260.

Cleal, C. J., & Thomas, B. A. (2005). Palaeozoic tropical rainforests and their effect on global climates: is the past the key to the present? Geobiology, 3(1), 13-31.

Cooper, J. D., Miller, R. H., & Patterson, J. (1990). A trip through time: principles of historical geology (No. 551.7 COO).

Cui, H., Kaufman, A. J., Xiao, S., Zhou, C., & Liu, X. M. (2017). Was the Ediacaran Shuram Excursion a globally synchronized early diagenetic event? Insights from methane-derived authigenic carbonates in the uppermost Doushantuo Formation, South China. Chemical Geology, 450, 59-80.

Cutbill, J. L., & Challinor, A. (1965). Revision of the stratigraphical scheme for the Carboniferous and Permian rocks of Spitsbergen and Bjørnøya. Geological Magazine, 102(5), 418-439.

Dallmann, W. K., (1999), Lithostratigraphic lexicon of Svalbard. Upper Palaeozoic to Quaternary bedrock. Review and recommendations for nomenclature use: Tromsø, Norwegian Polar Institute, 318 p.

Das, A., Chung, C. H., You, C. F., & Shen, M. L. (2012). Application of an improved ion exchange technique for the measurement of $\delta^{34}S$ values from microgram quantities of sulfur by MC-ICPMS. Journal of Analytical Atomic Spectrometry, 27(12), 2088-2093.

Davydov, V. I. (2018). Precaspian Isthmus emergence triggered the Early Sakmarian glaciation: Evidence from the Lower Permian of the Urals, Russia. Palaeogeography, Palaeoclimatology, Palaeoecology, 511, 403-418

Davydov, V. I., & Cózar, P. (2019). The formation of the Alleghenian Isthmus triggered the Bashkirian glaciation: Constraints from warm-water benthic foraminifera. *Palaeogeography, Palaeoclimatology, Palaeoecology*, *531*, 108403.

Ding, W., Dong, L., Sun, Y., Ma, H., Xu, Y., Yang, R., & Shen, B. (2019). Early animal evolution and highly oxygenated seafloor niches hosted by microbial mats. *Scientific Reports*, *9*(1), 13628.

Ding, W., Nie, T., Peng, Y., Sun, Y., Xue, J., & Shen, B. (2021). Validating the deep time carbonate carbon isotope records: effect of benthic flux on seafloor carbonate. Acta Geochimica, 40(3), 271-286.

Ding, X., Liu, G., Zha, M., Huang, Z., Gao, C., Lu, X., & Liuzhuang, X. (2015). Relationship between total organic carbon content and sedimentation rate in ancient lacustrine sediments, a case study of Erlian basin, northern China. *Journal of Geochemical Exploration*, *149*, 22-29.

Dons, C. E. (1983). Facies and paleocurrent analysis of the Nordenskiöldbreen Formation (Upper Carboniferous-Lower Permian), central Spitsbergen. Unpublished Cand. Real. thesis, University of Oslo, Oslo, Norway.

Dunbar, C. O., Skinner, J. W., (1931). New fusulinid genera from the Permian of west Texas. American

Journal of Science. 5-22(129): 252-268.

Edwards, C. T., & Saltzman, M. R. (2014). Carbon isotope ($\delta^{13}C_{carb}$) stratigraphy of the Lower–Middle Ordovician (Tremadocian–Darriwilian) in the Great Basin, western United States: implications for global correlation. Palaeogeography, Palaeoclimatology, Palaeoecology, 399, 1-20.

Edwards, C. T., & Saltzman, M. R. (2016). Paired carbon isotopic analysis of Ordovician bulk carbonate (δ13Ccarb) and organic matter (δ13Corg) spanning the Great Ordovician Biodiversification Event. *Palaeogeography, Palaeoclimatology, Palaeoecology*, *458*, 102-117.

Edwards, C. T., Fike, D. A., Saltzman, M. R., Lu, W., & Lu, Z. (2018). Evidence for local and global redox conditions at an Early Ordovician (Tremadocian) mass extinction. *Earth and Planetary Science Letters*, *481*, 125-135.

Edwards, C. T., Saltzman, M. R., Royer, D. L., & Fike, D. A. (2017). Oxygenation as a driver of the Great Ordovician Biodiversification Event. Nature Geoscience, 10(12), 925-929.

Fielding, C.R., Frank, T.D., Birgenheier, L.P., Rygel, M.C., Jones, A.T., Roberts, J., (2008a). Alternating glacial and non-glacial intervals characterize the late Paleozoic Ice Age: stratigraphic evidence from eastern Australia. Journal of the Geological Society of London 165, 129–140.

Fielding, C.R., Frank, T.D., Isbell, J.L., (2008b). The late Paleozoic ice age—a review of current understanding and synthesis of global climate patterns. In: Fielding, C.R., Frank, T.D., Isbell, J.L. (Eds.), Resolving the Late Paleozoic Ice Age in Time and Space: Geological Society of America Special Paper, 441, pp. 343–354.

Fike, D. A., Bradley, A. S., & Rose, C. V. (2015). Rethinking the ancient sulfur cycle. Annual Review of Earth and Planetary Sciences, 43, 593-622.

Frank, T. D., Birgenheier, L. P., Montañez, I. P., Fielding, C. R., Rygel, M. C., & Isbell, J. L. (2008). Late Paleozoic climate dynamics revealed by comparison of ice-proximal stratigraphic and ice-distal

isotopic records. Geological Society of America Special Papers, 441, 331-342.

Fry, B., Ruf, W., Gest, H., & Hayes, J. M. (1988). Sulfur isotope effects associated with oxidation of sulfide by O_2 in aqueous solution. Chemical Geology: Isotope Geoscience section, 73(3), 205-210.

Garrels, R. M., & Lerman, A. (1981). Phanerozoic cycles of sedimentary carbon and sulfur. Proceedings of the National Academy of Sciences, 78(8), 4652-4656.

Gill, B. C., Lyons, T. W., Young, S. A., Kump, L. R., Knoll, A. H., & Saltzman, M. R. (2011). Geochemical evidence for widespread euxinia in the Later Cambrian Ocean. *Nature*, *469*(7328), 80-83

Given, R. K., & Lohmann, K. C. (1986). Isotopic evidence for the early meteoric diagenesis of the reef facies, Permian Reef Complex of West Texas and New Mexico. Journal of Sedimentary Research, 56(2), 183-193.

Goddéris, Y., Donnadieu, Y., Carretier, S., Aretz, M., Dera, G., Macouin, M., & Regard, V. (2017). Onset and ending of the late Palaeozoic ice age triggered by tectonically paced rock weathering. Nature Geoscience, 10(5), 382-386.

Grader, G. W., Isaacson, P. E., Díaz-Martínez, E., & Pope, M. C. (2008). Pennsylvanian and Permian sequences in Bolivia: Direct responses to Gondwana glaciation. *The Late Paleozoic Gondwanan ice age: timing, extent, duration and stratigraphic records. Geological Society of America, Special Paper*, *441*, 143-159.

Gradstein, F.M., Ogg, J.G., Schmitz, M., Ogg, G., (2020). Geologic Time Scale 2020, 2nd ed. Elsevier.

Grossman, E. L., Yancey, T. E., Jones, T. E., Bruckschen, P., Chuvashov, B., Mazzullo, S. J., & Mii, H. S. (2008). Glaciation, aridification, and carbon sequestration in the Permo-Carboniferous: the isotopic record from low latitudes. Palaeogeography, Palaeoclimatology, Palaeoecology, 268(3-4), 222-233.

Guo, Q., Strauss, H., Kaufman, A. J., Schröder, S., Gutzmer, J., Wing, B., & Farquhar, J. (2009). Reconstructing Earth's surface oxidation across the Archean-Proterozoic transition. Geology, 37(5),

399-402.

Habicht, K. S., & Canfield, D. E. (1997). Sulfur isotope fractionation during bacterial sulfate reduction in organic-rich sediments. Geochimica et Cosmochimica Acta, 61(24), 5351-5361.

Habicht, K. S., Canfield, D. E., & Rethmeier, J. (1998). Sulfur isotope fractionation during bacterial reduction and disproportionation of thiosulfate and sulfite. Geochimica et Cosmochimica Acta, 62(15), 2585-2595.

Habicht, K. S., Gade, M., Thamdrup, B., Berg, P., & Canfield, D. E. (2002). Calibration of sulfate levels in the Archean Ocean. Science, 298(5602), 2372-2374.

Halevy, I., Peters, S. E., & Fischer, W. W. (2012). Sulfate burial constraints on the Phanerozoic sulfur cycle. *Science*, *337*(6092), 331-334.

Han, Z., Hu, X., He, T., Newton, R. J., Jenkyns, H. C., Jamieson, R. A., & Franceschi, M. (2022). Early Jurassic long-term oceanic sulfur-cycle perturbations in the Tibetan Himalaya. Earth and Planetary Science Letters, 578, 117261.

Harland, W. B., & Geddes, I. (1997). Carboniferous-Permian history of Svalbard. Geological Society, London, Memoirs, 17(1), 310-339.

Hayes, J. M., & Waldbauer, J. R. (2006). The carbon cycle and associated redox processes through time. *Philosophical Transactions of the Royal Society B: Biological Sciences*, *361*(1470), 931-950.

He, T., Dal Corso, J., Newton, R. J., Wignall, P. B., Mills, B. J., Todaro, S., ... & Dunhill, A. M. (2020). An enormous sulfur isotope excursion indicates marine anoxia during the end-Triassic mass extinction. Science Advances, 6(37), eabb6704.

Holser, W. T. (1977). Catastrophic chemical events in the history of the ocean. Nature, 267(5610), 403-408.

Hong, J., Choh, S. J., Park, J., & Lee, D. J. (2017). Construction of the earliest stromatoporoid

framework: labechiid reefs from the Middle Ordovician of Korea. *Palaeogeography, Palaeoclimatology, Palaeoecology*, *470*, 54-62.

Hong, J., Oh, J. R., Lee, J. H., Choh, S. J., & Lee, D. J. (2018). The earliest evolutionary link of metazoan bioconstruction: Laminar stromatoporoid–bryozoan reefs from the Middle Ordovician of Korea. Palaeogeography, Palaeoclimatology, Palaeoecology, 492, 126-133.

Hong, J., Park, J., Kim, D., Cho, E., & Kim, S. M. (2022). Relatively deep subtidal microbial–lithistid sponge reef communities in Lower Ordovician rocks reveal early escalation of the Great Ordovician Biodiversification Event. *Palaeogeography, Palaeoclimatology, Palaeoecology*, *602*, 111159.

Hoogakker, B. A., Lu, Z., Umling, N., Jones, L., Zhou, X., Rickaby, R. E., ... & Galbraith, E. (2018). Glacial expansion of oxygen-depleted seawater in the eastern tropical Pacific. *Nature*, *562*(7727), 410-413.

Howard Gest, B. F., & Hayes, J. M. (1984). Isotope effects associated with the anaerobic oxidation of sulfide by the purple photosynthetic bacterium, Chromatium vinosum. FEMS Microbiology Letters, 22(3), 283-287.

Hurtgen, M. T., Arthur, M. A., Suits, N. S., & Kaufman, A. J. (2002). The sulfur isotopic composition of Neoproterozoic seawater sulfate: implications for a snowball Earth?. Earth and Planetary Science Letters, 203(1), 413-429.

Hüneke, H., Joachimski, M., Buggisch, W., & Lützner, H. (2001). Marine carbonate facies in response to climate and nutrient level: the Upper Carboniferous and Permian of Central Spitsbergen (Svalbard). Facies, 45(1), 93-135.

Immenhauser, A., Della Porta, G., Kenter, J. A., & Bahamonde, J. R. (2003). An alternative model for positive shifts in shallow-marine carbonate $\delta^{13}C$ and $\delta^{18}O$. Sedimentology, 50(5), 953-959.

Immenhauser, A., Kenter, J. A., Ganssen, G., Bahamonde, J. R., Van Vliet, A., & Saher, M. H. (2002).

Origin and significance of isotope shifts in Pennsylvanian carbonates (Asturias, NW Spain). Journal of Sedimentary Research, 72(1), 82-94.

Isbell, J. L., Miller, M. F., Wolfe, K. L., & Lenaker, P. A. (2003). Timing of late Paleozoic glaciation in Gondwana: was glaciation responsible for the development of northern hemisphere cyclothems?. Special papers-geological society of America, 5-24.

Jeon, J., Park, J., Choh, S. J., & Lee, D. J. (2017). Early labechiid stromatoporoids of the Yeongheung Formation (Middle Ordovician), Yeongwol Group, mideastern Korean Peninsula: part II. Systematic paleontology and paleogeographic implications. Geosciences Journal, 21, 331-340.

Jeong, H., & Lee, Y. I. (2000). Late Cambrian biogeography: conodont bioprovinces from Korea. Palaeogeography, Palaeoclimatology, Palaeoecology, 162(1-2), 119-136.

Jeong, H., & Lee, Y. I. (2004). Nd isotopic study of Upper Cambrian conodonts from Korea and implications for early Paleozoic paleogeography. Palaeogeography, Palaeoclimatology, Palaeoecology, 212(1-2), 77-94.

Jing, X., Zhao, Z., Fu, L., Zhang, C., Fan, R., Shen, Y., & Yang, B. (2022). Biostratigraphically-controlled Darriwilian (Middle Ordovician) $\delta^{13}C$ excursions in North China: Implications for correlation and climate change. Palaeogeography, Palaeoclimatology, Palaeoecology, 601, 111149.

Johnston, D. T., Wing, B. A., Farquhar, J., Kaufman, A. J., Strauss, H., Lyons, T. W., ... & Canfield, D. E. (2005). Active microbial sulfur disproportionation in the Mesoproterozoic. science, 310(5753), 1477-1479.

Jørgensen, B. B. (1982). Mineralization of organic matter in the sea bed—the role of sulphate reduction. Nature, 296(5858), 643-645.

Kah, L. C., Lyons, T. W., & Frank, T. D. (2004). Low marine sulphate and protracted oxygenation of the Proterozoic biosphere. *Nature*, *431*(7010), 834-838.

Kah, L. C., Thompson, C. K., Henderson, M. A., & Zhan, R. (2016). Behavior of marine sulfur in the Ordovician. Palaeogeography, Palaeoclimatology, Palaeoecology, 458, 133-153.

Kampschulte, A., & Strauss, H. (2004). The sulfur isotopic evolution of Phanerozoic seawater based on the analysis of structurally substituted sulfate in carbonates. Chemical Geology, 204(3-4), 255-286.

Kampschulte, A., Bruckschen, P., & Strauss, H. (2001). The sulphur isotopic composition of trace sulphates in Carboniferous brachiopods: implications for coeval seawater, correlation with other geochemical cycles and isotope stratigraphy. Chemical Geology, 175(1-2), 149-173.

KANO, A., LEE, D. J., CHOI, D. K., & YOO, C. M. (1994). 970. ORDOVICIAN (LLANVIRNIAN) STROMATOPOROIDS FROM THE YOUNGWOL AREA, SOUTHERN KOREA. In *Transactions and proceedings of the Paleontological Society of Japan. New series* (Vol. 1994, No. 174, pp. 449-457). PALAEONTOLOGICAL SOCIETY OF JAPAN.

Kaplan, I. R., & Rittenberg, S. C. (1964). Microbiological fractionation of sulphur isotopes. Microbiology, 34(2), 195-212.

Kemeny, P. C., Lopez, G. I., Dalleska, N. F., Torres, M., Burke, A., Bhatt, M. P., & Adkins, J. F. (2021). Sulfate sulfur isotopes and major ion chemistry reveal that pyrite oxidation counteracts CO_2 drawdown from silicate weathering in the Langtang-Trisuli-Narayani River system, Nepal Himalaya. *Geochimica et Cosmochimica Acta*, *294*, 43-69.

Kim, S.H. (1987). A study on stratigraphy and paleontology of the Makgol limestone distributed in the South Part of the Baegunsan Syncline – Chiefly by Means of Conodont Study. MS dissertation, Yonsei University, Seoul, South Korea.

Kim, Y., & Lee, Y. I. (2006). Early evolution of the Duwibong Unit of the lower Paleozoic Joseon Supergroup, Korea: A new view. Geosciences Journal, 10(4), 391-402.

Kobayashi, T. (1966). The Cambro-Ordovician formations and faunas of South Korea. Part X.

Stratigraphy of the Chosen Group in Korea and South Manchuria and its relation to the Cambro-Ordovician formations of other areas. Section A. The Chosen Group of South Korea. *Journal of the Faculty of Science, University of Tokhyo*, *16*, 1-84.

Koch, J. T., & Frank, T. D. (2011). The Pennsylvanian–Permian transition in the low-latitude carbonate record and the onset of major Gondwanan glaciation. *Palaeogeography, Palaeoclimatology, Palaeoecology*, *308*(3-4), 362-372.

Korte, C., Jasper, T., Kozur, H. W., & Veizer, J. (2005). $\delta^{18}O$ and $\delta^{13}C$ of Permian brachiopods: a record of seawater evolution and continental glaciation. Palaeogeography, Palaeoclimatology, Palaeoecology, 224(4), 333-351.

Kozik, N. P., Young, S. A., Bowman, C. N., Saltzman, M. R., & Them II, T. R. (2019). Middle–Upper Ordovician (Darriwilian–Sandbian) paired carbon and sulfur isotope stratigraphy from the Appalachian Basin, USA: Implications for dynamic redox conditions spanning the peak of the Great Ordovician Biodiversification Event. Palaeogeography, Palaeoclimatology, Palaeoecology, 520, 188-202.

Kroopnick, P. M. (1985). The distribution of 13C of ΣCO_2 in the world oceans. *Deep Sea Research Part A. Oceanographic Research Papers*, *32*(1), 57-84.

Kump, L. R., & Arthur, M. A. (1999). Interpreting carbon-isotope excursions: carbonates and organic matter. *Chemical Geology*, *161*(1-3), 181-198.

Kurtz, A. C., Kump, L. R., Arthur, M. A., Zachos, J. C., & Paytan, A. (2003). Early Cenozoic decoupling of the global carbon and sulfur cycles. Paleoceanography, 18(4).

Kwon, Y. J., & Kwon, Y. K. (2020). Sequence stratigraphy in the Middle Ordovician carbonate successions (Yeongheung Formation), mid-east Korea: Paleogeographic implications for a land-detached ramp-type platform. Journal of Asian Earth Sciences, 193, 104263.

Kwon, Y. K. (2012). Sequence Stratigraphy of the Yeongwol Group (Cambrian-Ordovician),

Taebaeksan Basin, Korea: Paleogeographic Implications. Economic and Environmental Geology, 45(3), 317-333.

Kwon, Y. K., & Chough, S. K. (2005). Sequence stratigraphy of the cyclic successions in the Dumugol Formation (Lower Ordovician), mideast Korea. Geosciences Journal, 9(4), 305-324.

Kwon, Y. K., Chough, S. K., Choi, D. K., & Lee, D. J. (2006). Sequence stratigraphy of the Taebaek Group (Cambrian–Ordovician), mideast Korea. Sedimentary Geology, 192(1-2), 19-55.

Lang, X., Shen, B., Peng, Y., Huang, K., Lv, J., & Ma, H. (2016). Ocean oxidation during the deposition of basal Ediacaran Doushantuo cap carbonates in the Yangtze Platform, South China. *Precambrian Research*, *281*, 253-268.

Leavitt, W. D., Halevy, I., Bradley, A. S., & Johnston, D. T. (2013). Influence of sulfate reduction rates on the Phanerozoic sulfur isotope record. Proceedings of the National Academy of Sciences, 110(28), 11244-11249.

Lee, B. S., & Seo, K. S. (2004). Lower Paleozoic conodonts of Korea. Paleontological Society of Korea, Special Publication, 7, 189-215.

Lee, B. S., Cho, S. H., Choh, S. J., & Wang, X. (2022). Confirmation of the Floian-Darriwilian (Lower to Middle Ordovician) hiatus in the Taebaek Group, Korea: integration of conodont biostratigraphy and sedimentology. Geosciences Journal, 1-19.

Lee, D. C., & Choi, D. K. (1992). Reappraisal of the Middle Ordovician trilobites from the Jigunsan Formation, Korea. 지질학회지, 28(2), 167-183.

Lee, D. J., & Yoo, C. M. (1993). Middle Ordovician stromatoporoids from the Yeongheung Formation and its biostratigraphic implication. *Journal of the Paleontological Society of Korea*, *9*, 131-142.

Lee, H. Y. (1979). A Study on Biostratigraphy and Bioprovince of the Middle Ordovician Conodonts

from South Korea: With Special reference to the Conodonts from the Yeongheung Formation. 지질학 회지, 15(1), 37-60.

Lee, J. S. (1927). Fusulinidae of North China. Paleontologica Sinica. ser. B 4(1): 1-123.

Lee, K.W., & Lee, H.Y., (1990). Conodont biostratigraphy of the Upper Joseon Supergroup in Janseong-Dongjeom area, Gangwondo. J. Paleont. Soc. Koew 13, 356-375

Lee, S. (2013). An integrated multidisciplinary palaeontological study of selected permian arctic brachiopods (No. Ph. D). Deakin University.

Lee, S. J. (1990). Conodont biostratigraphy of the lower Paleozoic Yeongheung Formation in the Yeongwol area, Kangweondo, Korea. Unpublished MS thesis, YOnsei University, 107p.(in Korean).

Lee, Y. I. (1988). Storm sedimentation in the Middle Ordovician Duwibong Formation, southern Taebaeg City. 지질학회지, 24(3), 234-242.

Lee, Y. I., Hyeong, K., & Yoo, C. M. (2001). Cyclic sedimentation across a middle Ordovician carbonate ramp (Duwibong Formation), Korea. *Facies*, *44*, 61-73.

Lee, Y. N. (1986). Conodont biostratigraphy of the Jigunsan shale and Duwibong limestone in the Nokjeon-Sangdong area, Yeongwol-gun, Kangweondo, Korea. Journal of Paleontological Society of Korea, 2, 114-136.

Lehnert, O., Meinhold, G., Wu, R., Calner, M., & Joachimski, M. M. (2014). δ^{13}C chemostratigraphy in the upper Tremadocian through lower Katian (Ordovician) carbonate succession of the Siljan district, central Sweden. Estonian Journal of Earth Sciences, 63(4), 277-286.

Li, J., Hu, X., Garzanti, E., & BouDagher-Fadel, M. (2022). Spatial heterogeneity in carbonate-platform environments and carbon isotope values across the Paleocene–Eocene thermal maximum (Tethys

Himalaya, South Tibet). Global and Planetary Change, 103853.

Liu, M., Chen, D., Zhou, X., Yuan, W., Jiang, M., & Liu, L. (2019). Climatic and oceanic changes during the Middle-Late Ordovician transition in the Tarim Basin, NW China and implications for the Great Ordovician Biodiversification Event. Palaeogeography, Palaeoclimatology, Palaeoecology, 514, 522-535.

Lowenstein, T.K., Hardie, L.A., Timofeeff, M.N., Demicco, R.V., (2003). Secular variation in seawater chemistry and the origin of calcium chloride basinal brines. Geol-ogy31, 857–860

Ma, H., Dong, L., Shen, B., Qiu, X., Peng, Y., Xiang, K., & Sun, Y. (2021). Sulfur and oxygen isotopic compositions of carbonate associated sulfate (CAS) of Cambrian ribbon rocks: Implications for the constraints on using CAS to reconstruct seawater sulfate sulfur isotopic compositions. Chemical Geology, 580, 120369.

Mangerud, G., & Konieczny, R. M. (1993). Palynology of the Permian succession of Spitsbergen, Svalbard. Polar Research, 12(1), 65-93.

Marenco, P. J., Corsetti, F. A., Hammond, D. E., Kaufman, A. J., & Bottjer, D. J. (2008). Oxidation of pyrite during extraction of carbonate associated sulfate. Chemical Geology, 247(1-2), 124-132.

Montañez, I. P., & Poulsen, C. J. (2013). The Late Paleozoic ice age: an evolving paradigm. Annual Review of Earth and Planetary Sciences, 41, 629-656.

Montañez, I. P., McElwain, J. C., Poulsen, C. J., White, J. D., DiMichele, W. A., Wilson, J. P., & Hern, M. T. (2016). Climate, pCO_2 and terrestrial carbon cycle linkages during late Palaeozoic glacial–interglacial cycles. Nature Geoscience, 9(11), 824-828.

Moon, J. H., Joo, Y. J., Kang, J. O., & Sim, M.S. (2021). Measurement of sulfur isotope ratios in trace amounts of dissolved sulfate by MC-ICP-MS. Journal of the Geological Society of Korea. v. 57, no. 1, p. 99-108

Nakrem, H. A., Nilsson, I., & Mangerud, G., (1992), Permian biostratigraphy of Svalbard (Arctic Norway)-a review: International Geology Review

Nelsen, M. P., DiMichele, W. A., Peters, S. E., & Boyce, C. K. (2016). Delayed fungal evolution did not cause the Paleozoic peak in coal production. Proceedings of the National Academy of Sciences, 113(9), 2442-2447

Nestor, H., & Webby, B. D. (2013). Chapter 7 Biogeography of the Ordovician and Silurian Stromatoporoidea. Geological Society, London, Memoirs, 38(1), 67-79.

Nilsson, I. (1994). Upper Palaeozoic fusulinid assemblages, Wandel Sea Basin, North Greenland. Rapport Grønlands Geologiske Undersøgelse, 161, 45-71.

Nilsson, I., & Davydov, V. I. (1997). Fusulinid biostratigraphy in Upper Carboniferous (Gzhelian) and Lower Permian (Asselian-Sakmarian) successions of Spitsbergen. Arctic Norway. Permophiles, 30, 18-24.

Oh, J. R., Choh, S. J., & Lee, D. J. (2015). First report of Cystostroma (Stromatoporoidea; Ordovician) from Sino-Korean Craton. Geosciences Journal, 19, 25-31.

Oh, Y., Lee, S., Park, T. Y. S., & Lee, D. C. (2023). Middle Ordovician (middle Darriwilian) Dirafinesquina and Jigunsania gen. nov.(Rafinesquinidae; Strophomenoidea; Brachiopoda) from South Korea, with discussion of rafinesquinid evolution. Geosciences Journal, 1-18.

Oordt, A. J., Soreghan, G. S., Stemmerik, L., & Hinnov, L. A. (2020). A record of dust deposition in northern, mid-latitude Pangaea during peak icehouse conditions of the late Paleozoic ice age. Journal of Sedimentary Research, 90(4), 337-363.

Paik, I. S. (1987). Depositional environments of the Middle Ordovician Maggol Formation, southern part of the Baegunsan Syncline area. J. Geol. Korea, 23(4), 360-373.

Paris, G., Adkins, J. F., Sessions, A. L., Webb, S. M., & Fischer, W. W. (2014a). Neoarchean carbonate–

associated sulfate records positive Δ33S anomalies. *Science*, *346*(6210), 739-741.

Paris, G., Fehrenbacher, J. S., Sessions, A. L., Spero, H. J., & Adkins, J. F. (2014b). Experimental determination of carbonate-associated sulfate δ^{34}S in planktonic foraminifera shells. *Geochemistry, Geophysics, Geosystems*, *15*(4), 1452-1461.

Paris, G., Sessions, A. L., Subhas, A. V., & Adkins, J. F. (2013). MC-ICP-MS measurement of δ^{34}S andΔ ^{33}S in small amounts of dissolved sulfate. Chemical Geology, 345, 50-61.

Pasquier, V., Bryant, R. N., Fike, D. A., & Halevy, I. (2021). Strong local, not global, controls on marine pyrite sulfur isotopes. Science advances, 7(9), eabb7403.

Pasquier, V., Sansjofre, P., Rabineau, M., Revillon, S., Houghton, J., & Fike, D. A. (2017). Pyrite sulfur isotopes reveal glacial − interglacial environmental changes. Proceedings of the National Academy of Sciences, 114(23), 5941-5945

Paytan, A., Kastner, M., Campbell, D., & Thiemens, M. H. (2004). Seawater sulfur isotope fluctuations in the Cretaceous. science, 304(5677), 1663-1665.

Present, T. M., Adkins, J. F., & Fischer, W. W. (2020). Variability in sulfur isotope records of Phanerozoic seawater sulfate. Geophysical Research Letters, 47(18), e2020GL088766.

Present, T. M., Gutierrez, M., Paris, G., Kerans, C., Grotzinger, J. P., & Adkins, J. F. (2019). Diagenetic controls on the isotopic composition of carbonate-associated sulphate in the Permian Capitan Reef Complex, West Texas. *Sedimentology*, *66*(7), 2605-2626.

Present, T. M., Paris, G., Burke, A., Fischer, W. W., & Adkins, J. F. (2015). Large carbonate associated sulfate isotopic variability between brachiopods, micrite, and other sedimentary components in Late Ordovician strata. *Earth and Planetary Science Letters*, *432*, 187-198.

Qie, W., Liu, J., Chen, J., Wang, X., Mii, H. S., Zhang, X., & Luo, G. (2015). Local overprints on the global carbonate δ13C signal in Devonian–Carboniferous boundary successions of South

China. *Palaeogeography, Palaeoclimatology, Palaeoecology*, *418*, 290-303.

Rabus, R., Hansen, T. A., & Widdel, F. (2006). Dissimilatory sulfate-and sulfur-reducing prokaryotes. The prokaryotes, 2, 659-768.

Rasmussen, C. M., Ullmann, C. V., Jakobsen, K. G., Lindskog, A., Hansen, J., Hansen, T., & Nielsen, A. T. (2016). Onset of main Phanerozoic marine radiation sparked by emerging Mid Ordovician icehouse. Scientific Reports, 6(1), 1-9.

Rennie, V. C., & Turchyn, A. V. (2014). The preservation of $\delta^{34}S_{SO4}$ and $\delta^{18}O_{SO4}$ in carbonate-associated sulfate during marine diagenesis: A 25 Myr test case using marine sediments. Earth and Planetary Science Letters, 395, 13-23.

Rennie, V. C., Paris, G., Sessions, A. L., Abramovich, S., Turchyn, A. V., & Adkins, J. F. (2018). Cenozoic record of $\delta^{34}S$ in foraminiferal calcite implies an early Eocene shift to deep-ocean sulfide burial. Nature Geoscience, 11(10), 761-765.

Richardson, J. A., Keating, C., Lepland, A., Hints, O., Bradley, A. S., & Fike, D. A. (2019). Silurian records of carbon and sulfur cycling from Estonia: The importance of depositional environment on isotopic trends. Earth and Planetary Science Letters, 512, 71-82.

Richardson, J. A., Lepland, A., Hints, O., Prave, A. R., Gilhooly III, W. P., Bradley, A. S., & Fike, D. A. (2021). Effects of early marine diagenesis and site-specific depositional controls on carbonate-associated sulfate: Insights from paired S and O isotopic analyses. Chemical Geology, 584, 120525.

Roscher, M., & Schneider, J. W. (2006). Permo-Carboniferous climate: Early Pennsylvanian to Late Permian climate development of central Europe in a regional and global context. Geological Society, London, Special Publications, 265(1), 95-136.

Rose, C. V., Fischer, W. W., Finnegan, S., & Fike, D. A. (2019). Records of carbon and sulfur cycling during the Silurian Ireviken Event in Gotland, Sweden. Geochimica et Cosmochimica Acta, 246, 299-

316.

Ross, C. A., & Ross, J. R. (1987). Late Paleozoic Sea levels and depositional sequences. *Cushman Foundation for Foraminiferal Research*, 137.

Rozovskaya, S. E., (1948). Classification and systematic features of the genus Triticites. Reports of the Academy of Sciences USSR. 59(9): 1635-1638.

Rygel, M. C., Fielding, C. R., Frank, T. D., & Birgenheier, L. P. (2008). The magnitude of Late Paleozoic glacioeustatic fluctuations: a synthesis. *Journal of Sedimentary Research*, *78*(8), 500-511.

Saalmann, K., & Thiedig, F. (2002). Thrust tectonics on Brøggerhalvøya and their relationship to the Tertiary West Spitsbergen Fold-and-Thrust Belt. *Geological Magazine*, *139*(1), 47-72.

Saltzman, M. R., Groessens, E., & Zhuravlev, A. V. (2004). Carbon cycle models based on extreme changes in δ13C: an example from the lower Mississippian. *Palaeogeography, Palaeoclimatology, Palaeoecology*, *213*(3-4), 359-377.

Samuelsberg, T. J., & Pickard, N. A. (1999). Upper Carboniferous to lower Permian transgressive–regressive sequences of central Spitsbergen, Arctic Norway. *Geological Journal*, *34*(4), 393-411.

Scheffler, K., Buehmann, D., & Schwark, L. (2006). Analysis of late Palaeozoic glacial to postglacial sedimentary successions in South Africa by geochemical proxies–Response to climate evolution and sedimentary environment. Palaeogeography, Palaeoclimatology, Palaeoecology, 240(1-2), 184-203.

Scheffler, K., Hoernes, S., & Schwark, L. (2003). Global changes during Carboniferous–Permian glaciation of Gondwana: Linking polar and equatorial climate evolution by geochemical proxies. Geology, 31(7), 605-608.

Scheibner, C., Blomeier, D., Forke, H., & Gesierich, K. (2015). From terrestrial to shallow-marine depositional environments: reconstruction of the depositional environments during the Late Carboniferous transgression of the Lomfjorden Trough in NE Spitsbergen (Malte Brunfjellet

Formation). Norwegian Journal of Geology/Norsk Geologisk Forening, 95(2).

Scholle, P.A., Arthur, M.A., Ekdale, A.A., (1983). Pelagic environment. In: Scholle, P.A., Bebout, D.G., Moore, C.H. (Eds.), Carbonate Depositional Environments. AAPG, Memoir 33, 619–691.

Schrag, D. P., Higgins, J. A., Macdonald, F. A., & Johnston, D. T. (2013). Authigenic carbonate and the history of the global carbon cycle. science, 339(6119), 540-543.

Schroller-Lomnitz, U., Hensen, C., Dale, A. W., Scholz, F., Clemens, D., Sommer, S., ... & Wallmann, K. (2019). Dissolved benthic phosphate, iron and carbon fluxes in the Mauritanian upwelling system and implications for ongoing deoxygenation. *Deep Sea Research Part I: Oceanographic Research Papers*, *143*, 70-84.

Scotese, C. R. & Golonka, J., (1997). Paleogeographic Atlas. Paleomap Project 1, University of Texas at Arlington, pp. 31.

Servais, T., & Harper, D. A. (2018). The great Ordovician biodiversification event (GOBE): definition, concept and duration. Lethaia, 51(2), 151-164.

Shields, G. A., Mills, B. J., Zhu, M., Raub, T. D., Daines, S. J., & Lenton, T. M. (2019). Unique Neoproterozoic carbon isotope excursions sustained by coupled evaporite dissolution and pyrite burial. *Nature Geoscience*, *12*(10), 823-827.

Sim, M. S., Bosak, T., & Ono, S. (2011a). Large sulfur isotope fractionation does not require disproportionation. *Science*, *333*(6038), 74-77.

Sim, M. S., Ono, S., & Bosak, T. (2012). Effects of iron and nitrogen limitation on sulfur isotope fractionation during microbial sulfate reduction. Applied and environmental microbiology, 78(23), 8368-8376.

Sim, M. S., Ono, S., Donovan, K., Templer, S. P., & Bosak, T. (2011b). Effect of electron donors on the fractionation of sulfur isotopes by a marine Desulfovibrio sp. Geochimica et Cosmochimica

Acta, 75(15), 4244-4259.

Sim, M. S., Woo, D. K., Kim, B., Jeong, H., Joo, Y. J., Hong, Y. W., & Choi, J. Y. (2023). What Controls the Sulfur Isotope Fractionation during Dissimilatory Sulfate Reduction?. *ACS Environmental Au*, *3*(2), 76-86.

Song, H., Tong, J., Algeo, T. J., Horacek, M., Qiu, H., Song, H., ... & Chen, Z. Q. (2013). Large vertical δ13CDIC gradients in Early Triassic seas of the South China craton: Implications for oceanographic changes related to Siberian Traps volcanism. *Global and Planetary Change*, *105*, 7-20.

Sorento, T., Olaussen, S., & Stemmerik, L. (2020). Controls on deposition of shallow marine carbonates and evaporites–lower Permian Gipshuken Formation, central Spitsbergen, Arctic Norway. *Sedimentology*, *67*(1), 207-238.

Sosipatrova, G. P., (1967). Upper Paleozoic foraminifera assemblages of Spitsbergen. Doklady Akademii Nauk. Rossiyskaya Akademiya Nauk, 176(1), 182-185.

Staudt, W. J., Reeder, R. J., & Schoonen, M. A. (1994). Surface structural controls on compositional zoning of $SO2-4$ and $SeO2-4$ in synthetic calcite single crystals. Geochimica et Cosmochimica Acta, 58(9), 2087-2098.

Strauss, H. (1999). Geological evolution from isotope proxy signals—sulfur. Chemical Geology, 161(1-3), 89-101.

Stein, R. (1986). Organic carbon and sedimentation rate—further evidence for anoxic deep-water conditions in the Cenomanian/Turonian Atlantic Ocean. *Marine Geology*, *72*(3-4), 199-209.

Stein, R. (1990). Organic carbon content/sedimentation rate relationship and its paleoenvironmental significance for marine sediments. *Geo-Marine Letters*, *10*, 37-44.

Stigall, A. L., Edwards, C. T., Freeman, R. L., & Rasmussen, C. M. (2019). Coordinated biotic and abiotic change during the Great Ordovician Biodiversification Event: Darriwilian assembly of early

Paleozoic building blocks. Palaeogeography, Palaeoclimatology, Palaeoecology, 530, 249-270.

Sur, S., Owens, J. D., Soreghan, G. S., Lyons, T. W., Raiswell, R., Heavens, N. G., & Mahowald, N. M. (2015). Extreme eolian delivery of reactive iron to late Paleozoic icehouse seas. Geology, 43(12), 1099-1102.

Thompson, C. K., & Kah, L. C. (2012). Sulfur isotope evidence for widespread euxinia and a fluctuating oxycline in Early to Middle Ordovician greenhouse oceans. Palaeogeography, Palaeoclimatology, Palaeoecology, 313, 189-214.

Thompson, M. L., (1935). The Fusulinid genus Staffella in America. Journal of Palaeontology. 9(2): 111-120.

Thompson, M. L., (1947). Stratigraphy and fusulinids of pre-Desmoinesian Pennsylvanian rocks, Llano uplift, Texas. Journal of Paleontology, 147-164.

Torres, M. A., Moosdorf, N., Hartmann, J., Adkins, J. F., & West, A. J. (2017). Glacial weathering, sulfide oxidation, and global carbon cycle feedbacks. Proceedings of the National Academy of Sciences, 114(33), 8716-8721

Torres, M. A., West, A. J., & Li, G. (2014). Sulphide oxidation and carbonate dissolution as a source of CO 2 over geological timescales. Nature, 507(7492), 346-349.

Turchyn, A. V., & DePaolo, D. J. (2019). Seawater chemistry through Phanerozoic time. *Annual Review of Earth and Planetary Sciences*, *47*, 197-224.

Waldron, J. W., Rygel, M. C., Gibling, M. R., & Calder, J. H. (2013). Evaporite tectonics and the late Paleozoic stratigraphic development of the Cumberland basin, Appalachians of Atlantic Canada. *GSA Bulletin*, *125*(5-6), 945-960.

Wallmann, K. (2001). The geological water cycle and the evolution of marine δ18O values. Geochimica et Cosmochimica Acta, 65(15), 2469-2485.

Wang, Z., Zhen, Y. Y., Bergstrom, S. M., Zhang, Y., & Wu, R. (2018). Ordovician conodont biozonation and biostratigraphy of North China. Australasian Palaeontological Memoirs, (51), 65-79.

Weyer, S., & Schwieters, J. B. (2003). High precision Fe isotope measurements with high mass resolution MC-ICPMS. International Journal of Mass Spectrometry, 226(3), 355-368.

Wilson, J. P., Montañez, I. P., White, J. D., DiMichele, W. A., McElwain, J. C., Poulsen, C. J., & Hren, M. T. (2017). Dynamic Carboniferous tropical forests: new views of plant function and potential for physiological forcing of climate. New Phytologist, 215(4), 1333-1353.

Wing, B. A., & Halevy, I. (2014). Intracellular metabolite levels shape sulfur isotope fractionation during microbial sulfate respiration. *Proceedings of the National Academy of Sciences*, *111*(51), 18116-18125.

Woo, J., & Chough, S. K. (2007). Depositional processes and sequence stratigraphy of the Jigunsan Formation (Middle Ordovician), Taebaeksan Basin, mideast Korea: implications for basin geometry and sequence development. Geosciences Journal, 11, 331-355.

Woo, J., Lee, H. S., & Chough, S. K. (2023). Deposition of sandstone (early Cambrian) above the Great Unconformity in the Sino-Korean Block, Gondwana: Control of antecedent topography. Gondwana Research, 116, 212-228.

Wotte, T., Shields-Zhou, G. A., & Strauss, H. (2012). Carbonate-associated sulfate: Experimental comparisons of common extraction methods and recommendations toward a standard analytical protocol. Chemical Geology, 326, 132-144

Wu, N. (2013). *Sulfur isotopic evolution of Phanerozoic and Ediacaran seawater sulfate* (Doctoral dissertation).

Wu, N., Farquhar, J., & Strauss, H. (2014). δ^{34}S and Δ^{33}S records of Paleozoic seawater sulfate based on the analysis of carbonate associated sulfate. Earth and Planetary Science Letters, 399, 44-51.

Wu, R., Calner, M., & Lehnert, O. (2017). Integrated conodont biostratigraphy and carbon isotope chemostratigraphy in the Lower–Middle Ordovician of southern Sweden reveals a complete record of the MDICE. Geological Magazine, 154(2), 334-353.

Yao, W., Paytan, A., & Wortmann, U. G. (2018). Large-scale ocean deoxygenation during the Paleocene-Eocene Thermal Maximum. Science, 361(6404), 804-806.

Yoo, C. M., & Lee, Y. I. (1997). Depositional cyclicity of the Middle Ordovician Yeongheung Formation, Korea. Carbonates and Evaporites, 12(2), 192-203.

Yoo, C. M., Lee, Y. I., & Paik, I. S. (1994). Evidence for hypersaline conditions in the middle Ordovician Yeongheung Formation, Korea. J. Geol. Korea, 30(4), 355-368.

Young, S. A., Gill, B. C., Edwards, C. T., Saltzman, M. R., & Leslie, S. A. (2016). Middle–Late Ordovician (Darriwilian–Sandbian) decoupling of global sulfur and carbon cycles: Isotopic evidence from eastern and southern Laurentia. Palaeogeography, Palaeoclimatology, Palaeoecology, 458, 118-132.

Yu, S., Fang, X., Zhang, Y., Zhen, Y. Y., Li, W., Li, Y., & Munnecke, A. (2021). First record of the Middle Darriwilian $\delta^{13}C$ excursion (MDICE) in southern Xizang (Tibet), China, and its implications. Carbonates and Evaporites, 36(2), 1-11.

Zerkle, A. L., Farquhar, J., Johnston, D. T., Cox, R. P., & Canfield, D. E. (2009). Fractionation of multiple sulfur isotopes during phototrophic oxidation of sulfide and elemental sulfur by a green sulfur bacterium. Geochimica et Cosmochimica Acta, 73(2), 291-306.

Zhang, Y., & Munnecke, A. (2016). Ordovician stable carbon isotope stratigraphy in the Tarim Basin, NW China. Palaeogeography, Palaeoclimatology, Palaeoecology, 458, 154-175.

Zhen, Y. Y., Zhang, Y., Wang, Z., & Percival, I. G. (2016). Huaiyuan Epeirogeny—shaping Ordovician stratigraphy and sedimentation on the North China Platform. PPP.

국문 초록

고생대의 탄소 및 황 순환에 대한 전 지구적 및 지역적인 해석

권효상

서울대학교 지구환경과학부

퇴적암에서의 얻을 수 있는 안정 황 동위원소 기록은 과거 지구의 황 순환의 중요한 기록이다. 이 논문의 목표는 전기 및 후기 고생대의 지층에서 산화 및 환원된 형태의 탄소와 황 동위원소 기록을 통해 고생대의 생지화학순환을 지역적 및 전 지구적 관점에서 해석하는 것이다. 제 1 장은 황 순환에 대한 기초 지식을 정리하여 논문의 이해를 도울 수 있도록 하였다. 1 장에서 주로 정리된 내용은 황 환원 미생물의 생리, 황 동위원소 값의 퇴적학적 요소에 의한 변화, 그리고 전 지구적 황 순환의 변화 요인에 대한 것이다.

제 2 장에서는 한국의 태백과 영월 지역의 상부 조선누층군에서 탄산염 탄소, CAS, 그리고 황화철 황 동위원소 분석을 통해서 오르도비스기의 지역적 및 세계적인 생지화학 순환을 이해하고자 하였다. 태백과 영월 지역의 탄소 동위원소 및 황화철의 황 동위원소는 두 지역이 하나의 퇴적분지 내에서 서로 근접한 위치에도 불구하고 퇴적 환경 차이로 인해 상이한 경향을 보인다. 태백 지역에서 탄소 동위원소 값은 직운산층 하부에서 −4 퍼밀의 음의 이상값이 나타나는데 이러한 패턴은 같은 시기 다른 어떤 지역에서도 나타나지 않는다. 따라서 직운산층의 탄소동위원소 이상값은 닫혀 있는 분지에서의 지역적인 환경 변화를 나타내며 퇴적 속도의 감소로 인해 무산소 호흡이 증가하고 그로 인해 생긴 가벼운 DIC 들이 유입되면서 나타나는 것으로 해석할 수 있다.

태백에서의 황 동위원소 값의 변화는 두위봉층과 직운산층에서 나타나는 퇴적속도와 수심에 따라 황 환원 미생물에 도달하는 유기물 공급의 변화에 의해 나타나는 것으로 해석된다. 다만 직운산층 하부에는 수심이 깊어짐에도 황화철의 황 동위원소 값이 증가하는 모습이 나타나는데 이것은 직운산층 하부가 쌓였던 환경이 무산소 환경으로 황 환원 세균에 의한 유기물의 분해가 활발히 일어나서 나타나는 현상일 것으로 보인다.

영월 지역의 황 동위원소 조성이 특별한 경향성 없이 태백보다 더 무거운 값을 보이는 이유는 상대적으로 영월 지역의 수심이 얕고 수심의 변화가 적기 때문에 나타나는 것으로 해석한다. 영월지역이 안정적인 퇴적환경이 유지되는 것에 비해 태백형에서 조금 더 많은 변화가 나타나는 것은 태백 지역이 육지에 더 가까운 환경이었기 때문일 것으로 추측한다.

제 3 장은 고생대 후기의 생지화학 순환과 지구조 운동 및 기후변화의 연관성에 대해서 다룬다. 고생대 후기는 여러 번의 대륙 충돌과 빙하기가 발생한 시기이다. 이러한 급격한 환경변화에도 불구하고 황 동위원소 데이터의 부족으로 인해 고생대 후기의 생지화학 순환에 대한 이해는 제한적이었다. 따라서 제 2 장에서는 스발바르 지역의 석탄기–페름기 탄산염 지층에서의 CAS 및 황화철의 황 동위원소 분석을 실시하여 생지화학 순환의 이해를 높이고자 하였다. 석탄기 후기의 CAS 동위원소 값은 이전에 보고된 값과 비슷한 경향을 보였지만 석탄기 말기에는 닫힌계의 형성으로 인한 +20‰의 양의 이상값이 발견되었다. 초기 페름기의 CAS 동위원소 기록은 짧은 기간 발생하는 변동 사이에서 지속적으로 상승하는 추세가 발견되었다. 짧은 기간의 변동은 아틴스키안절에 발생한 해침으로 인해 발생한 것으로 해석한다. 하지만 긴 기간의 상승 추세는 빙하기에 유기물 매장이 주로 일어나는 지역이 육상에서 해양으로 옮겨가면서 황화철의 매장량이 늘고 대륙 충돌로 인해 증발암의 풍화가 증가하면서 생겨난 것으로 해석하였다. 석탄기 중기에 발생한 황 동위원소의 양의 이상값도 마찬가지로 대륙 충돌 및 빙하기가 발생하는 시기에 기록되므로 비슷한 관점에서 황화철 매장량 증가와 증발암 풍화의 증가로 해석이 가능하며, 이것은 대륙충돌과 기후변화가 황 순환과 밀접한 관련이 있음을 보여준다.

제 4 장은 MC-ICP-MS 를 가지고 분석하기 위한 전암에서의 CAS 추출 방법을 소개하고 그 방법의 정확성과 반복성을 검증하기 위한 여러 실험 결과에 대해서 보여줄 것이다. 실험 결과는 정확성과 반복성이 1 퍼밀 이내로 전통적인 방법과 비슷하게 나타나 낮은 농도의 CAS 를 가진 샘플에 대해서도 mesoscale 방법을 이용하면 전통적인 방법과 비슷한 수준의 반복성으로 측정할 수 있을 가능성을 보여주었다. 그러나 황화철을 추가로 넣은 실험에서는 황 동위원소 데이터가 낮아지는 것이 보여 산화가 방지되지 않았다는 것이 확인되었다. 황화철 함량이 높은 조선누층군 샘플에서의 mesoscale 실험 결과도 낮은 동위원소 값을 보여주어 황화철의 산화가 방지되지 않았음을 보여주었다. 황화철 산화를 배제하기 위해 microscale 로 황화철이 없는

부분을 슬랩에서 추출하여 실험을 한 결과는 authigenic carbonate 에 가벼운 CAS 동위원소 값이 나타날 수 있다는 것을 보여주었다. 하지만 전암 분석의 경우에는 여러 조직들이 섞여 속성작용의 영향이 희석되므로 황화철 함량만 먼저 고려된다면 mesoscale 로 분석을 했을 때 CAS 가 낮은 탄산염암에서도 해수의 값을 얻을 수 있을 것으로 보인다.